UNIVERSIDADE DE SÃO PAULO
INSTITUTO DE ASTRONOMIA, GEOFÍSICA E CIÊNCIAS ATMOSFÉRICAS
DEPARTAMENTO DE GEOFÍSICA

KARINE ZUCCOLAN CARVAS

A record of the transition between Gondwana and South Atlantic crust in the tholeiitic intrusive magmatism of Cabo Frio Tectonic Domain, Southeast Brazil

SÃO PAULO
2022

A record of the transition between Gondwana and South Atlantic crust in the tholeiitic intrusive magmatism of Cabo Frio Tectonic Domain, Southeast Brazil

Original version

Thesis to be presented to the Geophysics Department of Instituto de Astronomia, Geofísica e Ciências Atmosféricas of the University of São Paulo as a partial requirement for the PhD title.

Concentration Area: Geophysics, Geochronology and Geochemistry

Advisors: Professor Leila Soares Marques and Professor Paulo Vasconcelos

São Paulo
2022
Karine Zuccolan Carvas

Aos meus avós – o que deles conheci, o que deles imagino.

ACKNOWLEDGEMENTS / AGRADECIMENTOS

Inicialmente, eu agradeço à Fundação de Amparo à Pesquisa do Estado de São Paulo (FAPESP; processos 2012/06082-6, 2014/22948-9, 2017/18232-6, 2018/23650-4), ao Conselho Nacional de Desenvolvimento Científico e Tecnológico (CNPq; processo 141058/2018-8), e à Coordenação de Aperfeiçoamento de Pessoal de Nível Superior (CAPES; código de financiamento 001, processo 1425945) pelo financiamento das análises, cursos, auxílios e bolsas referentes a esta pesquisa. I also thank the Argon Geochronology Laboratory of The University of Queensland (UQ-AGES) for all financial support during my research period in Australia.

Agradeço profundamente aos meus orientadores pela imensa dedicação e generosidade. À Professora Doutora Leila Marques, pela incansável busca. Ao Professor Doutor Paulo Vasconcelos, pela incansável pergunta.

Agradeço aos colaboradores com os quais tive a sorte de contar ao longo deste trajeto. À Professora Doutora Marly Babinski, agradeço o incentivo criterioso desde os meus tempos de graduação. À Doutora Isabela Carmo, agradeço a frequente troca de boas ideias, a confiança, belas fotografias de campo e amostras adicionais. I am also thankful to Professor Teresa Ubide for reawakening my curiosity whenever we worked together, and for all valuable discussions.

Agradeço a todo o corpo docente e técnico-administrativo do Instituto de Astronomia, Geofísica e Ciências Atmosféricas da USP (IAG-USP) pela ajuda e prestatividade em diversos momentos. Sou especialmente grata aos Professores Doutores Marcia Ernesto, Naomi Ussami, Marcelo Bianchi, Carlos Mendonça e Ricardo Trindade pela orientação e suporte constantes.

Durante o desenvolvimento deste trabalho no Brasil, fui auxiliada por inúmeras pessoas de diferentes laboratórios da Universidade de São Paulo (USP) e da Universidade Estadual Paulista (UNESP). Agradeço ao Mestre (em breve Doutor) Caio Vicentini (IAG-USP), e ao Professor Doutor Fábio Machado (UFPR) pela ajuda em meu primeiro campo de amostragem, o qual serviria de base para os seguintes. Agradeço à coordenadora técnica do Laboratório de Preparação de amostras e da Litoteca do IAG-USP, Sônia Alonso, pela prestatividade, pela sabedoria generosa e pelos bolos. Sou grata a toda a equipe do Centro de Pesquisas Geocronológicas do Instituto de Geociências da USP (CPGeo – IGc – USP), sobretudo à especialista técnica em química isotópica e espectrometria de massa Liliane Petronilho.

Agradeço também às equipes dos Laboratórios de Fluorescência de Raios X e de Microscopia Eletrônica de Varredura do Departamento de Geologia da UNESP.

I acknowledge all the scientific and technical assistance I received from the UQ-AGES, the Centre for Microscopy and Microanalysis (CMM-UQ), the Radiogenic Isotope Facility (RIF-UQ) and the Sample Preparation Laboratory staff while in Australia, especially from Dr. Ai Nguyen, Dr. Gang Xia, Dr. Faye Liu, Ms. Yin Yu, Dr. Kim Sewell, and Ron Rasch.

I am especially thankful to Dr. Allan Gomes, Dr. Tracey Crossingham, Dr Al-Tamini Tapu, Ms. Alice Mcdonald and Dr. Zhe Ren for all the help, friendship, support and laughs inside and outside the School of Earth and Environmental Sciences. They were responsible for some of my best memories in Australia.

Agradeço também a amizade, os ombros, os ouvidos e os sorrisos que ganhei de tantos durante meu período de doutorado. Aline Mazzoni, Lais Vazami, Dani Gaeta, Mari Rossafa, Wil Poletti, Gra Luz, Karine Gottardo, Janine Carmo, Vitor Ido, Flávia Bonora, Denize Delomero, Vanessa Salomão, Ju Vilhena, Cláudio Andrade, Guilherme Oliveira, Daniel Patias, Fernanda Chupel, Fred Almeida, Melissa Makibara, Marco Scarpa, Lucas Diogo, Carlos Cardoso, Renan Noda, Daniel Blanc, Jessica Volejnik, Ivan Lavander, Fabi Nascimento, Dani Cury, Laura Cavalcanti, Maju Francischetto, Dr. Miguel Siqueira, Bianca Brandão, Filipe Temporim, Dani Brandt, Plinio Jaqueto, Andreise Saraiva, Aynoan Lopes, Sthefano Carvalho, Sheila de Carvalho, e tantos outros (aqui totalmente desordenados, como deve ser).

Sou grata pelo apoio, incentivo e afeto contínuos de toda minha família, especialmente de minhas tias Sônia e Denise, de minha mãe, Rosely, e de meu irmão, Caio. E do meu pai, Américo, sempre contínuo.

Sou grata pela presença do Fábio - durante todo este percurso aqui narrado, minha casa.

[...]
E se há nisto um segredo e uma verdade
Os deuses ou destinos que a demonstrem
Do outro lado da realidade,
Ou nunca a mostrem, se nada há que mostrem
O caminho é de âmbito maior
Que a aparência visível do que está fora,
Excede de todos nós o exterior
Não pára como as cousas, nem tem hora.

Ciência? Consciência? Pó que a ‘strada deixa
E é a própria ‘strada, sem ‘strada ser.
É absurda a oração, é absurda a queixa.
Resignar(-se) é tão falso como ter.
Coexistir? Com quem, se estamos sós?
Quem sabe? Sabe o que é ou quem são?
Quantos cabemos dentro de nós?
Ir é ser. Não parar é ter razão.
(Pessoa, In: Lopes, 1990)

They say the sea is cold, but the sea contains
the hottest blood of all, and the wildest, the most urgent.

All the whales in the wider deeps, hot are they, as they urge
on and on, and dive beneath the icebergs.
The right whales, the sperm-whales, the hammer-heads, the killers
there they blow, there they blow, hot wild white breath out of
the sea!

And they rock, and they rock, through the sensual ageless ages
on the depths of the seven seas,
and through the salt they reel with drunk delight
and in the tropics tremble they with love
and roll with massive, strong desire, like gods.
[...]
(Lawrence, 1977)

ABSTRACT

The transition from large igneous provinces (LIPs) into new ocean crust during early stages of rift evolution is largely unknown, and it is poorly represented or resolved in the geological record. Combining petrogenetic studies, magma dynamics investigations and novel geochronological approaches, this PhD thesis shows that early MORB- and Paraná-Etendeka-type intrusions associated with Gondwana breakup, in the Cabo Frio Tectonic Domain (Southeast Brazil), represent evidence of the initial oceanization of the South-America-Africa margins. A novel approach to ^{40}Ar/^{39}Ar geochronology of MORB-type dykes from the Cabo Frio Tectonic Domain was instrumental in differentiating between magmatism and post-magmatic alteration. Encapsulation procedures permitted focusing on minor and high retentivity magmatic amphibole and biotite aggregates. Incremental-heating analysis of both clear and cloudy feldspar crystals from the same sample revealed the ages of K- and Na-alteration. High-resolution elemental mapping of altered plagioclase crystals was combined with whole-rock elemental and isotopic analyses to determine elemental mobility and isotopic effects caused by hydrothermal fluid migration during tectonic evolution of the rifted margin. The intrusive age of a MORB-type dyke was determined to be 132.83 ± 0.30 Ma, i.e., late stages of Paraná-Etendeka magmatism. Altered plagioclase crystals show that K-, Na-, Rb-, Ba-, Sr-, Si-, Li-, Fe-, Pb- and light-REE-rich hydrothermal fluids percolated along the rifted margin between ~106-105 Ma and 60-30 Ma. Hydrothermalism was probably triggered by interactions between alkaline magmatism and basinal fluids in offshore basins along the southeastern Brazilian margin. Whole-rock geochemistry, Sr, Nd and Pb isotope signatures, mineral chemistry, thermobarometry, mass balance and thermodynamic models, and high-resolution elemental mapping of clinopyroxene crystals were used to model magma sources, magmatic evolution, and emplacement for MORB- and Paraná-Etendeka-type dykes. The LIP dykes are similar to low-Ti Ribeira magmas from the Paraná-Etendeka, deriving mostly from a metasomatized lithospheric peridotitic source that comprised a 1-3% ancient SCLM contribution applied to a 100-96% DMM – 0-4% pyroxenite mixture. MORB-type dykes share many similarities with South Atlantic MORB and E-MORB rocks, and were generated from an asthenospheric, peridotitic source consisting of a 100-98% DMM – 0-2% pyroxenite mixture with 0.2-0.4% ancient SCLM contribution. Both magmatic suites evolved mainly by plagioclase and clinopyroxene fractional crystallization under polybaric conditions. The multiple recharge events that fed MORB-type intrusive magmatism suggest a localized passive-margin system as early as ~2 Ma after peak LIP activity. Similar occurrences of subduction-influenced lithospheric and asthenospheric magma suites occur in rifts globally and indicate that crustal subductions related to continental amalgamation eventually contribute to the posterior destabilization of the continental structures.

Keywords: South Atlantic opening; Continental breakup; Hydrothermalism during rifting; Paraná-Etendeka intrusive magmatism; ^{40}Ar/^{39}Ar geochronology of mafic dykes; Oceanization of the continental crust; Dyke emplacement.

RESUMO

A transição entre o magmatismo de grandes províncias magmáticas (*large igneous provinces*, LIPs) e a geração de nova crosta oceânica durante estágios iniciais da evolução de riftes ainda é pouco conhecida e identificada enquanto registro geológico. Por meio do estudo da petrogênese, da dinâmica magmática e de novas abordagens geocronológicas, esta tese de doutoramento mostra que intrusões do tipo MORB e Paraná-Etendeka associadas à ruptura do paleocontinente Gondwana, no Domínio Tectônico de Cabo Frio (sudeste do Brasil) apresentam evidências da oceanização inicial das margens da América do Sul e África. O desenvolvimento de um protocolo para a geocronologia $^{40}Ar/^{39}Ar$ dos diques do tipo MORB do Terreno Tectônico de Cabo Frio proporcionou a diferenciação de registros magmáticos e de alterações pós-magmáticas. A encapsulação de alíquotas de amostras permitiu a análise de agregados de anfibólio e biotita de alta retentividade. As análises de cristais de plagioclásio leitosos e translúcidos revelaram idades aproximadas de alterações ricas em K e em Na. O mapeamento elemental de alta resolução de cristais de plagioclásio, associado às análises composicionais e isotópicas de rocha-total, foi capaz de determinar a mobilidade elemental causada pela migração de fluidos hidrotermais durante a evolução tectônica da margem. A idade de intrusão de um dique do tipo MORB foi determinada como 132.83 ± 0.30 Ma, correspondendo às fases finais do magmatismo Paraná-Etendeka. Cristais de plagioclásio alterados mostram que fluidos hidrotermais ricos em K, Na, Rb, Ba, Sr, Si, Li, Fe, Pb e Terras Raras leves percolaram a margem do rifte entre ~106-105 Ma e entre 60-30 Ma. O hidrotermalismo foi provavelmente provocado por interações entre magmas alcalinos e fluidos bacinais nas bacias *offshore* ao longo da margem sudeste do Brasil. Os dados de geoquímica de rocha-total, razões isotópicas de Sr, Nd e Pb, química mineral, termobarometria, modelos de balanço de massa e termodinâmicos, e mapeamento elemental de cristais de clinopiroxênio foram utilizados na modelagem de fontes mantélicas, evolução magmática e colocação dos diques do tipo MORB e Paraná-Etendeka. As intrusões do tipo LIP se assemelham aos basaltos de baixo-Ti Ribeira, e derivaram de uma fonte litosférica peridotítica metassomatizada correspondente a uma contribuição de 1-3% de manto litosférico subcontinental antigo (SCLM) a uma mistura de 100-96% de manto empobrecido (DMM) e 0-4% de piroxenito. Os diques do tipo MORB assemelham-se aos basaltos oceânicos do assoalho do Atlântico Sul e foram gerados por uma fonte astenosférica peridotítica consistindo em uma mistura de 100-98%

DMM e 0-2% piroxenito enriquecida por uma pequena contribuição de 0.2-0.4% de SCLM. Ambas as suítes magmáticas evoluíram via cristalização fracionada de plagioclásio e clinopiroxênio em condições de pressões variáveis. Os múltiplos eventos de recarga responsáveis pelo magmatismo do tipo MORB sugerem o estabelecimento restrito de um sistema de caráter passivo depois de apenas ~2Ma do pico da atividade vulcânica Paraná-Etendeka. Combinações similares de magmatismo astenosférico e litosférico com influência de subducções anteriores nas fontes mantélicas podem ser encontradas em riftes globalmente, indicando que sucessivos processos de subducção associados à amalgamação continental contribuem para a posterior desestabilização das estruturas da crosta.

Palavras-chave: Abertura do Atlântico Sul; Ruptura continental; Hidrotermalismo durante rifteamento; Magmatismo intrusivo Paraná-Etendeka, Geocronologia ^{40}Ar/^{39}Ar de diques máficos, Oceanização da crosta continental; Colocação de diques.

INDEX

LIST OF FIGURES

LIST OF TABLES

CHAPTER 1 - INTRODUCTION

Continental rifting is a fundamental step in the evolution of divergent plate margins (e.g., Peron-Pivindic et al., 2019; and references therein). Despite extensive studies and numerous models of the evolution of divergent tectonic margins (e.g., McKenzie, 1978; Wernicke, 1985), significant questions remain on the rheological regimes that dominate in magma-rich versus magma-poor rifts. In addition, the influence of ancient orogens, faults, and mantle-crust interactions in the geodynamic configuration and geomechanical processes leading to continental breakup remains understudied (Peron-Pivindic et al., 2019; Sapin et al., 2021).

Magmatism, the main topic of this thesis, plays an important role in passive margin evolution. The emplacement of sills and dyke swarms promotes fault reactivation and crustal accretion during extension (e.g., Thybo e Nielsen, 2009; Rivalta et al., 2015), and it is invariably associated with rift systems, even in magma-poor environments (e.g., Franke, 2013). Such intrusive complexes frequently display a broad range of chemical compositions, likely reflecting multiple magma sources, mantle heterogeneities, and/or variable levels of partial melting, fractional crystallization, or crustal assimilation during magma ascent (Wilson, 1989; Robin Gill, 2010). Investigating lithogeochemical changes through time may potentially help to unravel important geodynamic forces controlling rift evolution.

In cases where large igneous provinces (LIP) preceded continental rifting, for example, the transition from the LIP to typical mid-ocean ridge basaltic magmatism (MORB) starts by the progressive oceanization of the crust, which records the onset of a passive regime. Interestingly, age gaps of tens of millions of years exist between LIP magmatic rocks – extrusive and intrusive – and the oldest ocean floor at a given locality. In some places, however, local onshore intrusive MORB-like rocks appear to be contemporaneous with the main peak of LIP volcanism (e.g., Jagoutz et al., 2007; Jourdan et al., 2007), but their geodynamic role is still poorly constrained.

Opening of the South Atlantic Ocean, preceded by the Paraná-Etendeka LIP, is a good example where this complex relationship between magmatism and oceanization remains to be addressed. During LIP magmatism, volcanic activity lasted for 1.6-3.0 Ma, peaking at 134.5±0.1 Ma (Gomes e Vasconcelos, 2021; and references therein), and it was roughly contemporaneous with the initial stages – 132-126 Ma – of meridional Gondwana breakup (Torsvik et al., 2009). The supercontinent rupture slowly migrated northward, extending the margins and thinning the crust by progressive rifting and fault reactivation along ancient Proterozoic suture zones (Torsvik et al., 2009). The oldest resolvable magnetic anomalies at Paraná-Etendeka latitudes suggest that open seafloor spreading in this segment of the crust was established ~ 20 Ma after peak LIP magmatism at ~ 112 Ma (Torsvik et al., 2009; Granot et al., 2015; and references therein). Voluminous intrusions of mafic dykes preceded this transition to open ocean-floor spreading.

^{40}Ar/^{39}Ar geochronology of mafic subalkaline intrusions along the southeastern Brazilian margin reveal possible ages ranging from 155 to 55 Ma (Turner et al., 1994; Renne et al., 1996; Deckart et al., 1998; Raposo et al., 1998; Bennio et al., 2003; Guedes et al., 2005, 2016; Almeida et al., 2021). However, most of the incremental heating spectra available in the published domain lack true age *plateaus* (e.g., Fleck et al., 1977; Schaen et al., 2020; and references therein), which suggests possible alteration, the presence of excess argon, ^{39}Ar recoil, and other features that may question the validity of the geochronological results. Excess Ar is indeed very common in geochronological results obtained from single crystals and whole-rock fragments of mafic dykes (Gomes and Vasconcelos, 2021). The ambiguity of these geochronological results precludes a reliable correlation between magmatism and the various geodynamic processes controlling rift evolution through time. In this study, we combine reliable high-resolution geochronology and magma geochemistry to investigate ages and depth of magma emplacement, magmatic evolution, potential magma sources and emplacement mechanisms, and post-magmatic fluid-rock interactions to show that early oceanization of the southeastern Brazilian margin may be recorded by the transition from LIP- to MORB-type magmatism in mafic dyke swarms intruded along the coast.

We focus here on MORB-like dykes from the Cabo Frio Tectonic Domain, although other occurrences of this magma type have been reported elsewhere along the South America-African coast (Jagoutz et al., 2007; Jourdan et al., 2007). The dykes at Cabo Frio integrate the large Serra do Mar Dyke Swarm, in Southeast Brazil, and they have been the subject of numerous previous studies (Bennio et al., 2003; Schmitt et al., 2016; Almeida et al., 2021). Despite these investigations, their ages are still controversial. Results reported by Bennio et al. (2003) and Almeida et al. (2021) do not meet modern quality assessment criteria: for example, age spectra do not define true *plateaus* according to the older definition of Fleck et al. (1977) or the recently updated criteria of Schaen et al. (2020); isochrons suggest large amounts of excess Ar that question the validity of the results; tentative interpretation of these dubious results as maximum or minimum intrusion ages range by 75 Ma (~130-55 Ma), raising further doubts. Likewise, geochemical results are often not reproducible and show large anomalies in whole-rock LILE concentrations and Sr and Pb isotopic signatures, which leads to contrasting petrogenetic interpretations (Bennio et al., 2003; Almeida et al., 2021). By taking a more conservative approach to the study of these dykes, I intend to resolve some of the current controversies.

1.1. THESIS AIMS

The primary aim of this research thesis is to constrain the onset and dynamics of crustal oceanization in an ancient rift system by evaluating the geochronology and petrogenetic evolution of a set of mafic intrusions from the Cabo Frio Tectonic Domain, closely related to the South Atlantic opening. I have concentrated my efforts on:

- **Critically evaluating geochronological results obtained from intrusive magmatic rocks from the Brazilian southeastern and southern margins by Turner et al. (1994), Renne et al. (1996), Deckart et al. (1998), Raposo et al. (1998), Bennio et al. (2003), Guedes et al. (2005), Florisbal et al. (2014), Guedes et al. (2016) and Almeida et al. (2021),**
- **Defining precise and accurate intrusion ages for the MORB-like dykes from the Cabo Frio Tectonic Domain in order to estimate the timescale of crustal oceanization during Gondwana rifting,**
- **Assessing the validity of geochemical results obtained for the distinct generations and types of mafic dykes in the Cabo Frio Tectonic Domain by evaluating and correcting for the effects of post-magmatic water-rock interaction,**
- **Interpreting only reliable geochemical results to investigate the petrogenesis and possible significant dynamic differences between LIP- and MORB-type magmatism in the Cabo Frio Tectonic Domain and to evaluate the mechanisms controlling the transition from LIP- to MORB-type magmatism during the onset of South Atlantic opening and passive margin evolution,**
- **Incorporating state-of-the-art laser ablation ICP-MS mapping of elemental distribution in clinopyroxene crystals from different magmatic systems to infer magma plumbing systems active during syn-rift magmatism.**

The research encompassed the following steps: (i) assessing the possible causes of the ^{40}Ar/^{39}Ar and whole-rock geochemical anomalies of Cabo Frio Tectonic Domain dykes; (ii) obtaining less ambiguous geochronological and geochemical results for the MORB dykes; (iii) modeling the mantle sources associated with the various magma suites; and (iv) unravelling the mechanisms controlling the ascent, evolution and final emplacement of magmas in the upper crust.

1.2.CRETACEOUS THOLEIITIC MAGMATISM IN CABO FRIO TECTONIC DOMAIN

The Cabo Frio Tectonic Domain, Região dos Lagos, Rio de Janeiro, hosts subalkaline mafic dykes with low TiO_2 contents (LTi) that contrast with the rest of the Serra do Mar Dyke Swarm rocks, which are generally similar to high TiO_2 (HTi) basalts from the Paraná-Etendeka Province (Peate et al., 1992, Marques, 2001; Bennio et al., 2003). They intrude a Paleoproterozoic basement of felsic metagranitoids, diorites and migmatitic and amphibolitic gneisses, and Neoproterozoic sedimentary sequences deformed during collision of the Cabo Frio block with the Ribeira Belt (Búzios Orogeny, between 520-510 Ma; Schmitt et al., 2016; and references therein).

The LTi mafic dykes, the main focus of this investigation, can be grouped into two distinct magma suites: the first one, more primitive, shares many geochemical affinities with South Atlantic N-MORB and E-MORB rocks (normal/enriched mid-ocean ridge basalts; Bennio et al., 2003; Gale et al., 2013; Almeida et al., 2021); the second one, more enriched, is similar to LTi basalts from the Northern Paraná-Etendeka provinces (Bennio et al., 2003; Carvas, 2016; Rocha-Júnior et al., 2020). Analogously to recent rifts, such as the Red Sea (e.g., Ligi et al., 2018; Niu, 2021), MORB magma ascent from the asthenosphere was likely promoted by a local shallow Moho discontinuity (~38 km; Assumpção et al., 2002) resulting from a complex tectonic history (e.g., Fernandes et al., 2015; Schmitt et al., 2008, 2016).

1.3.THESIS OUTLINE

The thesis consists of five chapters: Chapter One defines the problems to be tacked and outlines the various approaches taken to solve these problems; Chapter Two, in the form of a journal article published in 2021 in *Geochimica et Cosmochimica Acta*, focuses on the investigation of the intrusion ages of MORB-like dykes and alteration ages of secondary phases, and on the possible signatures and sources of hydrothermal fluids that may have affected the magmatic rocks; Chapter Three, in the form of a journal article submitted to *Journal of Geophysical Research – Solid Earth*, assesses the distinct mantle sources and magma dynamics of the two Cabo Frio tectonic Domain dyke suites, and the early onset of a passive extensional regime during the emplacement of MORB-like dykes; Chapter Four takes advantage of the large quantity of high-quality geochemical data to evaluate major and minor elemental chemistry of clinopyroxene crystals and assess thermodynamical models of fractional crystallization of LIP- and MORB-like magmas throughout upper crust pressure and temperature conditions; it will be submitted for latter publication, probably in a more local journal (e.g., *Journal of South American Earth Sciences* or *Brazilian Journal of Geology*); Chapter Five, the Conclusions chapter, summarizes what has been achieved with this study and outlines future research directions that follow directly from the data and interpretation presented in the thesis.

CHAPTER 2 – GEOCHRONOLOGY OF MAFIC MAGMATISM AND HYDROTHERMAL ALTERATION DURING EARLY STAGES OF SOUTH ATLANTIC OPENING (PUBLISHED IN GEOCHIMICA ET COSMOCHIMICA ACTA)

Karine Zuccolan Carvas [a], Paulo Marcos de Paula Vasconcelos [b],
Leila Soares Marques a, Teresa Ubide [b], Isabela de Oliveira Carmo [c], Marly Babinski [d]
[a] Instituto de Astronomia, Geofísica e Ciências Atmosféricas, Universidade de São Paulo, Sa˜o Paulo, SP 05508-090, Brazil
[b] School of Earth and Environmental Sciences, The University of Queensland, Brisbane, QLD 4072, Australia
[c] PETROBRAS/CENPES, Rio de Janeiro, RJ 21941-915, Brazil
[d] Instituto de Geociências, Universidade de São Paulo, São Paulo, SP 05422-970, Brazil

Received 29 March 2021; accepted in revised form 16 August 2021; Available online 23 August 2021.
DOI: https://doi.org/10.1016/j.gca.2021.08.017

ABSTRACT

$^{40}Ar/^{39}Ar$ laser incremental-heating geochronology of whole-rock fragments and minerals from primitive subalkaline mafic dykes from the Cabo Frio Tectonic Domain, southeastern Brazil, reveals a complex combination of intrusive ages, apparent ages affected by excess argon, and ages that record late-stage hydrothermal alteration. Incremental-heating analysis of encapsulated magmatic amphibole-biotite clusters reveals a minimum intrusive age of 132.83 ± 0.30 Ma. Sericitized plagioclase crystals show the percolation of K-rich fluids at ~106 Ma. Albitized plagioclase phenocrysts suggest the percolation of Na-rich fluids in the 60–30 Ma interval. Hydrothermal alteration events overlap in time with pulses of alkaline magmatism in the extending Brazilian crust, suggesting a link between magmatic activity and generation of fluid circulation cells along the margin and adjacent sedimentary basins. Evidence for pervasive hydrothermal re-setting of the K-Ar system in the Cabo Frio Tectonic Domain dykes suggests that young $^{40}Ar/^{39}Ar$ geochronology results obtained for mafic dykes here and elsewhere along the continental margins may not record multiple intrusive events, reflecting instead partial or total resetting of the K-Ar system by water-rock interaction during fluid circulation.

2.1. INTRODUCTION

Continental rifts are invariably accompanied by intrusive mafic magmatism, often in the form of dyke swarms, which play an important role in fault reactivation and crustal accretion during plate divergence (Thybo and Nielsen, 2009; Rivalta et al., 2015). By generating or reactivating zones of weaknesses in the crust, dykes affect the rheological behavior of the lithosphere (Lavecchia et al., 2016; and references therein). Dyke swarms ascend through pathways that facilitate magma supply to major extrusive events that accompany continental break-up. To reconstruct the relationship between intrusive mafic magmatism, extrusive magmatism, and continental rifting, information on depth, temperature, source, duration, and rate of magma emplacement is necessary. Acquiring that information is not trivial, however.

^{40}Ar/^{39}Ar geochronology is one of the most commonly applied dating methods to obtain the ages of mafic dykes (McDougall and Harrison, 1999). It has been widely applied to date dykes associated with the Paraná-Etendeka Magmatic Province, but ^{40}Ar/^{39}Ar Ar results from aphanitic dykes are often compromised by the presence of excess argon in whole-rock analyses; results for porphyritic dykes often suggest that the phenochrysts are altered (Gomes and Vasconcelos, 2021). The preferential emplacement of dykes along deep faults prevents magmatic degassing and promotes the incorporation of excess argon; however, when reaching shallower levels, these faults focus fluid migration, promoting fluid-rock interaction and partially modifying the isotopic and geochemical signatures of the dykes (e.g., Kempe et al., 2015). We will show here that mafic dykes associated with Gondwana rifting and opening of the South Atlantic Ocean (Fig. 2.1) are marred by both of these difficulties. We will also show that some of the features (excess argon, hydrous alteration) that pose obstacles to geochronology may nevertheless provide valuable information about the evolution of the rifting continental margin.

Before Gondwana breakup, the flood basalts of the Paraná-Etendeka Magmatic Province covered extensive areas in the southern portion of Brazil, eastern Paraguay, Uruguay, and northern Argentina in South America; and parts of Angola and Namibia in Africa (Piccirillo and Melfi, 1988; Peate, 1997; Thompson et al., 2001; Almeida et al., 2013; and references therein). Peak magmatism occurred at 134.7 ± 2 Ma (Renne et al., 1993, 1996; Thiede and Vasconcelos, 2010), but smaller magmatic events purportedly preceded and post-dated the main phase of extrusion (Mizusaki et al., 1992; Marques et al., 2018 and references therein; Gomes and Vasconcelos, 2021). Mafic dykes associated with the Paraná-Etendeka Magmatic Province are most abundant along the continental margins and areas from where the flood basalts have been eroded (Fig. 2.1). In South America, they cluster in the Ponta-Grossa (PGDS), Florianópolis (FDS), and Serra do Mar (SMDS) dyke swarms (Fig. 2.1), but associated intrusions occur further south in Uruguay (Cuaró dykes, Ures et al., 1997), and as far north as the Parnaíba Basin (Fig. 2.1; e.g., Baksi and Archibald, 1997; Fernandes et al., 2020). In Africa, they occur in the Namibe Basin, Möwe Bay, Doros, South of Brandberg, Horingbaai, and Henjes Bay-Outjo dyke swarms (e.g. Thompson et al., 2001; Ewart et al., 1998).

At face-value, K-Ar and ^{40}Ar/^{39}Ar geochronology indicate that mafic dykes were emplaced before, during, and significantly after the main Paraná-Etendeka volcanic phase. The K-Ar results are dubious and suffer from some of the intrinsic limitations of the method (Vasconcelos et al., 2008), but many of the ^{40}Ar/^{39}Ar results are also ambiguous, show complex K and Ar systematics and suggest that some of the results may not reflect true ages of intrusion. For example, the Florianópolis dykes (Fig. 2.1) yield plagioclase single crystal incremental-heating ages of 129.4 ± 0.6 and 116.4 ± 7.8 Ma (Deckart et al., 1998) or 128.3 ± 0.8 to 119.0 ± 1.4 Ma (all age uncertainties at 1σ; Raposo et al., 1998), substantially younger than extrusive igneous rocks in the area. All age spectra are disturbed by excess argon, and most of the plateaus correspond to less than 50% of the ^{39}Ar released. In contrast, ID-TIMS U-Pb geochronology of three baddeleyite fractions yields a crystallization age of 134.7 ± 0.15 Ma (Florisbal et al., 2014), suggesting that at least some of the Florianópolis dykes are coeval with the main phase of Paraná flood basalt volcanism at ~134 Ma.

The Ponta Grossa dykes (Fig. 2.1) exhibit similar problems. ^{40}Ar/^{39}Ar laser incremental-heating analyses yield whole-rock plateau ages of 134.1 ± 2.6 to 130.4 ± 5.8 Ma (Turner et al., 1994). Turner et al. (1994) suggested that plagioclase alteration to clay minerals along fractures may have led to ^{40}Ar loss, lowering the measured ages. Renne et al. (1996) obtained young plateau ages, ranging from 131.4 ± 1.0 to 129.2 ± 1.0 Ma, for optically pristine plagioclase crystals from the Ponta Grossa dykes. Renne et al. (1996) reported two samples with even younger plagioclase plateau ages (125.8 ± 1.2 and 120.8 ± 1.4 Ma), interpreted as minor intrusive activity related to the full drift stage and ocean basin formation.

^{40}Ar/^{39}Ar geochronology for the Serra do Mar dykes (Fig. 2.1) is also problematic. Turner et al. (1994) obtained ages ranging from 135.8 ± 2.2 to 129.4 ± 1.2 Ma by laser incremental-heating analyses on whole-rock and plagioclase crystals from the central coast of the swarm. Deckart et al. (1998) reported plagioclase age spectra affected by excess argon and the presence of secondary phases; ages ranged from 134.5 ± 0.8 to 129.8 ± 0.4 Ma and were based on flat segments that represent less than 50% of the cumulative ^{39}Ar release, failing to define true plateaus (Fleck et al., 1977). Guedes et al. (2005) also obtained flat segments and plateau ages ranging from 146.8 ± 1.4 to 132.4 ± 0.6 Ma for plagioclase crystals and whole-rock grains from the central portion of the Serra do Mar dykes; all ^{40}Ar/^{39}Ar old results are affected by excess argon. Guedes et al. (2016) reported additional flat segments – not true plateaus – defining ages of 155.4 ± 1.7 and 149.8 ± 1.7 Ma for whole-rock analyses from the same swarm. Isochrons for the same grains confirm the presence of significant excess argon.

The Cabo Frio Tectonic Domain dykes (Schmitt et al., 2016), a northern component of the Serra do Mar dykes, also show significant amounts of excess argon, yielding saddle-shaped incremental-heating spectra. For example, Bennio et al. (2003) reported ^{40}Ar/^{39}Ar maximum ages of 77 ± 14, 54.8 ± 0.6 and 55.2 (uncertainty not provided) Ma for plagioclase crystals from tholeiitic dykes from Cabo Frio (Fig. 2.1). The pronounced saddled-shape spectra suggest large amounts of excess argon; the absence of statistically valid age plateaus or isochrons makes it impossible to evaluate the accuracy of these results.

More recently, Almeida et al. (2021) reported ^{40}Ar/^{39}Ar results for plagioclase crystals from four Cabo Frio Tectonic Domain dykes. The samples analyzed failed to provide reproducible results and flat segments do not yield plateaus as defined by Fleck et al. (1977); some are incorrectly identified as ‘‘integrated age”. The reported magmatic ages (130.3 ± 11.0 and 120.6 ± 6.0 Ma) are averaged from results that range by as much as 30 Ma.

The wide range in the ^{40}Ar/^{39}Ar ages reported for Serra do Mar tholeiitic dykes (~155 to ~55 Ma) may indicate that mantle thermal anomalies and crustal extension started early in the history of Gondwana breakup, long before massive extrusion of continental flood basalts (Rocha-Júnior et al., 2013, 2020). The geochronological data may also suggest that intrusive magmatism was coeval with flood basalt volcanism and may have lasted for a long time after continental breakup because of persistent thermal anomalies and/or fault reactivation. Alternatively, the results may indicate that the ^{40}Ar/^{39}Ar system in some of these mafic dykes is complex and susceptible to excess argon and post-magmatic alteration, where the interpreted results may not reflect true ages of magma emplacement. Similar ambiguities are present in ^{40}Ar/^{39}Ar results for mafic dykes emplaced during Gondwana breakup in other regions of South America and Africa (e.g., Baksi and Archibald, 1997; Marzoli et al., 1999; Gomes and Vasconcelos, 2021). Unfortunately, confirming ^{40}Ar/^{39}Ar ages with U-Pb results, as done by Florisbal et al. (2014), is not always possible due to the absence of suitable minerals.

Figure 2.1. A – Map of the Paraná-Etendeka Magmatic Province (PEMP) during early stages of South Atlantic expansion (Piccirillo and Melfi, 1988; Machado et al., 2015). SM: Serra do Mar dyke swarm. PG: Ponta Grossa dyke swarm. FL: Florianópolis dyke swarm. B – Cabo Frio Tectonic Domain, in Região dos Lagos (Schmitt et al., 2016), where all samples investigated here were collected. The four samples selected for $^{40}Ar/^{39}Ar$ geochronology and Sr, Nd and Pb isotope analyses are highlighted. C – Dyke LM-DA-BZ-5, from Armação dos Búzios. D – Dyke LM-DA-150, from Arraial do Cabo. E – Dyke LM-DA-206, from Armação dos Búzios. F – Dyke LM-DA-203, from Cabo Frio.

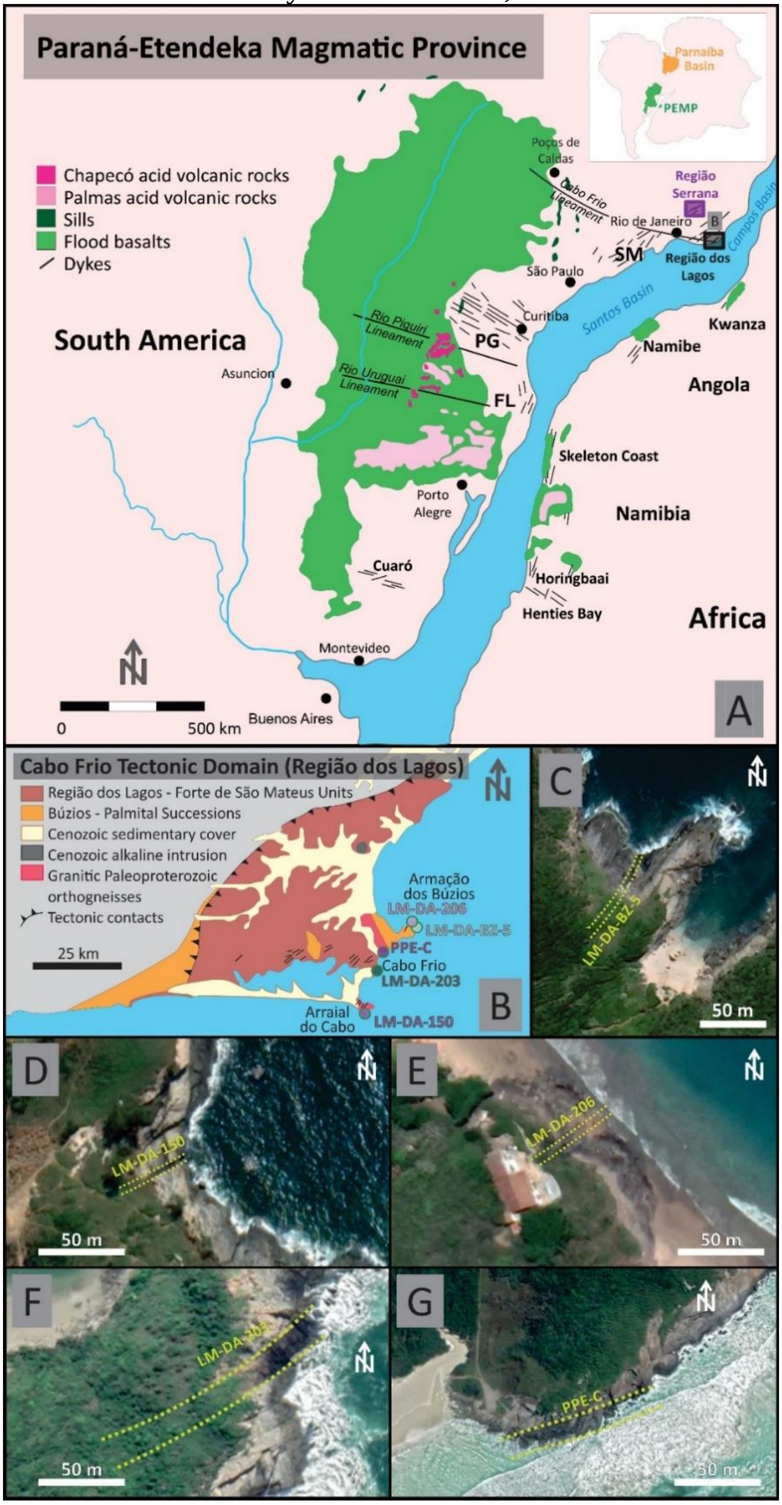

(Carvas et al., 2021)

In order to devise an approach for properly dating mafic dykes by the ^{40}Ar/^{39}Ar laser-heating method, to identify and possibly overcome difficulties associated with alteration and excess argon, and possibly derive useful geological information from the altered dykes, we sampled and analyzed distinct phases from four Serra do Mar dykes, located within the Cabo Frio Tectonic Domain. These dykes are ideal targets because of the presence of both altered and unaltered K-bearing phases, and their previously measured saddle-shaped age spectra (Bennio et al., 2003) and variable ages (Almeida et al., 2021).

We also investigated the dykes for whole-rock major, minor, trace element, and isotopic geochemistry to determine potential fluid-rock interactions during dyke ascent, emplacement, and exhumation. In addition, major and trace element electron microprobe data and laser ICP-MS elemental mapping of single crystals of plagioclase helped to identify specific fluid-rock interactions recorded within the mineral. Identifying and possibly dating alteration events make it possible to investigate water-rock interaction as the crust extended due to rheological changes during and after supercontinent breakup.

2.2. GEOLOGICAL CONTEXT

2.2.1. REGIONAL TECTONICS

All dykes investigated here were emplaced in the Região dos Lagos, within the Cabo Frio Tectonic Domain (CFTD; Fig. 2.1), a block that collided with the Ribeira belt during the Búzios Orogeny (520 to 510 Ma) and was later fragmented by Cretaceous rifting (Schmitt et al., 2016; and references therein).

The CFTD Paleoproterozoic basement rocks record low-angle deformation and low- to medium-pressure metamorphism and comprise two main groups: felsic metagranitoids, diorites and migmatitic gneisses from the Região dos Lagos Unit; and amphibolitic banded gneisses from the Forte de São Mateus Unit (~1970 Ma protoliths; ~520 Ma metamorphism; Schmitt et al., 2004). The Búzios and Palmital Units, which also host some of the dykes investigated in this study, are amphibolitic, calcium-silicate and quartz-feldspar meta-igneous and -sedimentary complexes that represent ocean floor deformed during the Búzios Orogeny (~500 Ma; Schmitt et al., 2004, 2016; and references therein).

The collision, subduction and extension events that affected the CFTD have probably decreased its crustal strength and thickness; in fact, receiver function seismology indicates a shallow Moho discontinuity (~38 km; Assumpção et al., 2002; Schmitt et al., 2016). Additionally, NE-SW-oriented magnetic and gravimetric anomalies following basement structural trends can be traced from the CFTD onshore to the Santos Basin offshore, suggesting that intrusive magmatism was more intense bellow the thinned crust and extended into marginal basins (Oreiro et al., 2008; Stanton et al., 2010). Extensional tectonism resulted from simultaneous fault reactivation and magma ascent, a combination that potentially minimized the stresses required for continental breakup (Lavecchia et al., 2016).

2.2.2. THE CABO FRIO TECTONIC DOMAIN DYKES WITHIN THE SERRA DO MAR DYKE SWARM

The Serra do Mar dyke swarm extends along São Paulo and Rio de Janeiro, southeastern Brazil (Fig. 2.1), and it comprises vertical/sub-vertical NE-SW dykes that follow basement structural trends (Corval et al., 2008). The dykes are either high- (HTi: $TiO_2 > 2$ wt%) and low-Ti (LTi: $TiO_2 < 2$ wt%) tholeiites, sharing similarities with HTi Pitanga-Urubici and LTi Esmeralda-Gramado basalts from the Paraná-Etendeka Magmatic Province (e.g., Bellieni et al., 1990; Peate et al., 1992). The LTi dykes represent only ~10% of the swarm and occur in the Regia˜o dos Lagos, in the CFTD, and in the Região Serrana of Rio de Janeiro, within the Serra do Mar mountains (Fig. 2.1; e.g., Corval et al., 2008).

According to Bennio et al. (2003), the dykes in the CFTD are subalkaline, with trace element and Sr isotopic signatures that preclude significant crustal assimilation, and comprise two distinct magmatic suites: group A, more primitive ($SiO_2 < 52$ wt%; MgO > 5.5 wt%; $145 \leq [Sr] \leq 229$ ppm; $66 \leq [Zr] \leq 114$ ppm; $0.70426 \leq {}^{87}Sr/{}^{86}Sr_i \leq 0.70434$ and $0.51659 \leq {}^{143}Nd/{}^{144}Nd_i \leq 0.51267$); and group B, more evolved ($SiO_2 > 52$ wt%; MgO < 6 wt%; $227 \leq [Sr] \leq 264$ ppm; $93 \leq [Zr] \leq 154$ ppm $0.70548 \leq {}^{87}Sr/{}^{86}Sr_i \leq 0.70613$ and $0.51238 \leq {}^{143}Nd/{}^{144}Nd_i \leq 0.51239$). Simple mixing, assimilation, and fractional crystallization models do not show petrogenetic relationships between the two suites (Bennio et al., 2003).

Precise emplacement ages of the CFTD dykes are relevant to understand continental rifting as their SW-NE direction is parallel to the continental margin, which suggests a close relationship with rift faulting. Their location also coincides with the coastal extension of the Cabo Frio Lineament, a 500 km-long WNW-ESE series of 85 to 50 Ma syenitic-carbonatitic plutons and alkaline dykes between Poços de Caldas, Minas Gerais, and Cabo Frio, Rio de Janeiro (Fig. 2.1). According to Ferroni et al. (2017), this magmatic series marks the reactivation of a deep lithospheric fracture zone during seafloor spreading. Magmatic activity along this trend continued into the offshore basins, comprising the Alto do Cabo Frio magmatism (Stanton et al., 2010; Oreiro et al., 2008).

2.3. SAMPLING AND ANALYTICAL PROTOCOLS

Twelve tholeiitic dykes (Table 2.1) were sampled at Arraial do Cabo, Cabo Frio and Armação dos Búzios (Fig. 2.1B), within the CFTD. The dykes range from small aphanitic bodies (tens of cm wide) to large (up to 20 m wide) intrusions that are holocrystalline and equigranular in the center, and aphanitic at the chilled margins. Samples were collected from non-weathered and xenolith-free central zones of > 3 m dykes, except for dyke PPE-C, sampled both at the margin (PPE-C1) and the center (PPE-C3). Most of the intrusions trend N40°E-N70°E (Fig. 2.1).

All dykes are visually free from weathering (no dissolution cavities, no iron oxyhydroxide staining, no visible clay minerals, etc.). However, they exhibit both sericitized (milky white) and apparently pristine (clear and transparent) plagioclase phenocrysts (500–1000 µm). One of them (LM-DA-203) also contained considerable amounts of amphibole and biotite (~5% of the assemblage). Four of the dykes – LM-DA-BZ-5, LM-DA-203, LM-DA-150 (highlighted in Table 2.1), and PPE-C – were dated by ^{40}Ar/^{39}Ar geochronology. Eleven of the dykes were investigated by a comprehensive set of additional analytical methods: optical microscopy for general petrographic characterization; scanning electron microscopy (SEM) and electron probe microanalysis (EPMA) for mineral identification and composition; X-ray fluorescence (XRF) for whole-rock major and minor element composition; inductively coupled plasma mass spectrometry (ICP-MS) for whole-rock trace element composition; and thermal ionization mass spectrometry (TIMS) for Sr and Nd isotopic composition. Because of its phenocryst assemblage (clear plagioclase, milky plagioclase, clinopyroxene, olivine, amphibole, biotite, and magnetite phenocrysts), dyke LM-DA-203 was targeted for detailed geochronology and mineral-specific trace-element mapping by laser ablation ICP-MS (LA-ICP-MS).

Table 2.1. Location, coordinates, thickness, and analytical methods used in the investigation of each of the 12 CFTD dyke samples.

Sample	Locality	Latitude	Longitude	Thickness (m)	Analytical methods
LM-DA-BZ-4	Armação dos Búzios	S22°45'17.8"	W41°51'54.8"	0.8	XRF; ICP-MS
LM-DA-BZ-5	Armação dos Búzios	S22°45'17.8"	W41°51'54.8"	3	XRF; ICP-MS; Sr, Nd, Pb isotopes, ^{40}Ar/^{39}Ar geochronology
LM-DA-150	Cabo Frio	S22°56'46.6"	W42°01'42.3"	2.5	XRF; ICP-MS; Sr, Nd, Pb isotopes; ^{40}Ar/^{39}Ar geochronology
LM-DA-158	Arraial do Cabo	S22°57'31.2"	W41°01'34.7"	1.5	XRF; ICP-MS
LM-DA-182	Armação dos Búzios	S22°59'25.5"	W42°00'51.5"	-	XRF; ICP-MS
LM-DA-203	Cabo Frio	S22°52'17.9"	W41°58'47.2"	20	XRF; ICP-MS; Sr, Nd, Pb isotopes; ^{40}Ar/^{39}Ar geochronology
LM-DA-204	Cabo Frio	S22°52'16.2"	W41°58'59.0"	3	XRF; ICP-MS
LM-DA-205	Armação dos Búzios	S22°46'10.0"	W41°52'37.1"	2.5	XRF; ICP-MS
LM-DA-206	Armação dos Búzios	S22°45'11.2"	W41°52'26.4"	1	XRF; ICP-MS; Sr, Nd, Pb isotopes
LM-DA-208	Armação dos Búzios	S22°45'06.6"	W41°53'47.6"	1.5	XRF; ICP-MS
LM-DA-210	Armação dos Búzios	S22°59'36.6"	W42°00'51.5"	2.5	XRF
PPE-C	Cabo Frio	S22°49’22.1’’	W41°58’8.2’’	20	^{40}Ar/^{39}Ar

2.3.1. ^{40}AR/^{39}AR GEOCHRONOLOGY

Basic mineral characterization, including the identification of alteration phases, preceded geochronological analysis; it included transmitted- and reflected-light optical microscopy (Nikon Eclipse E400 POL) and electron microscopy/EDS analysis (Hitachi Tabletop Scanning Electron Microscope TM3030 equipped with a Bruker Energy Dispersive Spectroscopy detector) on polished thin sections from four selected samples. Mineral separation was carried out at the Institute of Astronomy, Geophysics and Atmospheric Sciences and the Institute of

Geosciences, University of São Paulo, Brazil, and at the University of Queensland Argon Geochronology in Earth Sciences (UQ-AGES) laboratory.

After removing weathered surfaces with an alumina grindstone (Al_2O_3), we crushed the samples selected for $^{40}Ar/^{39}Ar$ analyses to 80–150 mesh using a jaw crusher and a stainless-steel mortar-and-pestle. Magnetic and density mineral separation was carried out with hand magnets, a Frantz separator, and bromoform (2.81 g/cm^3). For sample LM-DA-BZ-5, 0.2–2 mm sericite-free (clear) and sericitized (milky white) plagioclase crystals and visually unaltered whole-rock fragments were handpicked. For sample PPE, sericitized (milky white) plagioclase crystals and whole-rock fragments were handpicked. For samples LM-DA-150 and LM-DA-203, 5–8 mg of 80–150 mesh sericite-free (clear) and sericitized (milky white) plagioclase crystals were handpicked and vacuum-encapsulated in 1 mm ID and 2-mm OD Si capillaries. Pristine amphibole and biotite aggregated grains from sample LM-DA-203, ranging from 100 to 150 µm, were also hand-picked and encapsulated in Si capillaries. Capsules were pumped for eight hours to 10-8 Torr and sealed with a methane-O_2 torch, following the procedures of Ren and Vasconcelos (2019). Vacuum-encapsulation helped to test whether the fine-grained samples were susceptible to significant ^{39}Ar recoil losses.

Single crystals and rock fragments were inserted into individual wells in high-purity Al irradiation disks together with Fish Canyon sanidine fluence monitors (accepted age of 28.201 ± 0.046 Ma; Kuiper et al., 2008) and GA1550 biotite as a secondary standard (98.8 ± 0.5 Ma; Renne et al., 1998), following the geometry illustrated in Vasconcelos et al. (2002). The encapsulated samples were inserted into hollow wells in a stack of five aluminum disks, where the lowermost disk was not hollow and held Fish Canyon monitors at the bottom of the wells, in the same horizontal level as the grains in the capsules, as illustrated in Ren and Vasconcelos (2019). The disks were wrapped in Al-foil, sealed into a silica capsule containing up to 11 Al disks, and irradiated for 14 hours in the Cd-lined B-1 CLICIT facility at the Oregon State University TRIGA reactor, USA.

After irradiation, noble gas mass spectrometry was performed in a fully automated MAP-215–50 mass spectrometer equipped with a Balzers 217 electron multiplier at UQ-AGES. The individual crystals of GA1550 biotite were irradiated in the same disks as our samples and were analyzed separately. They yielded flat spectra and reproducible plateau, isochron, and kernel density probability ages (Table 2.2; plots are available in supplementary material A). All results are indistinguishable from the proposed values for this international standard (Renne et al., 1998; Spell and McDougall, 2003), attesting to the reliability of the procedures.

Table 2.2. GA1550 results.

Sample	Plateau			Isochron				Probability density plot	
	Age	MSWD	Steps	Age	MSWD	Steps	Intercept	Mean weighed age	MSWD
9240-01	98.83 ± 0.32	1.67	10	98.70 ± 0.35	1.6	16	295.2 ± 7.8	98.70 ± 0.14	1.55
9240-02	98.55 ± 0.36	1.63	10						
7474-01	98.49 ± 0.41	0.7	9	98.50 ± 0.37	0.89	19	296.0 ± 17	98.49 ± 0.18	0.85
7474-02	98.49 ± 0.50	1.13	10						
7495-01	99.15 ± 0.63	1.42	9	98.87 ± 0.58	1.4	19	292.0 ± 34	98.63 ± 0.27	1.04
7495-02	98.36 ± 0.65	0.52	10						
7516-01	98.85 ± 0.61	1.05	10	98.65 ± 0.54	1	19	291.0 ± 14	98.82 ± 0.50	0
7516-02	98.44 ± 0.59	0.82	9						

The capsules containing plagioclases from samples LM-DA-203 and LM-DA-150 were drilled with a Lambdaphysik MINex Excimer KrF laser so that any possible ^{39}Ar dislodged from the crystals by recoil or heating during irradiation could be analyzed prior to the step-heating procedure. Once the capsules had been pierced and the first step from each capsule had been analyzed, the same sample chamber containing the copper disks with the capsules was placed under a Coherent Verdi 10 W diode laser, where the grains were incrementally heated by a 2-mm wide laser beam programmed to progressively travel along the Si-capsules containing the grains. Single crystals and whole-rock fragments from samples LM-DA-BZ-5 and PPE-C were also incrementally heated with a Coherent Verdi 10 W diode laser with a similar 2-mm beam.

The fractions of gas released by piercing or incremental heating passed through a cryocooling device operated at -130 °C (H2O and CO2 removal) and two SAES C-50 getter pumps, the first at ~475 °C and the second at room temperature. The gas was then expanded into the mass spectrometer, equipped with a third SAES C-50 getter pump. One sequence of three blanks and one air-pipette shot (in the order blank-air-blank-blank) was analyzed before and after each sample to monitor background values and to quantify Ar isotope discrimination (assuming the atmospheric ^{40}Ar/^{36}Ar value of 298.56 ± 0.31 of Lee et al., 2006).

J-factors for each Al-disk were calculated from the laser total-fusion analyses of 15 individual aliquots (1–3 individual grains) of Fish Canyon sanidine grains. Irradiation parameters, Ar isotope discrimination, atmospheric gas contributions, and blanks and baseline corrections were calculated using the Mass Spec software (Deino, 2012). The ages and associated uncertainties were determined by propagating measured Ar isotope values to time zero with either linear or parabolic regressions, subtracting the values for blanks and baselines, and correcting for discrimination and errors in the J parameter and irradiation parameters. The results for discrete analysis from each grain were plotted in % cumulative ^{39}Ar released versus apparent age spectra, and age plateaus were defined as at least three consecutive steps yielding apparent ages within 2σ error from the variance-weighted mean, comprising 50% or more of total ^{39}Ar released (Fleck et al., 1977).

2.3.2. MAJOR, MINOR AND TRACE ELEMENT WHOLE-ROCK ANALYSES

In order to evaluate geochemical characteristics and possible alteration effects on the chemistry of the different dykes, we prepared whole rock fractions of 11 dykes for major, minor, and trace element, and Sr, Nd and Pb isotope analyses at the Institute of Astronomy, Geophysics and Atmospheric Sciences, University of São Paulo. Samples were crushed in fragments of less than 0.5 cm diameter using a hydraulic press and a stainless-steel jaw crusher with the same procedures described in Marques et al. (2016). After quartering, samples were washed with double distilled water, ultrasonicated in purified 0.1M HNO_3 and deionized water, and later dried inside clean boxes in a class 10,000 clean room (Marques et al., 1999, 2016). The fragments were then pulverized using an agate mill (Marques et al., 2016).

Major and minor oxide analyses were performed at the XRF Laboratory of the Universidade Estadual Paulista (UNESP-Rio Claro), following procedures described by Nardy et al. (1997) and Machado et al. (2015). Reference basalts BHVO-2 and BE-N were analyzed as primary standards with major and minor element accuracies better than 7%, with typical values ranging between 1 and 3% (supplementary material B).

Rare earth and other trace elements (Cr, Ni, Ba, Rb, Sr, Zr, Y, Nb, Ta, Th, U, Pb, Hf, Sc, Co) were analysed with ICP-MS at the Geochemistry Laboratory, Universidade Estadual de Campinas. Replicate analyses of the BRP-1 reference material (a basalt rock from the Northern portion of the Paraná-Etendeka Province; Cotta and Enzweiler, 2008) showed that the accuracy was better than 10% for most of the elements; Rb (26%) and Cr (46%) are exceptions (supplementary material C).

Four representative samples were analysed for Sr and Nd isotope compositions by thermal ionization mass spectrometry at the Institute of Geosciences, University of São Paulo. The rock powders (100 mg) were dissolved in Savillex beakers with HF and HNO_3 on a hot plate for 5 days at ~110 °C and were dried down on a hot plate; the residue was dissolved in 6 M HCl at

110 °C for 24 hours. The HCl solution was dried down and concentrated HNO_3 was added on the residues. Samples were taken to dryness prior to re-dissolution for ion exchange purification.

Sr was purified using Eichrom Sr-Spec® resin and eluted with 0.05 M HNO_3. A Triton TIMS (thermal ionization mass spectrometer) in dynamic mode was used for Sr isotope analysis (normalization ratio $^{86}Sr/^{88}Sr = 0.1194$ and analytical blank values of 119 pg), with an accuracy of 0.015% for NBS-987 standard ($^{87}Sr/^{86}Sr = 0.710237 \pm 0.000024$, total of 33 analyses from May/2015 to March/2016. Samples were analysed in March/2016).

Nd was purified using two sets of ion-exchange columns with RE-Spec® and LN-Spec®; Nd was eluted in 0.26 M HCl. Isotope ratios were measured in a Thermo Neptune ICP-MS (normalization ratio $^{146}Nd/^{144}Nd = 0.7219$ and blank values were below 40 pg) with an accuracy of 0.0012% for the JNdi-1 standard ($^{143}Nd/^{144}Nd = 0.51208\ 6 \pm 0.000006$, n = 20).

2.3.3. CHEMICAL CHARACTERISTICS OF PLAGIOCLASE AND SECONDARY PHASES

Altered plagioclase crystals were initially characterized on polished thin sections by electron microscopy (Hitachi SU3500 Scanning Electron Microscope equipped with an Energy Dispersive Spectroscopy system; SEM-EDS) in the Centre for Microscopy and Microanalysis (CMM), University of Queensland. Major element compositions were measured by Electron Probe Microanalysis (EPMA) with a JEOL JXA-8200 Wavelength Dispersive X-ray Spectrometer (WDS) and EDS instrument at CMM-UQ. Thin sections were carbon-coated and analyzed under high-vacuum at an accelerating voltage of 15 kV, a 2 mm diameter electron beam, 15nA beam current, and counting times of 10 s on peak and 5 s on each of two background positions.

The WDS system was calibrated using the following Micro-Analysis Consultants crystals: albite-t-ox (Al-TAP, Na-TAP), P140-olivine (Mg-TAP), wollastonite-t (Si-TAP, Ca-PETJ), orthoclase-1 (K-PETJ), spessartine-ox (Mn-LIF), chromite-t-ox (Fe-LIF, Cr-PETJ), Ni-olivine-G (Ni-LIF), apatite-t (P-PETJ), rutile-ox (Ti-PETJ); all in Ka position. Matrix effects were corrected using the ZAF procedure (Z – atomic number; A – absorption; F – fluorescence). The international reference materials Kakanui hornblende, Kakanui augite, Lake Co feldspar, VG2 basaltic glass and Springwater olivine were used to monitor the accuracy of analyses of unknowns. Accuracy was typically better than 1–5%, except for elements with abundances below 1%, for which accuracy was better than 20%. Plagioclase phenocrysts were analyzed along transects. All oxide results with analytical totals between 98–102% were then manually corrected with the calibration factors obtained for the standards. The final data was screened through stoichiometry tests for calcic plagioclase; the final dataset comprises 228 major element analyses (supplementary material D).

Major, minor and trace element maps (Ca, Si, Fe, K, Na, Ba, Li, Rb, Sr, Pb, U, La, Ce, Nd, Sm, Yb) were generated by LA-ICP-MS at the University of Queensland Centre for Geoanalytical Mass Spectrometry, Radiogenic Isotope Facility (UQ RIF Lab), following the methodology developed by Ubide et al. (2015, 2019a). Thin sections were loaded in a dual-volume Laurin Technic ablation cell controlled by GeoStar Norris software. We ablated the plagioclase crystals and surrounding groundmass using an ASI RESOlution 193 nm excimer UV ArF laser system and progressively moved the sample stage under the fixed laser beam to produce uniform ablated lines with overlapping squares (3 J/cm^2 fluence, 10 x 10 µm square mask, 10 µm/s translation speed, 10 Hz repetition rate, 1 µm overlap between rasters). Pre-ablation was performed with a 100 x 100 µm laser aperture, 200 mm/s speed and 20 Hz to enhance laser-crystal coupling. Ablation took place in an ultrapure He environment (350 mL/min flow), and Ar (850–950 mL/min) and N_2 (5 mL/min) flows in the plasm torch promoted efficient ionization and transport.

Elemental data were measured in a Thermo iCap RQ quadrupole mass spectrometer, and instrument calibration used the NIST612 glass reference material. Elemental maps were processed with Iolite v.2.5 (Paton et al., 2011) in quantitative mode. NIST612 was used as calibration standard, and the EPMA average calcium concentration in plagioclase phenocrysts (15.99 ± 1.48 wt% CaO) was used as internal standard because of the low CaO variation in comparison with other major elements (including SiO_2). For this reason, the results are quantitative for plagioclase crystals, and semi-quantitative for other phases. Accuracy and precision were calculated using BHVO-2G and BCR-2G glasses as secondary standards. Precision was better than 5% and accuracy was better than 5–10% for all trace elements. We also measured K and Fe to track relative variations in the mapped areas; results from these elements were treated as semi-quantitative.

We used the Monocle add-on for Iolite (Petrus et al., 2017) to estimate the compositions of selected crystal zones (supplementary material E). We based the selections on Ca and Fe zoning and defined polygons of homogeneous composition (i.e., where standard deviations were lowest). This approach returned compositions of high precision relative to spot analyses.

2.4. RESULTS

2.4.1. PETROGRAPHY OF SAMPLES INVESTIGATED BY ^{40}AR/^{39}AR GEOCHRONOLOGY

The dykes are holocrystalline and ophitic and have olivine diabase composition (Le Maitre et al., 2002), comprising mostly plagioclase, pyroxene, magnetite, ilmenite, olivine, biotite and amphibole. Most intrusions are porphyritic, with plagioclase, pyroxene and minor olivine, amphibole or biotite phenocrysts in a microcrystalline matrix of plagioclase, pyroxene and magnetite microlites. The central portions of wide dykes (>5 m wide) are equigranular. Partially altered rocks contain chlorite, pyrite, chalcopyrite and sericite. Chloritization is significant in one of the dykes (LM-DA-210), and sericitization occurs in most of them, mainly in plagioclase bytownitic cores, which are cloudy. Labradoritic compositions occur in phenocrysts rims and microlites, and rarely display any sericitization. The intensity of sericitization varies between dykes.

Selected images of the samples analyzed by ^{40}Ar/^{39}Ar geochronology are available in Fig. 2.2. Dyke LM-DA-203 is porphyritic along the borders and equigranular in the center, it is incipiently altered, and it contains plagioclase crystals with few fractures and magnetite, pyroxene, pyrite and apatite inclusions (Fig. 2.2C, D). Partial sericitization, if present, occurs in plagioclase cores and it results in lower average mineral density, as shown by the darker gray tones in backscattered images (Fig. 2.2A, B). Sericite is often associated to exceedingly small quartz crystals and albitized zones. Most of the fractures are filled with Fe and Mg-rich phases.

Some clear plagioclase phenocrysts show irregular rims marked by Na-enrichment and Ca-depletion that define albitized zones (6–11 wt% Na2O, against 1–5 wt.% in sectors without enrichment), only noticeable in backscatter electron images, EDS analyses and LA-ICP-MS elemental maps (Section 2.4.2). Narrow Na-rich zones also occur in central regions of the crystals, next to fractures (Fig. 2.2D). Plagioclase microlites in the matrix are not altered.

Figure 2.2. A – Cross-polarized photomicrograph of a sericitized (Ser) plagioclase phenocryst (Pl) from the border region of the dyke where LM-DA-203 was collected, along with magnetite (Ti-Mag) in a fine-grained matrix. B – Backscattered image of A. C - Cross polarized photomicrography of a clear partially albitized plagioclase phenocryst (Pl) in sample LM-DA-203 (center of the dyke), along with titanomagnetite (Ti-Mag), clinopyroxene (Cpx) and partially chloritized (Chl) olivine (Ol). D – Backscattered image of C. Albitization zones occur randomly in borders and along fractures; some of them are highlighted. E - Cross-polarized photomicrograph of an amphibole (Amp) crystal close to the border of the same dyke. Plagioclase, clinopyroxene and titanomagnetite phenocrysts are also shown. F – Backscattered image of the boxed region in E. A residual rim of the original clinopyroxene is highlighted.

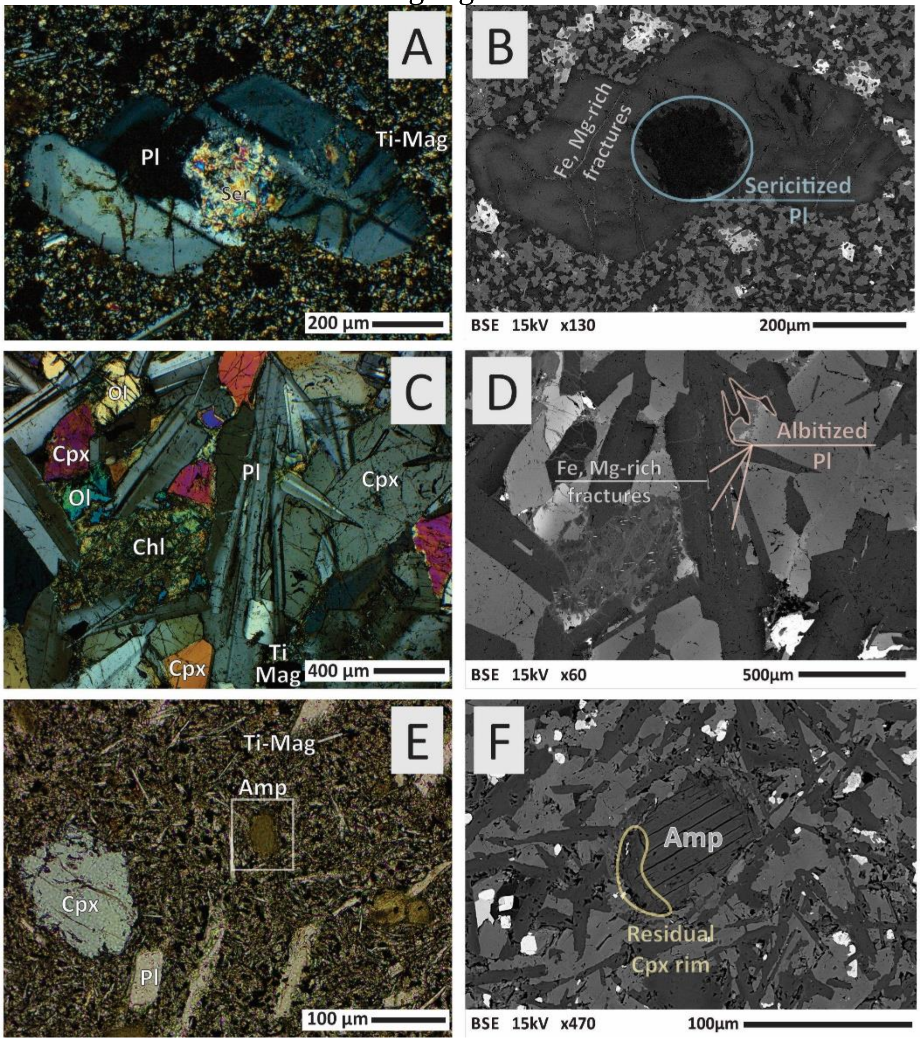

(Carvas et al., 2021)

Similar petrographic features are present in the other three samples. Dyke LM-DA-BZ-5 is porphyritic, and its plagioclase phenocrysts are either unaltered or pervasively sericitized in the core. They host magnetite, pyroxene, and pyrite inclusions. Irregular Na-rich zones are detectable by SEM/EDS analysis in many of the plagioclase phenocrysts (supplementary material K). The plagioclase microlites are unaltered.

Sample LM-DA-150 is porphyritic, with plagioclase phenocrysts showing pervasive core replacement by sericite and hosting apatite and sulfide inclusions (supplementary material K). They also show irregularly albitized zones. Sulfide crystals occur in the microcrystalline matrix, and no alteration is detectable in plagioclase microlites.

Lastly, dyke PPE-C is porphyritic at the border (PPE-C1; glass matrix) and equigranular with occasional plagioclase aggregates in the center (PPE-C3) (supplementary material K). In both PPE-C1 and PPE-C3, plagioclase phenocrysts and microlites are highly fractured, pervasively sericitized and display numerous apatite and sulfide inclusions. Na-enrichment in crystal rims and cores produce an irregular zonation pattern.

Additional petrographic images of plagioclase crystals from each of the dated samples are provided in supplementary material L.

2.4.2. LASER ABLATION ICP-MS MAPPING

LA-ICP-MS maps of Ca, Si, Fe, K, Na, Ba, Li, Rb, Sr, Pb, U, Sm, Nd, La and Yb concentrations for two representative altered plagioclase crystals from sample LM-DA-203 are shown in Figs. 3 and 4. Additional Ce maps are available on supplementary material F. Crystal I (Fig. 2.3) is embedded in a fine groundmass and its primary composition ranges from bytownite (core) to labradorite (rims). Sericite occurs in the core and in the vicinity of minor fractures. Major, minor and trace element maps show evidence for sericitization. The maps also show that LREEs (La, Ce etc.) were more affected by fluid percolation than HREEs (e.g., Yb). In crystal II (Fig. 2.4), primarily labradorite, albitization occurs as irregular rims and along fractures.

Independently of whether the crystal is sericitized or albitized, alteration is marked by an increase in Na, K, Si, and Fe and a decrease in Ca. Some fractures are filled with Si, Fe, Na and K-rich phases, but alteration penetrates beyond the fractures into the crystals and reveal solution-feldspar cation exchange (especially noticeable in Ca and Na maps, Fig. 2.4). The LA-ICP-MS analyses also show that sericitization is accompanied by Ba, Li, Rb, Sr, Pb, Na, and, to a lesser extent, Sm, Nd and La enrichment; albitization also shows Ba, K, Li, Sr and Pb enrichment. Li and Pb are particularly enriched along fractures.

Figure 2.3. Backscattered electron images and LA-ICP-MS elemental maps of the sericitized plagioclase crystal I (also shown in Fig. 2.2A, B) from sample LM-DA-203, collected at the border of the dyke, where the texture is porphyritic. Colour scales reflect concentration values in plagioclase (parts per million), except for the Ca map, which represents signal intensity (counts per second; internal standard). Analyses are quantitative for plagioclase and semi-quantitative for other phases in the groundmass.

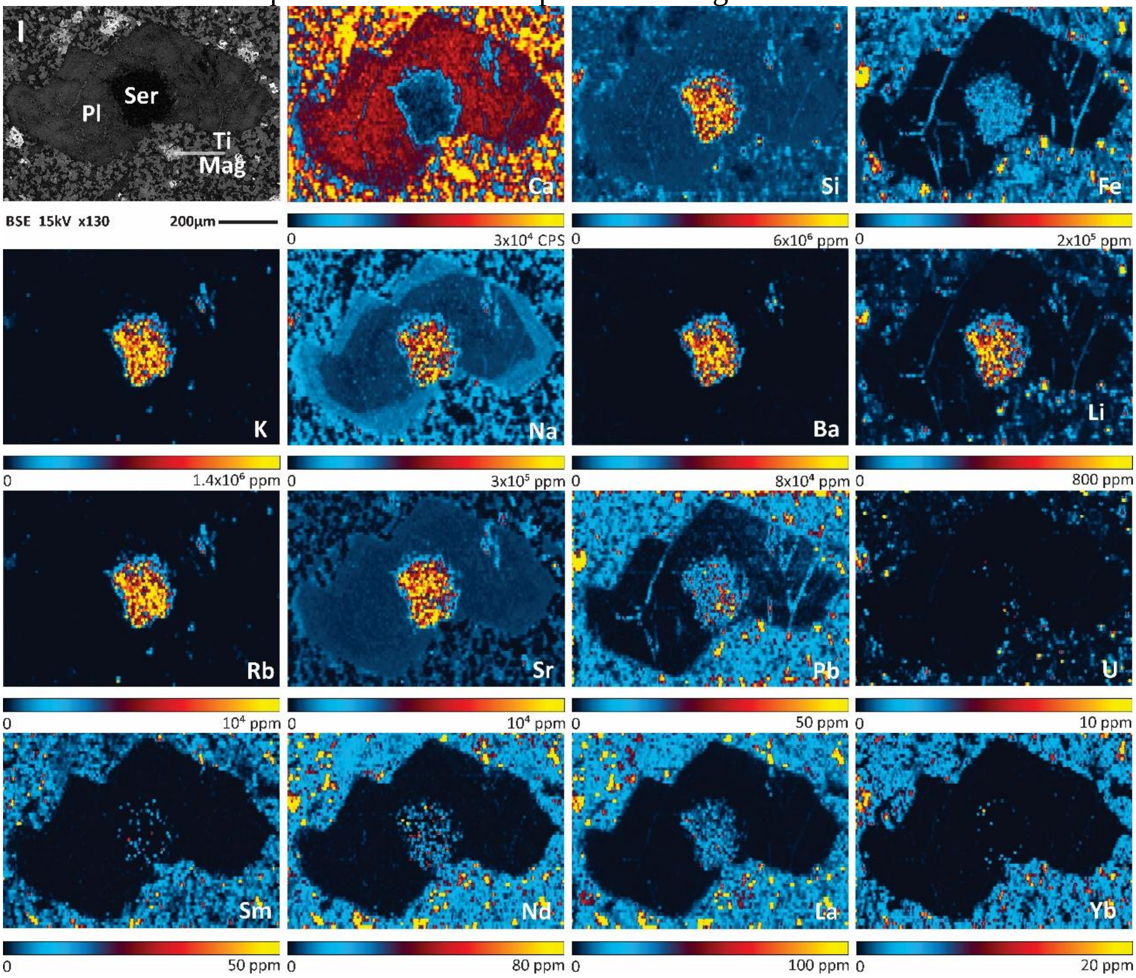

(Carvas et al., 2021)

Elemental enrichment in the alteration zones and fractures in crystals I and II (Figs. 2.3 and 2.4, respectively) is quantitatively evaluated in Fig. 2.5, in which average elemental concentrations were extracted from altered zones and normalized by the calcic plagioclase average values. The average values, ratios and figures of the selected regions are available in supplementary material E. Sm, Yb and U were excluded from the plots due to their high average uncertainties, which result from the low and scattered signals within the alteration zones and fractures.

The sericitized core in crystal I (Fig. 2.5) is enriched in all analyzed elements when compared to the pristine plagioclase. Rb, Ba, K and Li are particularly enriched in sericitized zones. Albitized zones in crystal II are also enriched in all elements when compared to the pristine crystal, but to a lesser degree.

Figure 2.4. Backscattered electron images and LA-ICP-MS elemental maps of the albitized plagioclase crystal II (also shown in Fig. 2.2C, D) from sample LM-DA-203. Plagioclase is bordered by olivine, chlorite, and clinopyroxene. Colour scales reflect concentration values in parts per million, except for the Ca map which represents signal intensity (counts per second; internal standard).

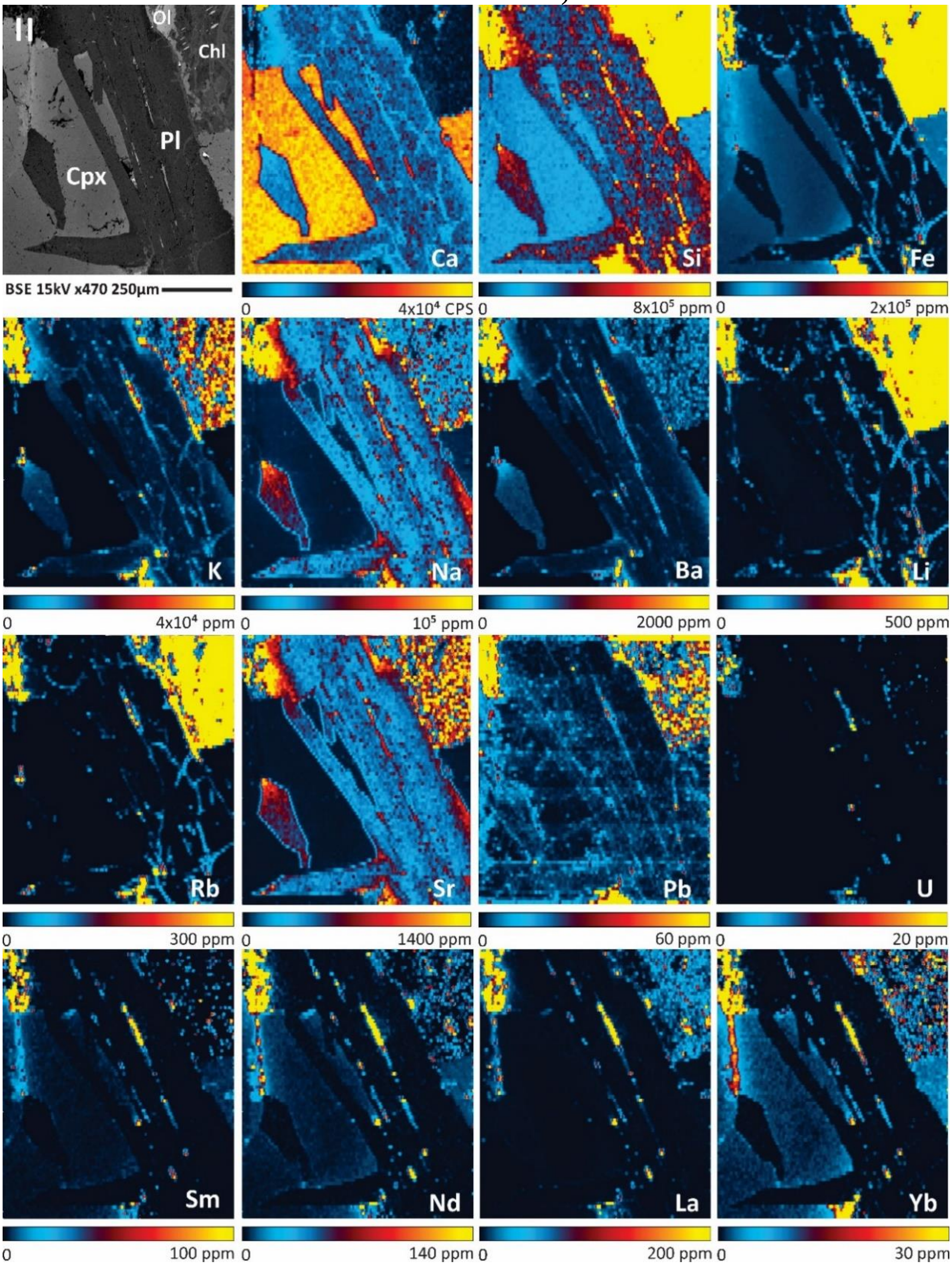

(Carvas et al., 2021)

Figure 2.5. Average element concentrations in alteration zones normalized by unaltered Ca-rich plagioclase average values. All data were extracted from selected regions in the LA-ICP-MS elemental maps through Monocle.

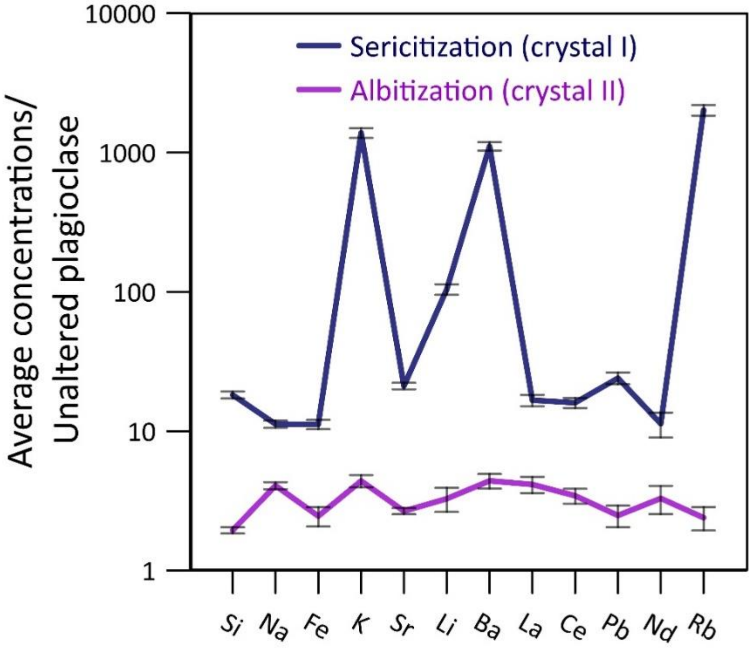

(Carvas et al., 2021)

2.4.3. Geochronological results

Four grains from sample LM-DA-BZ-5 were analyzed by the laser incremental-heating method: one whole-rock fragment (Lab #9237); one clear plagioclase crystal (Lab #9238); and two cloudy and sericitized plagioclase crystals (Lab #9239-01 and -02) (Fig. 2.6). All four samples yielded saddle-shaped spectra. The whole-rock chip (Lab #9237) yielded the most pronounced saddle-shape spectrum, with apparent ages at 168.0 ± 8.2 Ma (Fig. 2.6A) and unreasonably old apparent ages in the initial and final steps. The clear plagioclase crystal (Lab #9238) shows a saddle-shaped spectrum with a trough defining an apparent age estimate of 138.6 ± 2.5 Ma (Fig. 2.6B). These results can be interpreted as maximum ages of intrusion, but it is impossible to make further inferences. The two cloudy and sericitized plagioclase crystals yielded similar but not exactly reproducible saddle-shaped spectra that suggest variable amounts of excess argon in both grains (Fig. 2.6C). The trough defined by the intermediate temperature steps reached flat segments with distinct apparent age estimates of 131.9 ± 4.8 Ma and 124.1 ± 2.5 Ma that are also difficult to interpret.

Whole-rock fragments (Lab #7456-01 and -02 and #7457-01 and -02) and two plagioclase crystals (Lab #7459-01 and -02) from sample PPE-C also display saddle-shape spectra with no plateaus. Whole-rock chips from the center of the dyke (Lab #7457-01 and -02) yielded spectra with intermediate temperature apparent ages at 168.0 ± 12.0 and 167.6 ± 4.0 Ma (Fig. 2.6D); whole-rock chips from the dyke border (Lab #7456-01 and -02) yielded spectra with apparent ages at 137.8 ± 1.5 Ma and 137.2 ± 1.6 Ma (Fig. 2.6E). The only useful information retrievable from these results is that they identify maximum ages of intrusions, not particularly informative given the large scatter. Two sericitized plagioclase crystals from sample PPE-C (Lab #7457-01 and -02) yielded flat segments (no plateaus) that define apparent ages of 111.5 ± 1.2 Ma and 109.6 ± 5.5 Ma (Fig. 2.6F), showing that sericitization lowered the apparent ages and simultaneously masked the effects of excess argon components. The combination of excess argon (which increases the apparent age) with the presence of alteration phases (which lowers the apparent age) in a same grain or sample makes it impossible to retrieve much useful geochronological information from the results, other than the fact that the lowest apparent ages obtained record the maximum age of alteration.

Given the persistent presence of excess argon in whole-rock grains, we focused on dating selected mineral aliquots in samples LM-DA-203 and LM-DA-150. Since some of the pure mineral fractions were very fine grained, we dated the small crystals as silica-encapsulated aliquots both for ease of manipulation but also to measure and obviate any possible ^{39}Ar loss by recoil.

Sample LM-DA-203 yielded a reliable minimum estimate for the intrusion age, derived from the analysis of magmatic amphibole-biotite aggregates. Encapsulated grain aliquots from sample LM-DA-203 (Fig. 2.7) failed to show significant ^{39}Ar contents in the first (piercing) step, indicating that the small grains did not release ^{39}Ar by recoil or heating during irradiation. The initial incremental-heating analysis of amphibole-biotite aggregates (Lab #9169, Fig. 2.7A) yielded a two-step flat segment comprising > 80% of the total ^{39}Ar released with the age of 132.33 ± 0.69 Ma. A second aliquot (#9170), analyzed with a more appropriate heating protocol, yielded a well-defined plateau containing 90% of the total ^{39}Ar released with the age of 132.20 ± 1.20 Ma (Fig. 2.7A). Both results are compatible with the combined isochron age of 132.83 ± 0.30 Ma (Fig. 2.7B; initial ^{40}Ar/^{36}Ar of 294.2 ± 1.2, within error of the present atmospheric value of 298.56 ± 0.31 of Lee et al., 2006).

Figure 2.6. ^{40}Ar/^{39}Ar geochronology results (age spectra) of whole-rock (A), clear (B) and cloudy (sericitized) (C) plagioclase crystals from dyke LM-DA-BZ-5 (#9237, #9238, #9239–01 and _02), and of whole-rock (D and E) and cloudy (sericitized) (F) plagioclase crystal from dyke PPE-C (#7456–01 and _02, #7457–01 and _02 and 7459–01 and _02). None of the results above is a proper age, and they should not be interpreted as such (thus, the crosses over the diagrams).

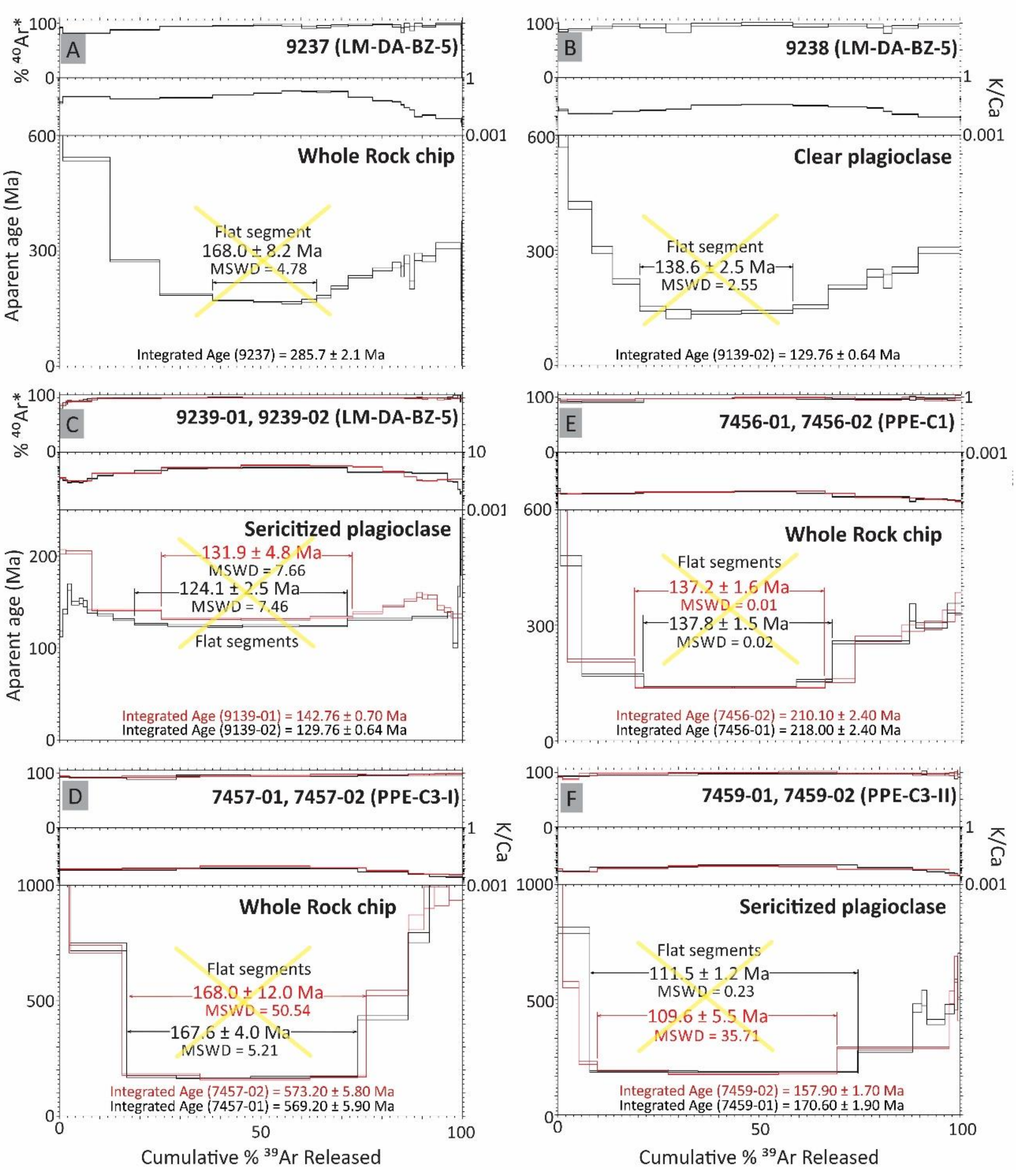

(Carvas et al., 2021)

Figure 2.7. ^{40}Ar/^{39}Ar geochronology results (age spectra, isochrons and probability density plots) of samples LM-DA-203 (A-I; #9169, #9170, #9156, #9159 and #9160) and LM-DA-150 (J-O; #9163 and #9166).

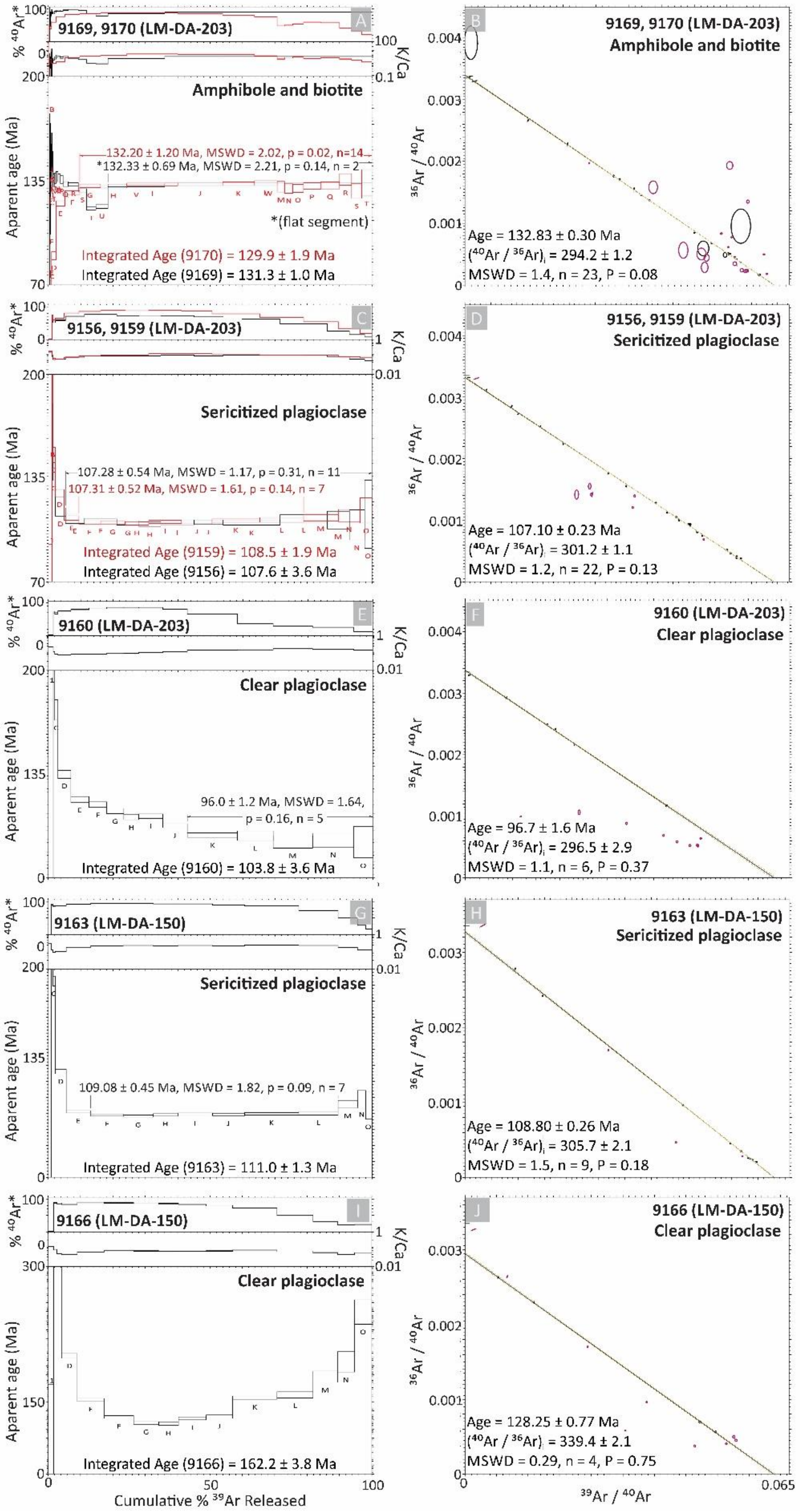

(Carvas et al., 2021)

Encapsulated grains of sericitized (cloudy) plagioclase from sample LM-DA-203 do not show evidence of ^{39}Ar release by recoil either. Incremental-heating analyses of two aliquots yielded reproducible spectra with old apparent ages in the initial steps that progressively descended towards well-defined plateaus containing more than 90% of the total ^{39}Ar released. The two encapsulated aliquots defined identical plateau ages of 107.28 ± 0.54 and 107.31 ± 0.52 Ma (Fig. 2.7C). An isochron for the entire data set yielded an age of 107.10 ± 0.23 Ma (Fig. 2.7D), within 2σ confidence level of the plateau ages, and showing an atmospheric initial ^{40}Ar/^{36}Ar value of 301.2 ± 1.1. These apparently coherent results are ~25 Ma younger than the plateau ages obtained for the magmatic amphibole-biotite clusters from the very same sample. Finally, sericite-free clear plagioclase crystals from sample LM-DA-203 yielded a spectrum with excess argon in low-temperature steps and a plateau at the high-temperature ones that comprised ~57% of the cumulative ^{39}Ar released and defined an age of 96.0 ± 1.20 Ma (Fig. 7E). The isochron fit by a positive elimination procedure to compensate for the excess Ar steps yielded a compatible age of 96.70 ± 1.60 Ma (Fig. 2.7F) and an initial ^{40}Ar/^{36}Ar value (296.5 ± 2.9) within 2σ from the present atmospheric value. The three apparently well-defined but totally distinct plateau ages obtained for the various minerals analyzed for mafic dyke LM-DA-203 clearly show the complexities associated with geochronology of partially altered mafic volcanic rocks, as discussed below.

Sample LM-DA-150 also shows complexity attributable to alteration. The sericitized plagioclase grains yielded a less pronounced saddle-shape spectrum with a well-defined plateau comprising more than 75% of total ^{39}Ar released and showing an age of 109.08 ± 0.45 Ma (Fig. 2.7G). The plateau age is compatible with the isochron age of 108.80 ± 0.26 Ma (Fig. 2.7H), showing that the plateau steps are not strongly affected by excess argon. In contrast, the sericite-free clear plagioclase grains from this sample display a pronounced saddle-shaped spectrum, showing significant excess argon (Fig. 2.7I) and minimum apparent ages at ~125 Ma.

All ^{40}Ar/^{39}Ar data are reported in supplementary material G. A combined probability density plot of the analyses exhibited in Fig. 2.7 is available in supplementary material L.

2.4.4. BULK ROCK GEOCHEMISTRY AND SR-ND ISOTOPE RATIOS

Bulk major and trace elements and Nd and Sr isotope results for each sample are reported in supplementary material H.

2.4.4.1. MAJOR, MINOR AND TRACE ELEMENTS

All samples are basaltic and tholeiitic in composition (supplementary material I). The SiO_2 and MgO contents of the 11 dykes analyzed range between 48.0–48.9 and 8.4–7.0 wt%, respectively, and TiO_2 contents range from 1.0 to 1.9 wt% (Fig. 2.8). Loss on ignition varies from 0.3 to 1.4 wt%, showing that the whole-rock compositions are not strongly affected by weathering or post-magmatic hydration or carbonation. The alteration identified in the crystals is subtle, thus the difficulties in recognizing alteration and its effects on geochronology. All samples correspond to suite A (SiO_2 < 52 wt%, MgO > 5.5 wt%, most samples with Al_2O_3 < 14 wt%) of the tholeiitic dykes from CFTD as defined by Bennio et al. (2003). Major and minor element variation plots (Fig. 2.8) exhibit a typical tholeiitic crystallization sequence dominated by clinopyroxene and plagioclase and minor titanomagnetite fractionation: decrease in CaO and Al_2O_3 and increase in SiO_2, TiO_2, K_2O, Fe_2O_{3t} and P_2O_5 with decreasing MgO contents. Na_2O concentrations are notably scattered and do not exhibit any trends. Major and minor elements and do not exhibit any trend with LOI (Fig. 2.8).

Trace element plots versus MgO (Fig. 2.9) show progressive enrichment in La, Nd, Th and U as the magma evolves. Sr, Pb, and Ba concentrations also increase, despite some scatter, while Rb does not exhibit any particular trend.

To further characterize anomalies in whole-rock data, we plotted minor and trace elements against three different proxies: La (which, in Fig. 2.9, follows a normal magmatic evolution pattern and does not seem to have been considerably disturbed by post-magmatic events); K (which is present in sericitized and albitized zones of plagioclase crystals); and LOI (a proxy for volatile input during hydrothermal alteration or weathering). All plots are shown in Fig. 2.10. Th, U and Na increase with La increase, whereas Sr does not follow any trend. Rb, also enriched in altered zones of the plagioclase crystals, increases as K increases. Sr and Pb do not show defined trends when plotted against LOI.

Figure 2.8. Major and minor elements (wt%, on dry basis) vs. MgO (wt%) and vs. LOI (wt%). Circles represent samples from this study. Samples LM-DA-203, LM-DA-150, LM-DA-BZ-5 and LM-DA-206 are highlighted (the first three were dated, and all of them have Sr and Nd isotope data). Empty diamonds consist of samples from Bennio et al. (2003), and stars are from Almeida et al. (2021), whenever available.

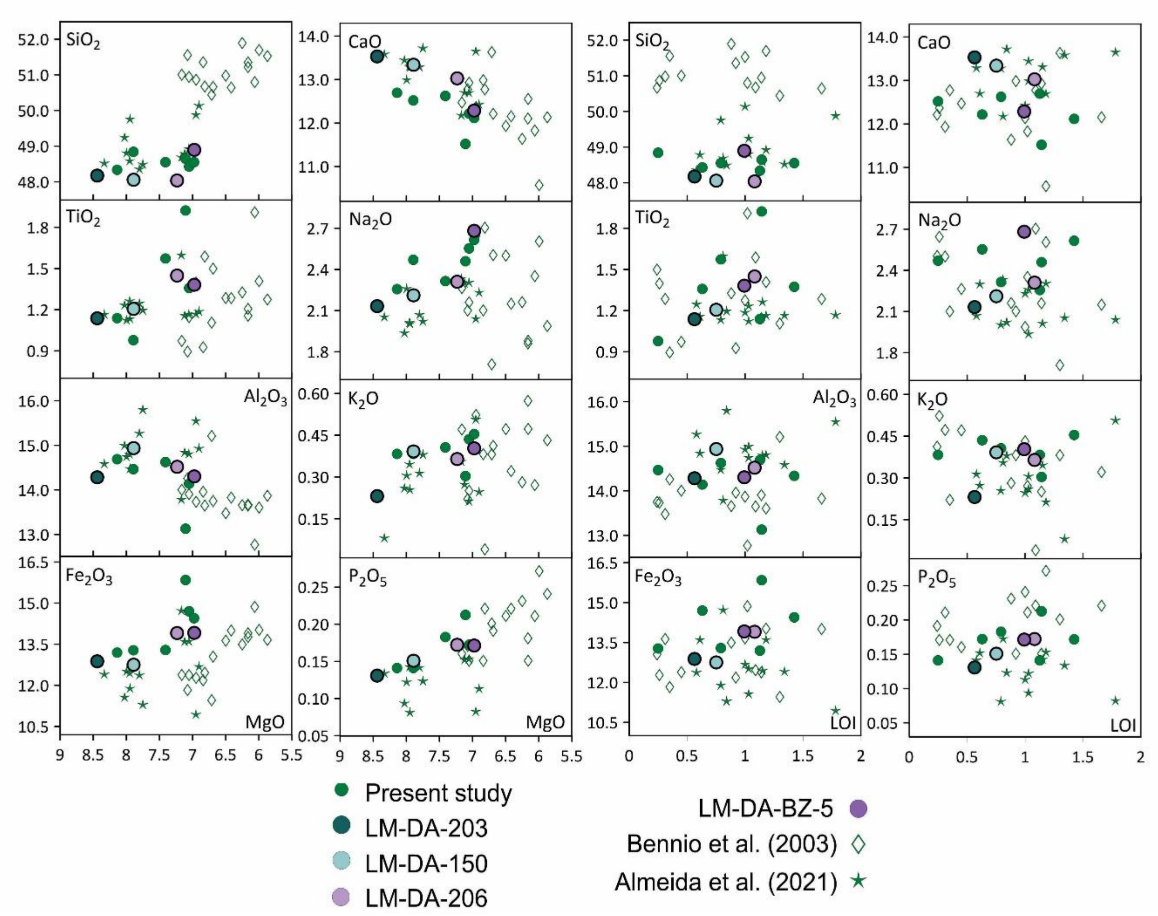

(Carvas et al., 2021)

Figure 2.9. Trace element (ppm) vs. MgO (wt%, on dry basis). Symbols as in Fig. 2.8.

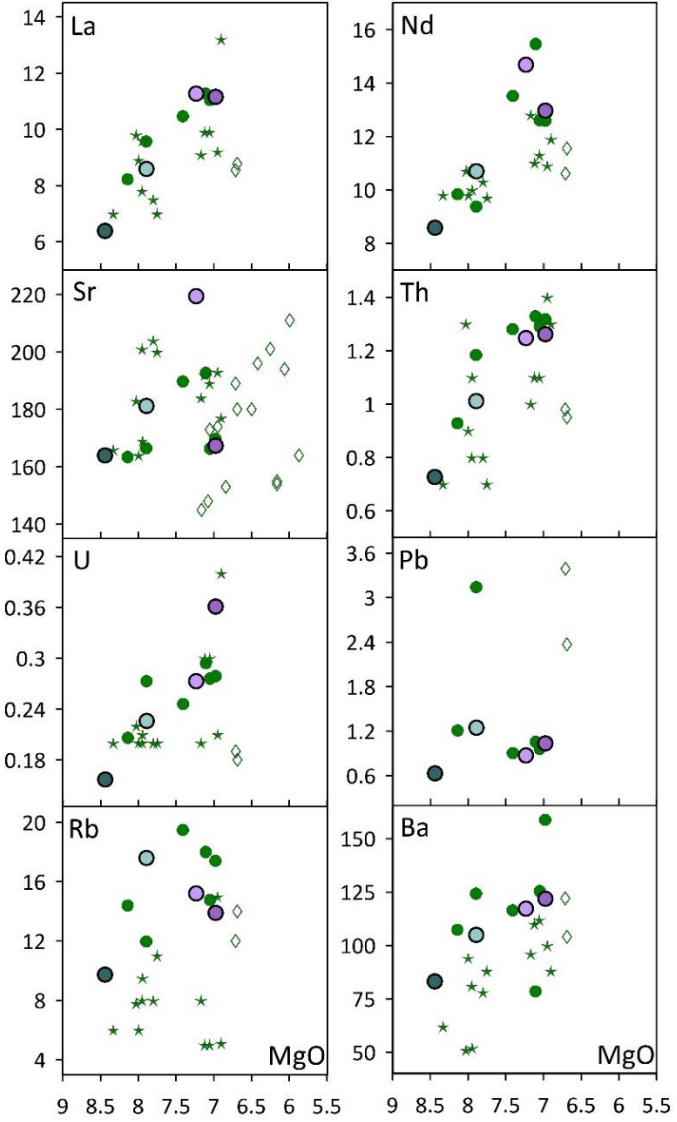

(Carvas et al., 2021)

Rare earth element (REE) patterns normalized to CI chondrite (McDonough and Sun, 1995) and multi-element patterns normalized to primitive mantle (McDonough and Sun, 1995) are shown in Fig. 2.11. The diagrams include CFTD data from Bennio et al. (2003) and Almeida et al. (2021), and Esmeralda and Ribeira basalts (Peate, 1997; Marques et al., 1999, and references therein), two subgroups of the Paraná-Etendeka Magmatic Province that display low TiO2 contents, similarly to the CFTD dykes.

Enrichment in light REE is observed for all samples ($2.1 \leq (La/Lu)_{CN} \leq 4.0$, mean = 2.7 ± 0.3; $1.4 \leq (La/Sm)_{CN} \leq 2.7$, mean = 1.8 ± 0.2). Additionally, most of the samples show slightly positive Eu anomalies ($0.92 \leq Eu/Eu^* \leq 1.11$, mean = 1.03 ± 0.04; Eu/Eu* is defined by

$Eu_{CN} / \sqrt{Sm_{CN} . Gd_{CN}}$). In the primitive mantle normalized multi-element diagram the dykes show erratic anomaly patterns (especially for Rb, Ba, K and Pb), similarly to those observed in Figs. 9 and 10, and consistent with mobility of these elements during alteration. In contrast, normalized Nb/Ta and Th/Nb values do not exhibit large variation ($0.84 \leq (Nb/Ta)_{PM} \leq 1.08$, mean 0.95 ± 0.04; $0.83 \leq (Th/Nb)_{PM} \leq 1.45$, mean 0.99 ± 0.06). All dykes have slightly negative Ti values.

Figure 2.10. Minor and trace element plots vs. La and K concentrations (ppm) and LOI (wt%). Symbols as in Fig. 2.8.

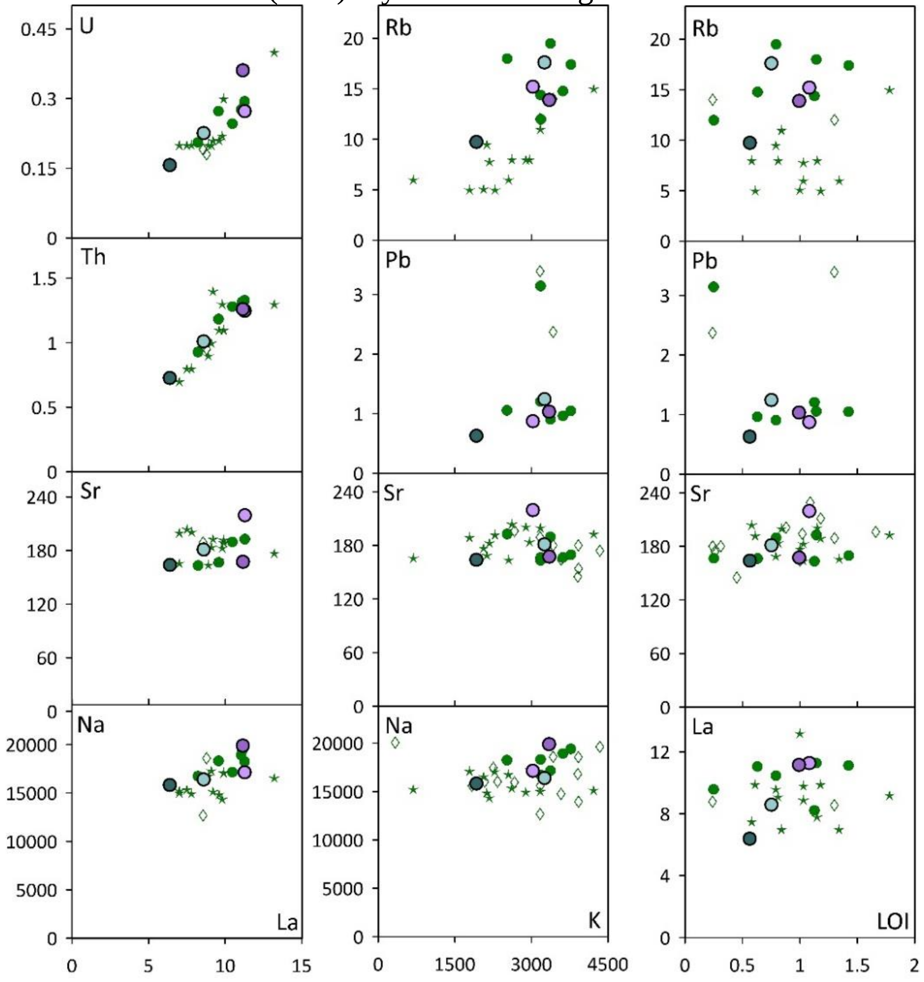

(Carvas et al., 2021)

Figure 2.11. A- CI-normalized (McDonough and Sun, 1995) REE patterns of group A (defined by Bennio et al., 2003). Samples LM-DA-203, LM-DA-150 and LM-DA-BZ-5 are highlighted. The results reported by Bennio et al. (2003) and by Almeida et al. (2021) are shown as dashed lines. LTi Esmeralda and Ribeira basalt samples from Parana´-Etendeka Magmatic Province are also illustrated (Peate, 1997; Marques et al., 1999; references therein). B - Primitive mantle normalized (McDonough and Sun, 1995) multi-element patterns of group A.

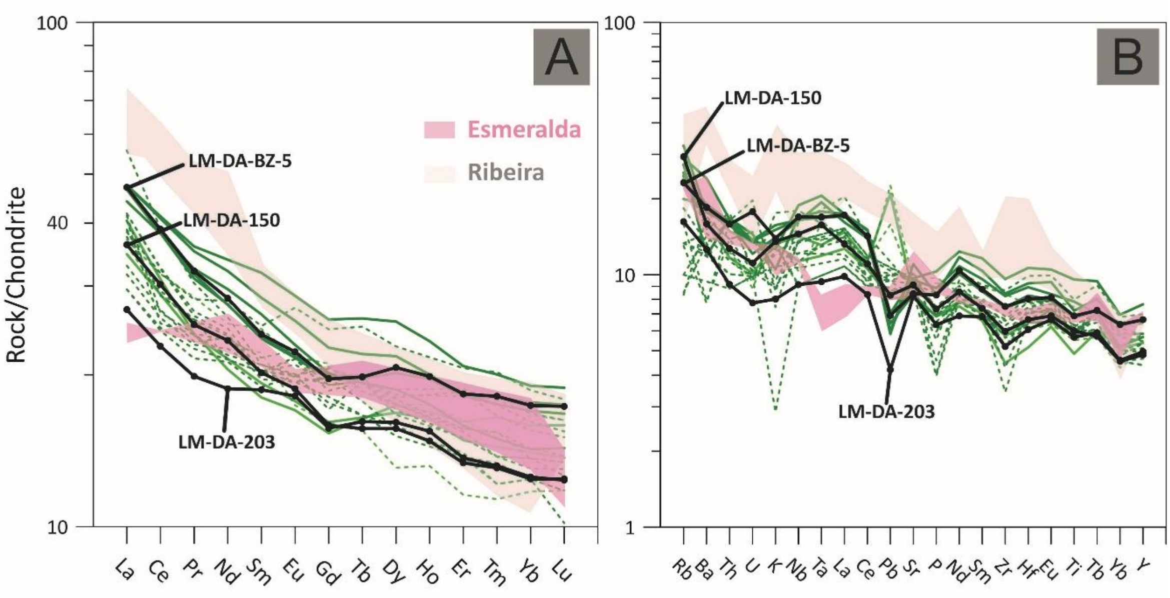

(Carvas et al., 2021)

2.4.4.2. SR AND ND ISOTOPE COMPOSITIONS

Initial Sr and Nd isotope ratios were calculated (supplementary material H) using the 132.32 ± 0.48 Ma ^{40}Ar/^{39}Ar age obtained for the amphibole-biotite aliquots, our best estimate for the age of dyke emplacement (Fig. 2.7C). The dykes have initial ^{87}Sr/^{86}Sr ratios varying from 0.70377 to 0.70429, and initial ^{143}Nd/^{144}Nd ranging between 0.51256 and 0.51264. Initial Sr and Nd isotope ratios are plotted along with previous results by Bennio et al. (2003) and LTi Esmeralda and Northern Paraná-Etendeka Magmatic Province basalts from South America (subgroup Ribeira is included; Fig. 2.12A and 13; Peate, 1997; Marques et al., 1999; Rocha-Ju´nior et al., 2013, 2020; and references therein). Initial ^{87}Sr/^{86}Sr vs MgO (Fig. 2.12B) is also shown. In ^{87}Sr/^{86}Sr and ^{143}Nd/^{144}Nd diagrams (Fig. 2.12A), the dykes plot in the same field of primitive group A defined by Bennio et al. (2003) and display lower ^{87}Sr/^{86}Sr and higher

$^{143}Nd/^{144}Nd$ than Esmeralda and Northern Paraná-Etendeka Magmatic Province basalts. $^{87}Sr/^{86}Sr$ values do not correlate with MgO contents (Fig. 2.12B).

Figure 2.12. A - Initial $^{87}Sr/^{86}Sr$ and $^{143}Nd/^{144}Nd$ compositions of mafic CFTD dykes, along with LTi and Northern basalt flows from the South American Paraná-Etendeka Magmatic Province (Peate, 1997; Marques et al., 1999; Rocha-Júnior et al., 2013, 2020; Machado et al., 2015; and references therein). CC – Regional continental crust (average $(^{87}Sr/^{86}Sr)_{133}$Ma = 0.7125; $(^{143}Nd/^{144}Nd)_{133}$Ma = 0.5121; MgO = 1.95 wt%; Peixoto et al., 2017). B – Initial $^{87}Sr/^{86}Sr$ vs. MgO (wt%) distribution shows little variation with MgO decrease.

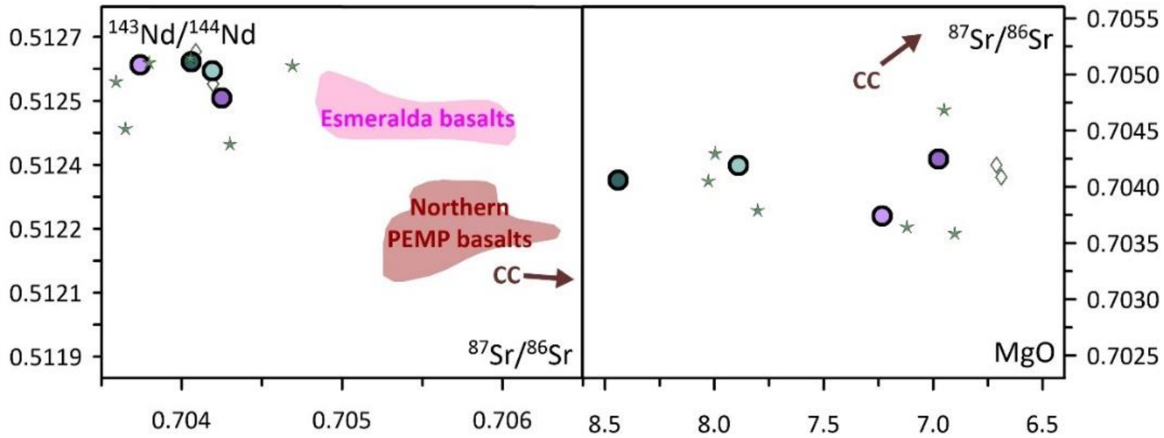

(Carvas et al., 2021)

2.5. DISCUSSION

2.5.1. INTERPRETING COMPLEX $^{40}Ar/^{39}Ar$ GEOCHRONOLOGICAL RESULTS

The wide range and complexity of geochronological results obtained for both whole rock fragments and plagioclase crystals (between apparent ages of ~168 Ma for saddle-shaped spectra and true plateau age of 96.0 ± 1.20 Ma for an albitized plagioclase crystal) illustrate the challenges associated with dating mafic dyke swarms from southeastern Brazil. Rigorous interpretation is essential for differentiating intrusion ages from geochronological artefacts (e.g., excess argon) or post-intrusion alteration.

2.5.1.1. SADDLE-SHAPED INCREMENTAL HEATING SPECTRA

Every whole-rock fragment analyzed in this study (samples LM-DA-BZ-5, PPE-C1, PPE-C3-I) yielded saddle-shaped spectra that reveal the presence of significant excess argon components (Fig. 2.6). Even though the saddle-shaped spectra reach flat segments at the middle temperature steps, none of these segments provides reliable geochronological information because of the large amounts of excess argon.

Saddle-shaped spectra are not confined to whole-rock fragments. Pristine (sample LM-DA-BZ-5, Fig. 2.6B; sample LM-DA-150, Fig. 2.7I) and sericitized plagioclase crystals (sample LM-DA-150, Fig. 2.7G; sample LM-DA-BZ-5, Fig. 2.6C; and sample PPE-C3-II, Fig. 2.6F) also yielded saddle-shaped spectra, showing that excess argon is pervasive throughout the dykes and cannot be necessarily obviated by dating plagioclase phenocrysts. The excess argon component is more pronounced in the center than the margins of the dykes.

The large amounts of excess argon (high apparent ages in low and high temperature steps) in whole-rock fragments and plagioclase crystals suggest that dyke emplacement occurred at depth, without major exchanges with crustal fluids or the atmosphere (McDougall and Harrison, 1999). The abundance of excess argon in the dykes makes it difficult to use the $^{40}Ar/^{39}Ar$ incremental-heating results at face-value. Importantly, the fact that many of the published $^{40}Ar/^{39}Ar$ results for southeastern Brazil mafic dykes reveal similar saddle-shaped spectra (e.g., Bennio et al. 2003; Guedes et al., 2005, 2016; Almeida et al., 2021) suggests that the true age of magma emplacement in these systems may yet to be determined.

2.5.1.2. AGE OF MAGMATISM

Among the four mafic dykes investigated in this study (samples LM-DA-BZ-5, LM-DA--50, LM-DA-203, PPEC), only magmatic amphibole-biotite grains from sample LM-DA-203 (Fig. 2.7A, B) provide reliable information about the age of magmatism. The well-defined plateau of aliquot #9170, compatible with the large flat segment of aliquot #9169, the absence of ^{39}Ar recoil losses from the small crystals, the reproducibility of results for the two aliquots, the absence of excess argon (Fig. 2.7B), combined with the high closure temperatures for amphibole suggest that 132.83 ± 0.30 Ma (isochron age) is a reliable age of crystallization of the amphibole-biotite clusters. The minerals result from late-stage magmatic alteration of pyroxene, implying that 132.83 ± 0.30 Ma is the minimum age of magmatic intrusion. All other attempts at geochronology yielded results affected by excess argon or alteration.

2.5.1.3. ^{40}AR/^{39}AR RESULTS FOR SERICITIZED PLAGIOCLASE CRYSTALS

Cloudy plagioclase crystals from the CFTD mafic dykes invariably reveal young ages, but most of these cloudy plagioclase crystals also show some excess argon. Fortunately, some samples (e.g., sample LM-DA-203, Fig. 2.7C; sample LM-DA-150, Fig. 2.7G) show that sericitization may be so pervasive that it overwhelms the excess argon component in the sericitized plagioclase crystals, suggesting that incremental-heating ages may indeed record the timing of pervasive K-alteration of the mafic dykes.

Cloudy plagioclase crystals from dyke LM-DA-203 yield reproducible plateau ages of 107.28 ± 0.54 and 107.31 ± 0.52 Ma (Fig. 2.7C), which most likely record the maximum age of sericitization. Cloudy plagioclase crystals from dyke LM-DA-150, located ~20 km away from LM-DA-203, record a maximum age of sericitization of 109.08 ± 0.45 Ma (Fig. 2.7G). Finally, two sericitized plagioclase crystals from dyke PPE-C3-II, located ~5 km away from LM-DA-203 (Fig. 2.1), failed to produce age plateaus but yielded two flat segments, containing more than 50% of the total ^{39}Ar released, that suggest apparent age estimates of 111.5 ± 1.2 and 109.6 ± 5.5 Ma. Ages obtained from sericitized plagioclase crystals record noble gas contributions from two distinct reservoirs: sericite crystals and unaltered plagioclase remnants. Therefore, apparent differences in sericitization ages among dykes LM-DA-203, LM-DA-150, and PPE-C3-II may simply reflect differences in the percentages of the original plagioclase crystals that survived alteration. The similar ages for sericitized plagioclases from three dykes up to 25 km apart suggest that the K-rich fluid that altered Ca-rich plagioclase phenocrysts to sericite travelled through extensive parts of the crust.

The reproducible and flat spectra for the two sericitized plagioclase aliquots from dyke LM-DA-203, and the apparent absence of an excess argon component, suggest that the isochron age of 107.10 ± 0.23 (Fig. 2.7D) Ma is a reliable age for the K-alteration event that affected the mafic dykes in the CFTD. However, a more robust estimate of the sericitization age was obtained by a mixture model (Fig. 2.13A, outlined in supplementary material J), analogous to the one proposed by Verati and Jourdan (2014). The model estimates the amount of radiogenic ^{40}Ar generated from a pure igneous ~132 Ma plagioclase (K by EPMA = 0.008 mol) mixed with sericite (K by EPMA = 0.602 mol) of several possible ages. Given that petrographic observations and LA-ICP-MS elemental analyses reveal ~15–25% sericitization, the age of 107.10 ± 0.23 Ma is a maximum age for the alteration and probably reflects a mixture of ~80% 132 Ma plagioclase with ~20% of a sericite generation ~106–105 Ma (Fig. 2.13A). The mixture model can also predict the K/Ca ratios obtained for the sericitized plagioclase during step-heating analysis, which range between 0.1 and 1 (Fig. 2.14).

2.5.1.4. ^{40}AR/^{39}AR RESULTS FOR ALBITIZED PLAGIOCLASE CRYSTALS

The low K-contents of magmatic plagioclase measured for the Cabo Frio dykes also make them very susceptible to age resetting by the introduction of Na and minor K during albitization. A visually ‘‘fresh” plagioclase crystal from the same LM-DA-203 sample yielded a plateau age of 96.0 ± 1.20 Ma (Fig. 2.7E). The age spectrum has a prominent slope, suggesting that the results may be affected by excess Ar. However, the plateau steps have no resolvable slope (Sharp and Renne, 2005; Schaen et al., 2020), and the excess Ar and plateau trends are distinguishable in the isochron (Fig. 2.7F), which allows us to estimate a maximum age of alteration.

LA-ICP-MS elemental maps show that the sample was albitized. Electron microprobe analyses show that hydrothermal albite contains ~0.025 mol K, as compared to 0.007 mol K in the original plagioclase phenocrysts, revealing that K was introduced together with Na during albitization. Fig. 2.13B illustrates the effect of various proportions of albitization, at different times (90, 80, 70, 60, 50, 40 and 30 Ma), on the apparent age measured for the plagioclase phenocryst. Based on SEM observations, LA-ICP-MS elemental maps, and electron microprobe analysis, visual estimation of the plagioclase phenocrysts albitization varies between ~10–30 wt%. Therefore, albitization must have occurred sometime between 60 and 30 Ma. Once again, the mixing model is coherent with the K/Ca ratios measured during step-heating analysis, which range between 0.01 and 0.1 (Fig. 2.14).

Figure 2.13. Modeled ages (black lines) for sample LM-DA-203 of mixtures between pristine bytownitic plagioclase and an alteration phase, either sericite (A) and albite (B), of various ages. The intercepts between modeled ages and measured plateau ages indicate the needed proportion of an alteration phase of a given composition and age. Approximately 10–20 wt% of 106–105 Ma sericite mixed with bytownitic plagioclase would produce the observed plateau age. Similarly, approximately 10–20 wt% of 40 to 70 Ma albite would suffice to produce the measured ~96 Ma plateau age.

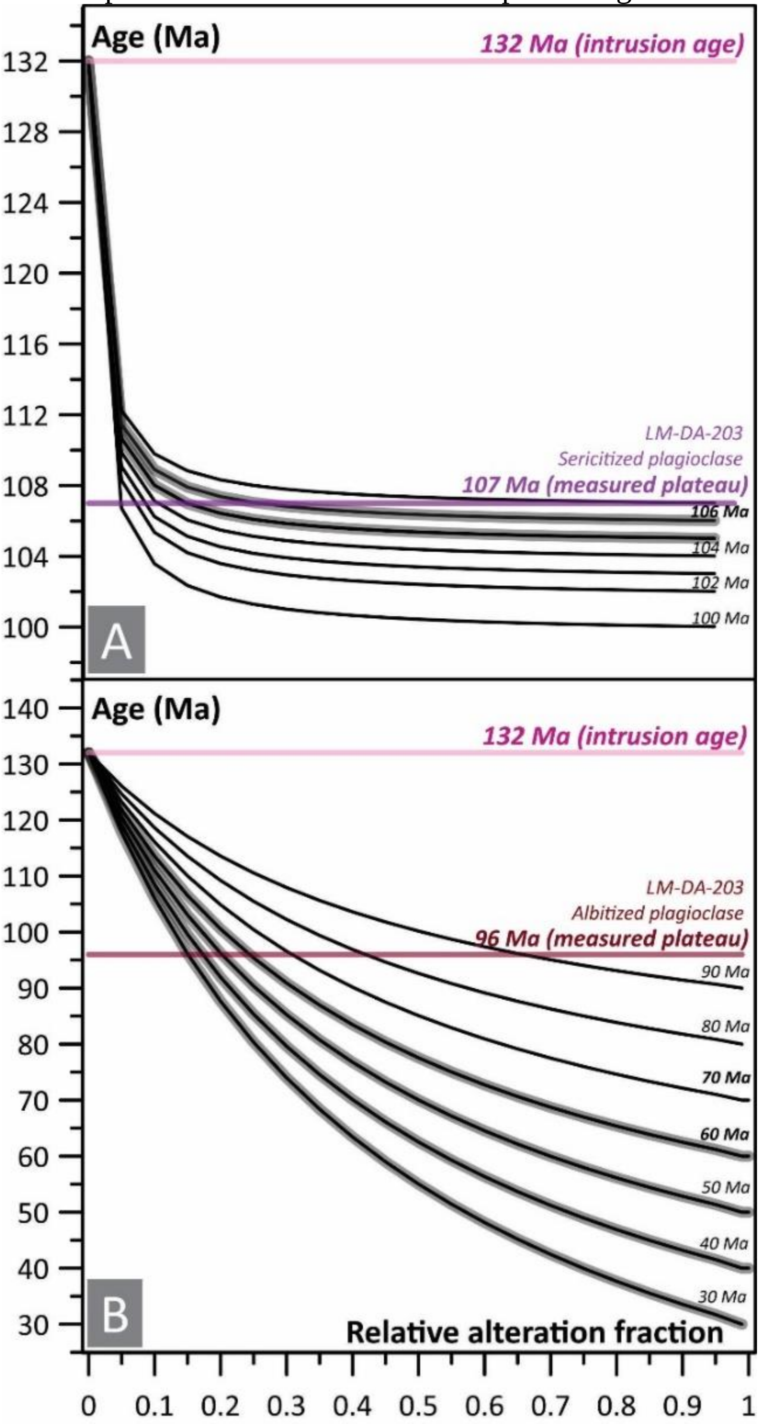

(Carvas et al., 2021)

Figure 2.14. K/Ca and Ca/K ratios for different mole fractions of K-poor and K-rich plagioclase and sericitization/albitization (all calculations are available in supplementary material J).

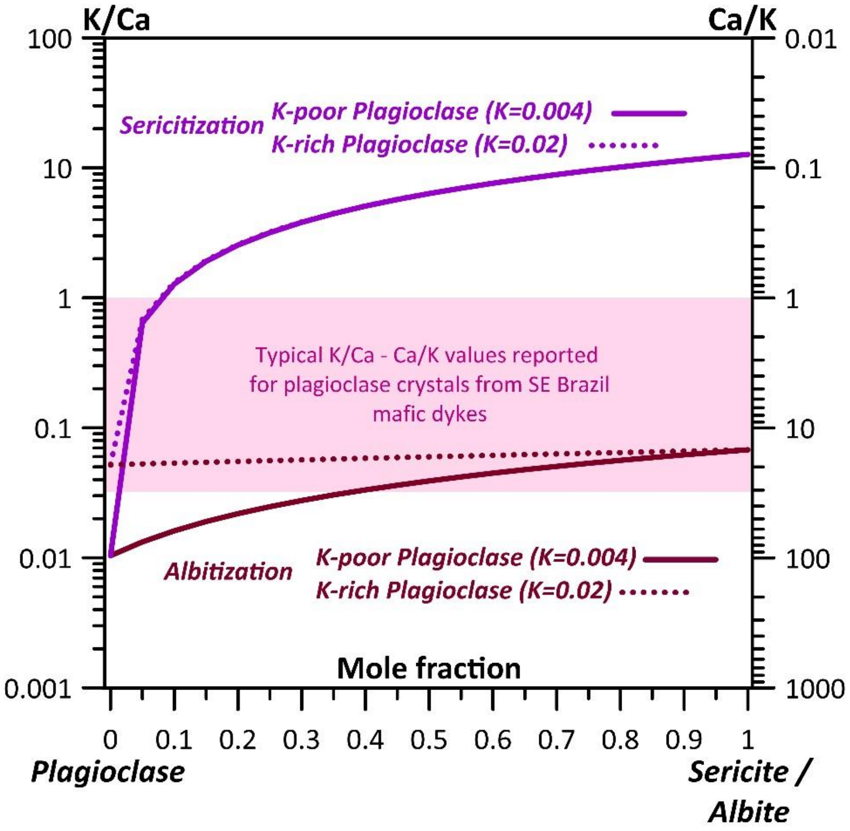

(Carvas et al., 2021)

The 60–30 Ma period corresponds to the emplacement of late-stage alkaline magmatism along the Cabo Frio Lineament, which connects Poc¸os de Caldas and Cabo Frio by a series of intrusions (Fig. 2.1; Ferroni et al., 2017, and references therein). The age similarity suggests possible links between thermal anomalies induced by the alkaline magmatism and circulation of hydrothermal solutions along coastal dykes and fracture zones. Albitization of plagioclase crystals can also explain the difficulties in obtaining reproducible ^{40}Ar/^{39}Ar ages from various aliquots from a same sample from the Cabo Frio Tectonic Domain dykes, as illustrated in Almeida et al. (2021). Age differences among visually pristine crystals from a same intrusion probably result from variable proportions of hydrothermal albite, which is not readily identifiable by optical microscopy.

2.5.2. EFFECTS OF HYDROTHERMAL ACTIVITY ON GEOCHEMICAL AND ISOTOPIC COMPOSITIONS: IMPLICATIONS TO FLUID SOURCES AND TECTONIC EVOLUTION

^{40}Ar/^{39}Ar geochronology shows that both sericitization (~106–105 Ma; Fig. 2.13A) and albitization (60–30 Ma; Fig. 2.13B) disturbed the K-Ar system in some of the plagioclase crystals from the CFTD dykes. The LA-ICP-MS and whole-rock geochemistry results provide further evidence for alteration: many of the elements (e.g., K, Na, Pb, Sr, Rb, Ba) present in sericitized and albitized areas of plagioclase crystals are scattered when plotted against MgO contents for whole-rock data. These elements increase with increasing K contents (Fig. 2.10). Combining all geochemical proxies permits evaluating possible sources of alteration fluids.

Firstly, the elements enriched in the altered samples (e.g., K, Na, Rb, Sr, Li, Ba) are readily soluble in and removed by weathering solutions, confirming that weathering is not the process responsible for affecting the K-Ar system. The absence of major and trace element correlations with LOI values (Figs. 8, 10) is further evidence that weathering processes, which typically result in high LOI values, have not significantly affected the dyke samples.

Similarly, seawater input was not significant because the LREE enrichment and HREE depletion in the sericitized and albitized zones of plagioclase crystals is the opposite of what would be expected if seawater was involved (e.g., Elderfield, 1988; Zheng et al., 2016; Deng et al., 2017). In addition, ^{87}Sr/^{86}Sr values for the least radiogenic sample of the set vs 1/Sr concentrations do not follow a mixing trend with Albian seawater (Veizer, 1989; Fig. 2.15).

The absence of Sr and Nd trends towards local crustal compositions (Fig. 2.12; data from Peixoto et al., 2017) suggests that crustal fluids were not significant in the alteration of the dykes.

Late-stage magmatic liquids, which affected some of the primary clinopyroxene and olivine crystals and generated amphibole, biotite and chlorite, could have supplied the incompatible elements to the altering feldspars. However, the sericitization and albitization ages suggest that fluid percolation took place long after the deuteric processes which resulted in the 132.83 ± 0.30 Ma magmatic amphiboles-biotites clusters (Fig. 2.7B), also precluding the involvement of magmatic fluids in the alteration processes.

Furthermore, the ^{40}Ar/^{39}Ar results suggest that sericitization and albitization occurred at different times and involved distinct solution compositions. Sericitization solutions (Fig. 2.3, 2.5) were enriched in K, Na, Si, Rb, Ba, Pb, Sr, Li and some LREE (La, Ce, minor Nd). In contrast, albitization solutions (Figs. 2.4, 2.5) were not rich in Si, Pb and REE and were less enriched in K, Fe, Sr, Li, Ba and Rb than sericitization solutions. This change in composition of the percolating fluids may reflect distinct source compositions or PT conditions (Warren, 2016).

Alteration ages indicate that fluid percolation was coeval with alkaline magmatism along the southeastern margin of Brazil, which started at 134 Ma and occurred, episodically, until about 60–50 Ma (Montes-Lauar et al., 1995; Gomes et al., 2018; Ferroni et al., 2017; and references therein; Gomes and Vasconcelos, 2021). These magmas intruded both continental onshore basement and adjacent offshore sedimentary basins, suggesting that some of the geochemical characteristics of the alteration fluids may have been derived from water-rock interactions in these offshore basins.

The South Atlantic marginal basins are notorious for extensive and thick evaporite layers formed during the late Aptian (Milani and Filho, 2000). Seismic reflection (Magee et al., 2021) show that Late Cretaceous and Paleogene magmatism intruded and interacted with the Aptian salt layers, causing hydrothermal circulation and Albian-Santonian salt movement. If these layers were to be partially dissolved during alkaline magmatism, hot solutions rich in K and Na would be produced and could have migrated into the extending tectonic margin, interacting with alkaline pulses, basement rocks and seawater, particularly when lithospheric uplift and extension were enhanced after the Aptian-Albian transition (Cogné et al., 2012; Granot and Dyment, 2015). The increase and scatter of $^{87}Sr/^{86}Sr$ data of the tholeiitic dykes can be explained by mixing curves involving evaporitic compositions of the Campos Basin (in the immediate offshore of Cabo Frio Tectonic Domain; Farias et al., 2019; Lima et al., 2020) and variable smaller contributions of regional continental crust (Peixoto et al., 2017), regional alkaline dykes (Thompson et al., 1998) and perhaps a minor Albian seawater component (Fig. 2.15).

A schematic illustration of how hydrothermal cells may have driven sericitization and albitization along the margin is depicted in Fig. 2.16. If proven correct, these hydrothermal cells may have affected the rheological properties and geochemical characteristics of the rifting margin. Furthermore, if the hydrothermal alteration processes identified in the Cabo Frio Tectonic Domain occurred along the entire South Atlantic coast, young mafic dykes elsewhere in southeastern Brazil (e.g., Renne et al., 1996; Deckart et al., 1998; Raposo et al., 1998; Guedes et al., 2016; Almeida et al., 2021) may also have partial resetting of the K-Ar system. Systematic elemental mapping of plagioclase crystals used in geochronology would permit testing this hypothesis.

Figure 2.15. Initial $^{87}Sr/^{86}Sr$ versus 1/Sr concentrations for the Cabo Frio Tectonic Domain (CFDT) dykes. Mixing curves between the least radiogenic sample of the set and Albian seawater (Veizer, 1989), CFTD alkaline dykes (Thompson et al., 1998), Campos Basin evaporites (Farias et al., 2019; Lima et al., 2020) and regional continental crust (Peixoto et al., 2017) are indicated. All isotopic data was corrected to 100 Ma. Symbols as in Fig. 2.12.

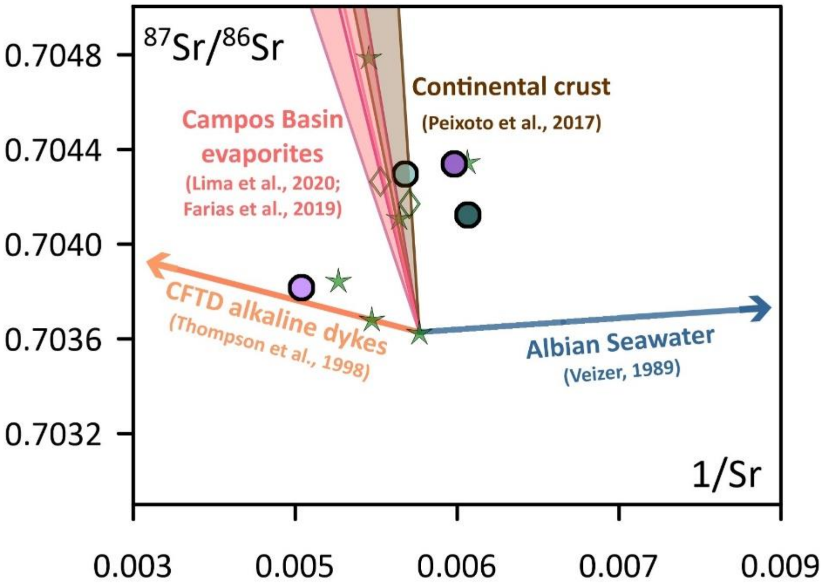

(Carvas et al., 2021)

Figure 2.16. Hydrothermal fluid percolation affecting the Cabo Frio Tectonic Domain at ~106–105 Ma. Similar processes occurred again between 60–30 Ma. Fluids generated in evaporite-rich marginal basin (Campos Basin) percolated the crust through extensional faults, partially altering the intrusive rocks emplaced along the same faults during Gondwana breakup and South Atlantic opening.

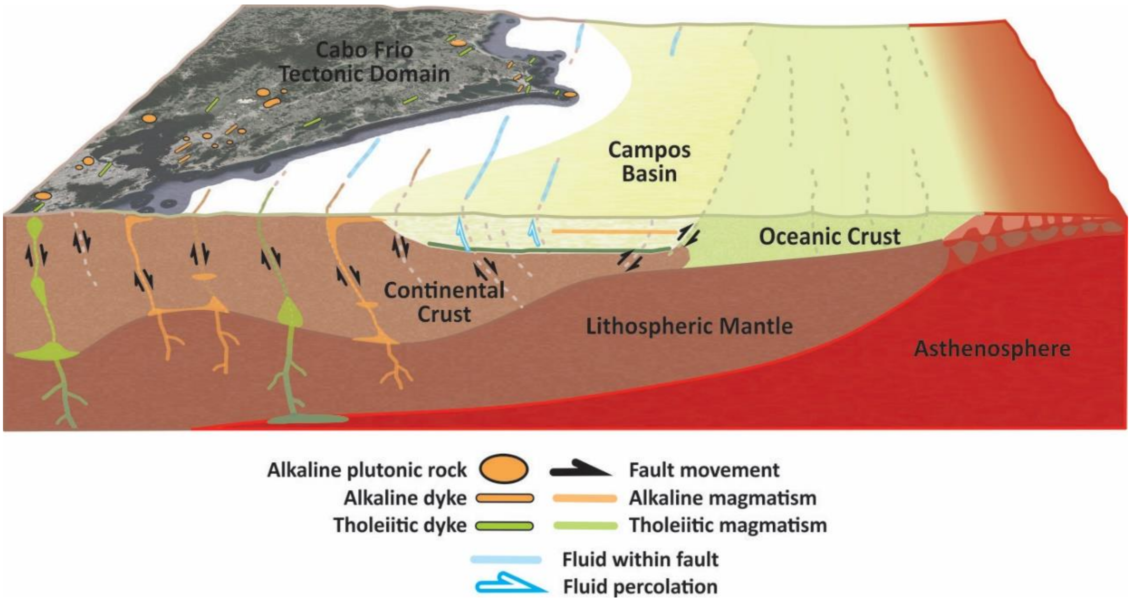

(Carvas et al., 2021)

2.6. CONCLUSIONS

^{40}Ar/^{39}Ar analyses of encapsulated amphibole and biotite crystals from primitive mafic dykes from the Região dos Lagos, Cabo Frio Tectonic Domain, southeastern Brazil, yielded a minimum intrusion age of 132.83 ± 0.30 Ma (1σ), which corresponds to early stages of Gondwana breakup and South Atlantic expansion. LA-ICP-MS elemental maps of altered plagioclase crystals from the same samples unveil the passage of fluids enriched in K, Na, Rb, Ba, Sr, Si, Li, Fe, Pb and light REE that affected the K-Ar system. Analyses of encapsulated sericitized plagioclase crystals suggest alteration by K-rich fluids at ~106–105 Ma; albitized plagioclase crystals suggest migration of Na-rich fluids in the 60–30 Ma interval.

Trace element and isotopic data suggest that the tholeiitic mafic magmas were not significantly contaminated by the continental crust or seawater. Instead, alkaline magmatic intrusions into evaporite layers in the marginal basins likely mobilized Na- and K- rich fluids and introduced them into the expanding crust. These hydrothermal processes led to albitization and sericitization that affected the K-Ar system in the Cabo Frio Tectonic Domain mafic dykes. Similar processes may have also partially reset the K-Ar system in a number of other dyke swarms in southeastern Brazil and Africa.

ACKNOWLEDGEMENTS

This research was supported by Fundação de Amparo à Pesquisa do Estado de São Paulo (FAPESP; Procs. 2012/06082-6, 2014/22948-9, 2017/18232-6, 2018/23650-4), Petrobras, Coordenação de Aperfeiçoamento de Pessoal de Nível Superior (CAPES; Proc. 1425945), and Conselho Nacional de Desenvolvimento Científico e Tecnológico (CNPq; Proc. 141058/2018-8). The Argon Laboratory at UQ-AGES was partially funded by ARC Large grant A39531815 to PV, and the ^{40}Ar/^{39}Ar, microscopy and EPMA, and LA-ICP-MS analysis were funded by UQ-AGES. We thank Marcia Ernesto, Fábio Braz Machado and Caio Morelli Vicentini for all the assistance and orientation during sampling. We are also very thankful to Liliane Aparecida Petronilho, David Thiede, Allan Gomes, Alice Mcdonald and Al-Tamini Tapu for suggestions and support during analyses. The authors acknowledge the facilities and the scientific and technical assistance of the Microscopy Australia Facility at the Centre for Microscopy and Microanalysis (CMM), The University of Queensland. LS Marques and M Babinski are CNPq Fellow Researchers. Fred Jourdan, Renaud Merle, Arto Luttinen, Courtney Sprain and Brian Jicha are acknowledged for insightful suggestions on the manuscript.

CHAPTER 3 – TRACKING THE TRANSITION FROM A GONDWANA LIP TO THE SOUTH ATLANTIC OCEAN WITH GEOCHRONOLOGICAL AND GEOCHEMICAL INDICATORS (SUBMITTED TO *JOURNAL OF GEOPHYSICAL RESEARCH – SOLID EARTH*)

K. Z. Carvas[1], L. S. Marques[1], P. M. Vasconcelos[2], and T. Ubide[2]
[1]Instituto de Astronomia, Geofísica e Ciências Atmosféricas, Universidade de São Paulo, São Paulo, SP 05508-090, Brazil
[2]School of Earth and Environmental Sciences, The University of Queensland, Brisbane, QLD 4072, Australia

ABSTRACT

Evidence of early oceanization during transition from large igneous provinces (LIPs) to new ocean crust is mostly missing in the geological record. Mafic dykes geochemically akin to mid-ocean ridge basalts (MORBs) occur in late stages of LIPs, but their tectonic role during margin evolution remains poorly constrained. Here we use whole-rock and high-resolution clinopyroxene chemistry of two distinct types of mafic dykes from the southeastern Brazilian margin to show that a MORB-like plumbing system became magmatically active in the central South Atlantic ~2 Ma after the volcanic peak of Paraná-Etendeka Magmatic Province. The LIP basaltic dykes derived from a metasomatized lithospheric mantle comprising 100-96% depleted mantle (DMM), 0-4% pyroxenite, and 1-3% Archean subcontinental lithospheric mantle (SCLM). Absence of elemental oscillatory zoning in clinopyroxene crystals suggests that they were produced by a single magma pulse, consistent with the strong magma fluxes in LIPs. MORB-like dykes, which exhibit strong similarities with South Atlantic MORBs, are interpreted to represent early stages of oceanization deriving from asthenospheric melts from a 100-98% DMM with 0-2% pyroxenite source, with small (0.2-0.4%) ancient SCLM contributions. The MORB-like intrusions ascended and cooled rapidly along faults and were fed by numerous magma injections that suggest episodic decompression of the asthenospheric source ~20 Ma before the birth of central South Atlantic. Such combination of subduction-influenced and MORB-like dykes is recurrent in ancients and modern rifts globally, suggesting

that thinned lithospheric blocks affected by ancient subductions may become more susceptible to early oceanization in crustal margins.

3.1. INTRODUCTION

The timing and mechanisms controlling the transition from large igneous provinces (LIPs) into oceanic crust during supercontinent breakup are poorly constrained. In the case of Pangea rifting and opening of the South Atlantic, the oldest seafloor magnetic anomalies usually postdate flood basalt extrusion by ~20-30 Ma; however, geochronological evidence shows that minor MORB-like intrusions were almost coeval with late-stage flood basalt volcanism (e.g., Jagoutz et al., 2007; Jourdan et al., 2007). Little is known about the role and significance of this early MORB-like intrusive magmatism during rifting, and whether it marks a stepwise transition from a LIP into a passive margin or whether it simply represents isolated asthenospheric upwellings still controlled by the LIP system.

Early asthenospheric upwelling and MORB intrusive events are observed in modern rifts, such as the Red Sea (Ligi et al., 2012; and references therein), where gabbros with MORB-like compositions and coeval with flood basalt magmas occur where continental crust is transitioning into oceanic crust (e.g., Corti et al., 2003; Ligi et al., 2018; Ligi et al., 2019). The MORB-like intrusive rocks are associated with crustal thinning and their intrusion potentially modifies the rheological behavior of the lower crust, causing mechanical decoupling between the crust and the lithospheric mantle (Ligi et al., 2018; Niu, 2021; and references therein). This suggests that oceanization starts at depth, weakens the lower crust, progressively reaches shallower levels, and slowly evolves into a passive continental margin (Gallacher et al., 2019).

The opening of the South Atlantic Ocean resulted from southern Gondwana rifting and occurred after the Paraná-Etendeka LIP magmatism (Torsvik et al., 2009, and references therein). Therefore, it provides an excellent target where to investigate LIP-ocean transition in ancient rifts, where oceanization is complete. While flood basalt volcanism lasted for 1.6-3.0 Ma and peaked at 134.5 ± 0.1 Ma in the central segment of the rift (Gomes & Vasconcelos, 2021), the magnetic records suggest that seafloor spreading started between 132-126 Ma, in meridional Gondwana, reaching the regions above the Florianopolis Fracture Zone at ~112 Ma (Fig. 3.1A; Torsvik et al., 2009, and references therein). If oceanization in the South Atlantic progressed similarly to what occurs today in the Red Sea, missing fragments of the early formed ocean floor must exist in offshore coastal segments of South America and Africa.

To find whether oceanization indeed occurred early in the transition from the Paraná-Etendeka LIP into a South Atlantic mid-ocean ridge, it is essential to (i) measure accurately and precisely the intrusive age of MORB-like dykes, (ii) identify asthenospheric mantle sources associated to such occurrences, and (iii) unravel magma dynamics during rifting. These objectives are achievable through a combination of high-resolution geochronology, elemental and isotope geochemistry, and detailed mineral chemistry (e.g., Ubide et al., 2019a) on onshore MORB-like dykes, where intrusive relationships can be directly observed.

MORB-like dykes occur within the Cabo Frio Tectonic Domain, a thinned lithospheric block in the southeastern Brazilian margin (Figs. 1A, 1B; e.g., Bennio et al., 2003; Schmitt et al., 2016; Almeida et al., 2021; Carvas et al., 2021). These dykes and their emplacement mechanisms offer an ideal setting where to investigate the role of early MORB magmatism in the transition towards oceanization in ancient rift systems. The dykes constitute the northern portion of the Serra do Mar Dyke Swarm, a large NE-SW set of intrusions extending from São Paulo to Rio de Janeiro (Fig. 3.1A) (Almeida, 1986; Piccirillo & Melfi, 1988; Corval et al., 2008). At the Cabo Frio Tectonic Domain, $^{40}Ar/^{39}Ar$ geochronology of magmatic amphibole-biotite aggregates indicates a minimum intrusive age of 132.83 ± 0.30 Ma for mafic dykes with MORB-like compositions (Carvas et al., 2021), coeval with the latest stages of Paraná-Etendeka volcanism (Gomes & Vasconcelos, 2021) and with the onset of seafloor production in the southern South Atlantic (Torsvik et al., 2009). A spatially related and chemically distinct group of mafic dykes, compositionally similar to low-Ti basalts from the northern part of the Paraná-Etendeka province (Ribeira) (Bennio et al., 2003; Schmitt et al., 2016; Savastano et al., 2017), occurs along the same fault systems. No reliable ages exist for this second set of intrusions.

Here, we combine whole-rock geochemistry (major and trace element concentrations as well as Sr, Nd and Pb isotope ratios) with clinopyroxene major element compositions, geothermobarometry, and high-resolution trace element mapping to assess mantle sources, mechanisms of magma supply, and magma emplacement dynamics that may have contributed to continental break-up and formation of an early ocean floor. Results show a considerable shift of the intrusive system from lithospheric to asthenospheric sources and simple to complex magma plumbing mechanisms as the system changed from LIP to MORB-like magmatism at ~132 Ma.

Figure 3.1. (a) Map of the Paraná-Etendeka Magmatic Province (PEMP) during early Cretaceous South Atlantic opening (Piccirillo and Melfi, 1988; Machado et al., 2015; Carvas et al., 2021), exhibiting Serra do Mar Dyke Swarm (SMDS) and Cabo Frio Tectonic Domain (CFTD). Inset: location of PEMP, São Francisco Craton (SF), Congo Craton (CC), Angola block (a) and Ribeira belt (r) around the ancient Gondwana rift. (b) Sampled dykes in the Cabo Frio Tectonic Domain (Schmitt et al., 2016; samples selected for laser ablation ICP-MS analyses are highlighted). (c) Praia do Peró dyke (PPE). (d) Ponta do Criminoso dyke (PCR). (e) Praia Olho-de-Boi dyke (POB). (f) Praia das Conchas dyke (PCO). (g) TAS and Pearce et al. (1996) two-proxy diagrams. Full circles: samples from this study; open circles: samples from Bennio et al. (2003) and Almeida et al., (2021). (h, I, j, k) Minor and trace element normalized by La vs. La concentrations plotted with Low-Ti Paraná-Etendeka basalts and South Atlantic MORB and E-MORB compositions.

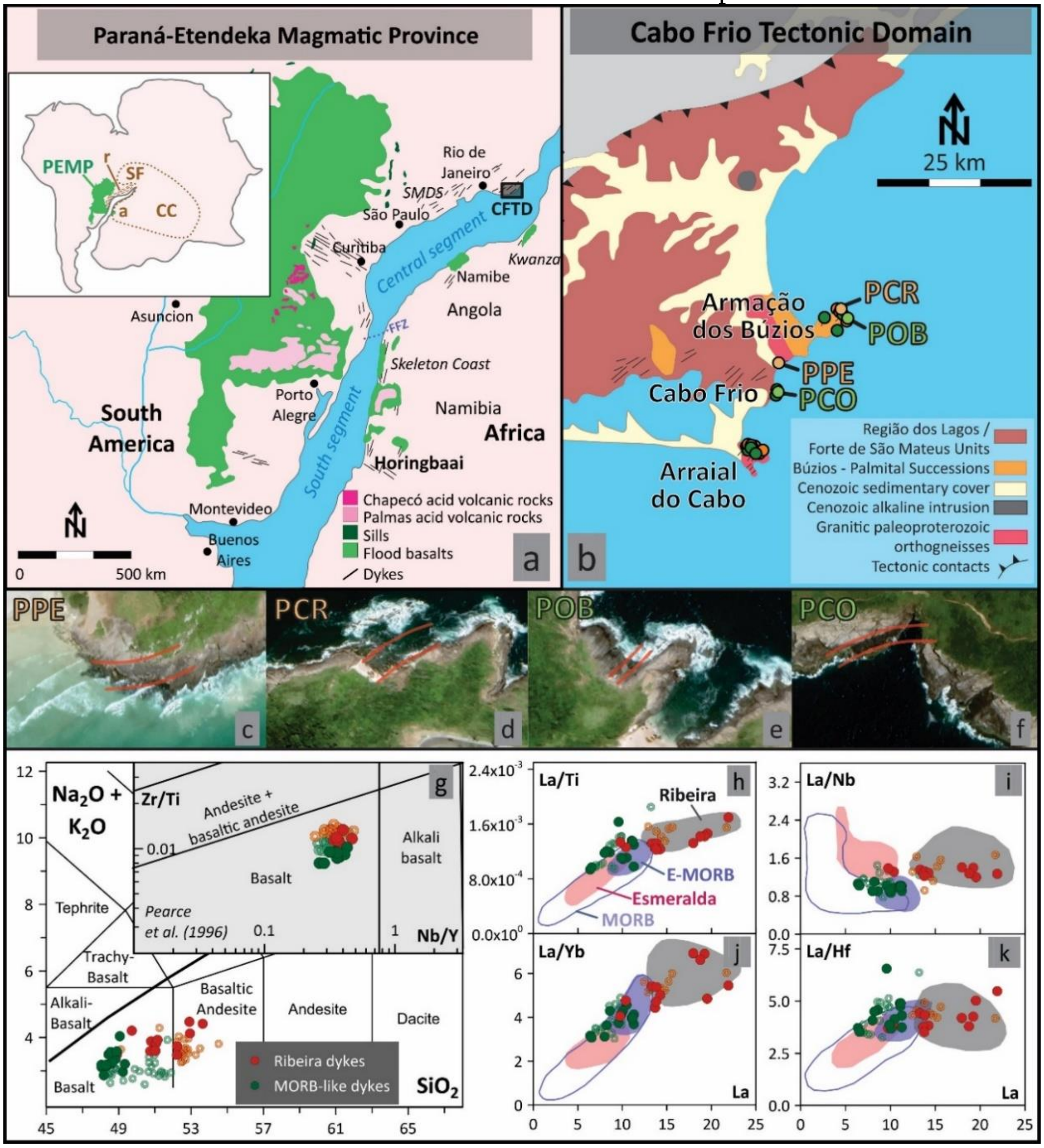

(Carvas et al., submitted)

3.2. GEOLOGICAL CONTEXT

3.2.1. CABO FRIO TECTONIC DOMAIN

The Cabo Frio Tectonic Domain was amalgamated into the Ribeira Belt, a large magmatic arc in the margins of São Francisco Craton (Fig. 3.1A), during the Búzios Orogeny at 520-510 Ma (Fig. 3.1A; Schmitt et al., 2016; and references therein). It comprises two main groups of low- to medium-grade Paleoproterozoic metamorphic rocks (~1970 Ma protoliths; ~520 Ma metamorphism; Schmitt et al., 2004): the Região dos Lagos Unit (felsic metagranitoids, diorites and migmatitic gneisses), and the Forte de São Mateus Unit (amphibolitic banded gneisses; Schmitt et al., 2004; Schmitt et al., 2016). The amphibolitic, calcium silicate, and quartz-feldspar meta-sedimentary and meta-igneous complexes of the Búzios and Palmital units overlap basement rocks and resulted from deposition, magmatism, and deformation during the Búzios Orogeny (Schmitt et al., 2004; Schmitt et al., 2016, and references therein). The tholeiitic dykes investigated in this study intruded during Cretaceous rifting of the Cabo Frio Tectonic Domain (Schmitt et al., 2016; Savastano et al., 2017).

3.2.2. THE SERRA DO MAR DYKE SWARM AND THE LOW-TI DYKES OF THE CABO FRIO TECTONIC DOMAIN

Continental breakup in southeastern Brazil involved the intrusion of voluminous mafic dykes and sills. The vertical/sub-vertical NE-SW intrusions, the Serra do Mar Dyke Swarm, extend along São Paulo and Rio de Janeiro (Fig. 3.1A) (Almeida et al., 1986; Piccirillo & Melfi, 1988; Corval et al., 2008). $^{40}Ar/^{39}Ar$ ages for whole-rock fragments and plagioclase crystals reveal intrusive ages of ~134 to 130 Ma, but step-heating spectra show a much wider range of apparent ages (~155 to ~55 Ma) due to excess argon and/or alteration (Gomes & Vasconcelos, 2021; Carvas et al., 2021; and references therein).

The Serra do Mar dykes are classified into high- and low-Ti groups (HTi: $TiO_2 > 2$ wt%; LTi: $TiO_2 < 2$wt%, respectively); circa 90% of them are petrogenetically similar to HTi Pitanga and Urubici basalts from the Paraná-Etendeka Magmatic Province (e.g., Peate et al., 1992). Some of the rare occurrences of LTi dykes intrude the Cabo Frio Tectonic Domain (Fig. 3.1A, 1B) (Bennio et al., 2003; Corval et al., 2008; Guedes et al., 2016). Their petrogenetic evolution is controversial. Bennio et al. (2003) identified two petrogenetically unrelated magma suites within the Cabo Frio Tectonic Domain: group A, with MORB-like compositions; and group B, very similar to LTi northern Paraná-Etendeka basalts. In contrast, Almeida et al. (2021) interpreted the same two groups of dykes as cogenetic and evolved from a single parental magma through fractional crystallization of augite and plagioclase.

Some ^{40}Ar/^{39}Ar dating of plagioclase crystals from the Cabo Frio Tectonic Domain LTi dykes suggested very young ages (~130 – 55 Ma; Bennio et al. (2003); Almeida et al. (2021)). In contrast, incremental-heating ^{40}Ar/^{39}Ar geochronology of magmatic amphibole-biotite aggregates revealed a minimum intrusive age of 132.83 ± 0.30 Ma for the MORB-like dykes (Carvas et al., 2021). Importantly, Carvas et al. (2021) documented the presence of secondary sericite and albite and showed that the young apparent ages recorded pervasive hydrothermal fluid percolation at ~106 Ma and between 60-30 Ma. Hydrothermal alteration also affected mineral and whole-rock geochemistry. For example, whole-rock LILE and Sr and Pb isotope data show that the Cabo Frio Tectonic Domain mafic dykes were significantly affected by fluid migration.

In this study, we evaluate the effects of hydrothermal alteration on Sr and Pb isotope signatures and use immobile element geochemistry to investigate the petrogenetic characteristics of the Cabo Frio Tectonic Domain dykes. To track magma transport and storage from source to final emplacement site, we combine high-resolution elemental mapping of clinopyroxene crystals with thermobarometry on selected clinopyroxene-melt equilibrium pairs.

3.3. SAMPLING AND ANALYTICAL METHODS

We sampled twenty-four Cabo Frio tholeiitic dykes with an overall trend N40°E-N70°E. Non-weathered and xenolith-free fragments were collected from dykes that range from thin (few meters wide) and aphyric to large (>15 m wide) equigranular (~400 – 800 μm) holocrystalline intrusions with chilled margins. Two of the dykes (Praia das Conchas, PCO, and Ponta do Criminoso, PCR; Fig. 3.1B) were sampled both at their margins and centers.

All samples were characterized with optical microscopy and analyzed by either X-ray fluorescence (XRF) or inductively coupled plasma optical emission spectrometry (ICP-OES) for whole-rock major element composition. Whole-rock trace elements were analyzed by inductively coupled plasma mass spectrometry (ICP-MS). Sr, Nd, and Pb isotopic compositions were obtained by thermal ionization mass spectrometry (TIMS). Mineral composition from representative samples was characterized via scanning electron microscopy (SEM) and electron probe microanalysis (EPMA), and clinopyroxene elemental mapping was carried out by laser ablation ICP-MS (LA-ICP-MS). The chemical results of this study were interpreted together with data from twelve dykes previously published in Carvas et al. (2021).

3.3.1. MAJOR, MINOR AND TRACE ELEMENT WHOLE-ROCK ANALYSES

Samples were prepared for geochemical analyses at the Institute of Astronomy, Geophysics and Atmospheric Sciences of the Universidade de São Paulo (USP), following the protocols described by Carvas et al. (2021). Major and minor oxide XRF and ICP-OES analyses were performed at the XRF Laboratory of the Universidade Estadual Paulista (UNESP – Rio Claro) following procedures described by Nardy et al. (1997) and Machado et al. (2015), and at the Environmental Chemistry Laboratory of The University of Queensland (UQ) following procedures described in Crossingham et al. (2018).

Reference basalts BHVO-2 and BE-N were used as secondary standards in XRF analyses and showed major and minor element accuracy better than 7% (typical values within 1-3%). BHVO-2 and JG-1a standards were analyzed multiple times during the ICP-OES experiments and revealed better than 8% accuracy for most of the oxides (K2O and P2O5 are exceptions, with 16% and 11%, respectively).

Trace elements (REE and Cr, Ni, Ba, Rb, Sr, Zr, Y, Nb, Ta, Th, U, Pb, Hf, Sc, Co) were analyzed by ICP-MS at the Geochemistry Laboratory of the Universidade Estadual de Campinas (UNICAMP) and at the Environmental Chemistry Laboratory of the UQ (procedures described in Crossingham et al., 2018). Compositional measurements of the Paraná-Etendeka standard basalt BRP-1 (Cotta and Enzweiler, 2008) at UNICAMP indicated better than 10% accuracy (Rb and Cr were exceptions with 26% and 46%, respectively); analyses of W2a, BHVO-2, BCR-2 and BIR-1 standards at UQ showed better than 10% accuracy for all elements.

3.3.2. ISOTOPIC ANALYSES

Sr, Nd and Pb isotope compositions of five low-Ti (Ribeira) dykes were measured by TIMS at the Centre of Geochronology and Isotope Geochemistry Research, USP. Sr and Nd measurements followed procedures described by Carvas et al. (2021). For Pb, sample aliquots were loaded in HBr media through columns filled with Biorad AG 1-X8 anion resin; Pb was eluted with 6.0 M HCl. All the procedures were carried out in class 100 laminar flow hoods in a class 10,000 clean room (Marques et al., 1999; 2016).

Sr isotopes were measured with a Triton TIMS (thermal ionization mass spectrometer) in dynamic mode ($^{86}Sr/^{88}Sr = 0.1194$; analytical blank values of 119 pg), with an accuracy of 0.015% for NBS-987 standard ($^{87}Sr/^{86}Sr = 0.710237 \pm 0.000024$, total of 33 analyses during the period of sample analysis). Nd isotope ratios were measured in a Thermo Neptune ICP-MS ($^{146}Nd/^{144}Nd = 0.7219$; blank values below 40 pg) with accuracy of 0.0012% for the JNdi-1 standard ($^{143}Nd/^{144}Nd = 0.512086 \pm 0.000006$; total of 20 measurements).

In addition, four of the MORB-like dykes previously investigated by Carvas et al. (2021) (samples 5, 150, 203, and 206) had their Pb isotope compositions measured in a Finnigan MAT 262 TIMS (fractionation correction factor of 0.13%/a.m.u., blank values below 150 pg). Reference material NBS-981 yielded $^{206}Pb/^{204}Pb$, $^{207}Pb/^{204}Pb$, and $^{208}Pb/^{204}Pb$ average ratios with accuracies of 0.254%, 0.377% and 0.551%, respectively ($^{206}Pb/^{204}Pb = 16.894 \pm 0.006$, $^{207}Pb/^{204}Pb = 15.433 \pm 0.008$ and $^{208}Pb/^{204}Pb = 36.519 \pm 0.024$, total of 93 measurements).

3.3.3. MINERAL CHEMISTRY

Mineralogy and textures were characterized by transmitted- and reflected-light optical microscopy (Nikon Eclipse E400 POL) followed by electron microscopy (Hitachi SU3500 Scanning Electron Microscope equipped with an Energy Dispersive Spectroscopy system; SEM-EDS) in the Centre for Microscopy and Microanalysis at UQ (CMM-UQ). Major element compositions were measured in core-rim transects across selected crystals by Electron Probe Microanalysis (EPMA) with a JEOL JXA-8200 Wavelength Dispersive X-ray Spectrometer (WDS), also at the CMM-UQ. All analytical procedures followed the descriptions of Carvas et al. (2021). Accuracy was generally better than 5%, except for low-concentration elements (< 1 wt% abundance), for which accuracy was better than 20%. The final dataset comprised 338 stoichiometric spot analyses.

Once the EPMA data suggested that clinopyroxene crystals were not significantly affected by hydrothermalism as described by Carvas et al. (2021), major, minor and trace elements were mapped by LA-ICP-MS at the Radiogenic Isotope Facility, Centre for Geoanalytical Mass Spectrometry, UQ (UQ CGMS-RIF), following the methodology of Ubide et al. (2015, 2019). Two representative dykes from each magma suite were selected: PCO and POB (both with MORB-like compositions, from Cabo Frio and Armação dos Búzios, respectively; Fig. 3.1B), and PPE and PCR (with LIP-like compositions also sampled in Cabo Frio and Armação dos Búzios, respectively; Fig. 3.1B). The thin sections were loaded in a dual-volume Laurin Technic ablation cell run with GeoStar Norris software. Clinopyroxene crystals and surrounding groundmass were ablated using an ASI RESOlution 193 nm excimer UV ArF laser by moving the sample stage under the laser beam, generating ablation lines with overlapping squares (3 J/cm^2 fluence, 10 x 10 µm square mask, 10 µm/s translation speed, 10 Hz repetition rate, and 1 µm overlap between lines). The ablation procedure took place in an ultrapure He environment (350 mL/min flow). Ar (850–950 mL/min) and N_2 (5 mL/min) carrier gases contributed to ionization and transport. Ca, Al, Ti, Na, Cr, Ni, Nb, Li, Rb, Sr, Sc, V, Zr, La, Ce, Nd, Sm, Eu and Yb concentrations were measured in a Thermo iCap RQ quadrupole mass spectrometer tuned with NIST612 glass reference material.

Elemental maps were processed with Iolite v.2.5 (Paton et al., 2011) in quantitative mode. Average calcium concentrations in clinopyroxene phenocrysts, as determined by EPMA for each dyke, were applied as internal standard because of the low CaO variation within and between crystals; BHVO-2G was used as the calibration standard. Precision and accuracy were calculated using BCR2G and NIST612 glasses as secondary standards: typical precision was better than 5% for most trace elements (except for Cr, typically <20%) and accuracy was better than 5-10% (Cr and Ni generally range between 10-50%). Al was analyzed by electron microprobe but was also mapped by LA-ICP-MS to track relative variations within crystals.

High precision compositions of crystal zones were extracted from maps using the Monocle add-on for Iolite (Petrus et al., 2017). Aluminum maps were used to identify clinopyroxene sectors and their inner variations, extracted using homogeneous map polygons (i.e., where concentrations had low standard deviations).

3.4. RESULTS

3.4.1. GENERAL PETROGRAPHIC DESCRIPTION

The MORB-type dykes are holocrystalline olivine basalts (Le Maitre, 2002), and comprise plagioclase, clinopyroxene, magnetite, ilmenite and olivine. Many of the intrusions are porphyritic and include phenocrysts of plagioclase (~15% volume fraction; 700-2000µm), clinopyroxene (~15 vol.%; 500-1500 µm), and minor olivine (~10 vol.%; 500 µm) within a microcrystalline matrix of plagioclase (~30 vol.%; maximum 500 µm), pyroxene (~15 vol.%; maximum 200 µm) and magnetite (~10 vol.%; maximum 400 µm) microlites and amphibole/biotite aggregates (~5 vol.%; maximum 200 µm). Wide dykes (>5 m wide) are generally equigranular in the center. Most samples are partially altered and show variable degrees of olivine chloritization and plagioclase sericitization (Carvas et al., 2021); minor amphibole and biotite aggregates result from deuteric alteration of clinopyroxene phenocrysts by late magmatic fluids.

The Ribeira-type dykes are holocrystalline and have basaltic composition (Le Maitre, 2002), with total absence of olivine. Most of the intrusions are porphyritic with plagioclase (~20% volume fraction; 600-2000 µm) and clinopyroxene (~15 vol.%; 500-1000 µm) phenocrysts within a microcrystalline matrix composed of microlites of plagioclase (~25 vol.%; maximum 400 µm), pyroxene (~25 vol.%; maximum 150 µm), magnetite and ilmenite (~10 vol.%; maximum 200 µm) and amphibole/biotite aggregates (~5 vol.%; maximum 300 µm). In general, the Ribeira-type dykes were less affected by secondary fluid percolation than MORB-type dykes, and plagioclase crystals are only slightly sericitized (as further discussed in section 3.5.1.1).

Clinopyroxene phenocrysts from both suites are mostly fresh and sector zoned (cfr. S1 and S2 photomicrographs of supporting information). Sector zoning comprises prism ({100}; {110}; {010}) and hourglass ({-111}) sectors variably oriented throughout the thin sections and identified based on morphology (e.g., Ubide et al., 2019; examples are shown in Fig. 3.4C). Such complex patterns do not occur in groundmass crystals.

3.4.2. MAJOR, MINOR AND TRACE ELEMENTS

All samples are tholeiitic based on mineral major and minor elemental composition and mineral assemblage. Identification of each magma suite was based on rare earth element (REE) and high field strength element (HFSE) signatures (Figs. 1H-K, 2A-E, and Fig. S4 of supporting information). Three of the new samples correspond to the MORB-type basalts, and ten correspond to Ribeira-type (Figs. 1H-K, 2E).

The chemistry of the three MORB-type dykes was evaluated together with data for eleven samples of the same suite published in Carvas et al. (2021), thirteen samples from Almeida et al. (2021), and sixteen samples from Bennio et al. (2003; Fig. 3.1). The rocks are basaltic, plot in the subalkaline field (Fig. 3.1G; Le Bas et al., 1986; Irvine & Baragar,1971) and LOI values are low (between 0.2-1.6 wt%), suggesting little weathering or post-magmatic hydration and carbonation. The basaltic TAS classification agrees with the Pearce et al. (1996) two-proxy diagram, which is less prone to mobility effects (based on Winchester & Floyd, 1977; Fig. 3.1G).

Bulk rock compositions range between 48.0-49.3 wt% SiO_2, 7.0-8.4 wt% MgO, and 1.0-1.9 wt% TiO_2. With decreasing MgO contents, SiO_2, TiO_2, Na_2O, K_2O, Fe_2O_{3t} and P_2O_5 increase while CaO and Al_2O_3 decrease, a typical tholeiitic evolution pattern marked by fractionation of clinopyroxene and plagioclase. New data for the MORB-type dykes largely overlap with the results obtained by Bennio et al. (2003) and Almeida et al. (2021); however, compositions reported by Bennio et al. (2003) show lower MgO, Al_2O_3 and Na_2O, and higher SiO_2 contents.

Data from our 10 Ribeira-type dykes were evaluated together with results for 16 samples from Bennio et al. (2003) and five samples from Almeida et al. (2021). All dykes plot as basalts and basaltic andesites in the TAS diagram and correspond to basalts in the Pearce et al. (1996) two-proxy diagram (Fig. 3.1G). LOI values range between 0.1-0.7 wt%, and SiO_2, MgO and TiO_2 contents range between 48.9-53.6, 5.1-6.9 and 1.2-2.3 wt%, respectively. Major and minor element behavior follows a tholeiitic path based on plagioclase and pyroxene fractionation (Fig. S3 of supporting information) with increasing SiO_2, TiO_2, Na_2O, K_2O, Fe_2O_{3t} and P_2O_5, and decreasing CaO with decreasing MgO concentrations. The Ribeira-type dykes have lower MgO, CaO and Al_2O_3 and higher SiO_2, TiO_2, Na_2O, K_2O and P_2O_5 contents than the MORB-type dykes. Again, Bennio et al. (2003) report lower Na_2O concentrations than our results and those of Almeida et al. (2021).

The two dyke suites exhibit distinct evolutionary trends in La/Yb, La/Ti, La/Nb and La/Hf plots. There are strong similarities between the MORB-type dykes (0.001 ≤ La/Ti ≤ 0.002; 0.9 ≤ La/Nb ≤ 1.1; 3.5 ≤ La/Hf ≤ 6.6) and South Atlantic MORB; in contrast, the group of dykes enriched in more incompatible elements (0.001 ≤ La/Ti ≤ 0.002; 13.7 ≤ La/Tb ≤ 20.6; 1.2 ≤ La/Nb ≤ 1.4; 3.5 ≤ La/Hf ≤ 5.5) are similar to the Paraná-Etendeka low-Ti Ribeira basalts (e.g., Rocha-Júnior et al., 2020). These similarities are evident in other trace element diagrams (Fig. S4 of supporting information).

Rare earth element (REE) patterns of MORB- and Ribeira-type dykes were normalized to CI chondrite (McDonough & Sun, 1995; Figs. 2A, 2C). All samples show enrichment in light REE (MORB-like dykes: 1.4 ≤ $(La/Sm)_{CN}$ ≤ 2.2, mean = 1.8 ± 0.1; Ribeira dykes: 1.8 ≤ $(La/Sm)_{CN}$ ≤ 2.3, mean = 1.9 ± 0.2). $(Dy/Yb)_{CN}$ ratios are lower in the MORB-type dykes (1.09 ≤ $(Dy/Yb)_{CN}$ ≤ 1.34, mean = 1.23 ± 0.09) than in Ribeira-type dykes (1.17 ≤ $(Dy/Yb)_{CN}$ ≤ 1.53, mean = 1.33 ± 0.06), and indicate a stronger fractionation of heavy relative to light REEs in the later.

The less differentiated MORB-type dykes (MgO wt% ≥ 7.5) generally show intermediate and heavy REE compositions similar to N-MORBs. Most of the MORB-type dykes have slightly positive Eu anomalies (0.98 ≤ Eu/Eu* ≤ 1.06, mean = 1.02 ± 0.02). The less differentiated Ribeira-type dykes (MgO wt% ≥ 6.0) are generally depleted in light REE when compared to Ribeira basalts, whereas the more differentiated dykes coincide with typical Ribeira behavior. In general, such dykes do not show significant positive Eu anomalies (0.93 ≤ Eu/Eu* ≤ 1.03, mean = 0.99 ± 0.03).

Figure 3.2. (a) CI-normalized (McDonough and Sun, 1995) REE patterns of MORB-like dykes. Bennio et al. (2003) and by Almeida et al. (2021) results are shown as dashed lines. South Atlantic MORB and E-MORB compositions are also illustrated (Gale et al., 2013). (b) Primitive mantle normalized (McDonough and Sun, 1995) multi-element patterns of MORB-like dykes. (c) CI-normalized REE patterns of Ribeira dykes. Bennio et al. (2003) and by Almeida et al. (2021) results are shown as dashed lines. LTi Ribeira basalt samples from Paraná-Etendeka Magmatic Province are illustrated (Peate, 1997; Marques et al., 1999; references therein). (d) Primitive mantle normalized multi-element patterns of Ribeira dykes. (e) LIP fingerprint diagram (Pearce et al., 2021) exhibiting Cabo Frio Tectonic Domain MORB and Ribeira dykes (symbols as in Fig. 3.1), as well as LTi Ribeira and Esmeralda Paraná-Etendeka basalts, and South Atlantic MORB and E-MORB compositions.

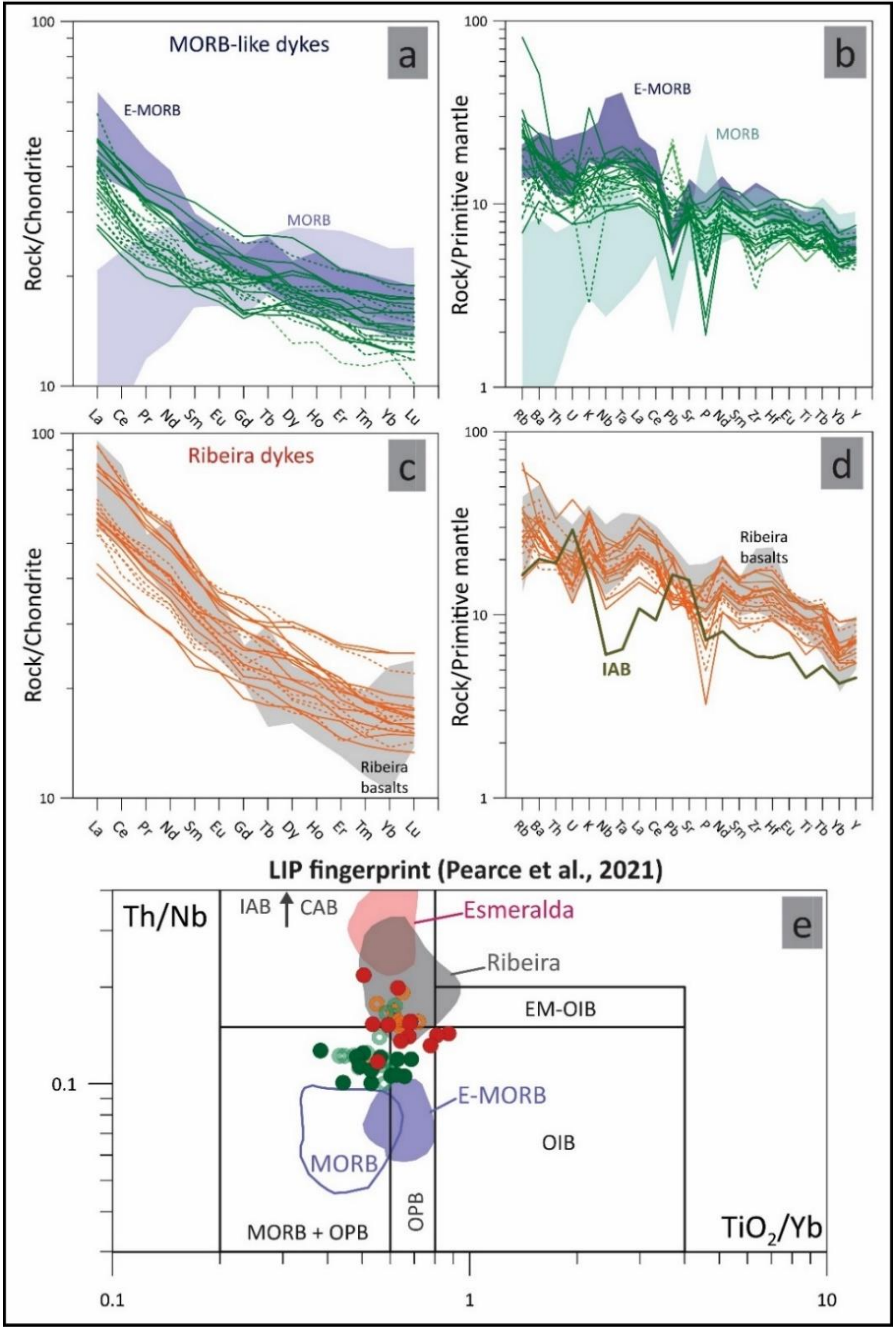

(Carvas et al., submitted)

Apart from the erratic Rb, Ba, K and Pb contents in the MORB-type dykes, resultant from fluid-rock interactions during post-magmatic hydrothermal activity (Carvas et al., 2021), the primitive mantle normalized multi-element diagrams (Figs. 2B, 2D) show that all dykes have negative Ti anomalies. Remarkably, the MORB-type dykes do not show significant $(La/Nb)_{PM}$ anomalies ($0.86 \leq (La/Nb)_{PM} \leq 1.12$, mean = 1.0 ± 0.06, as illustrated in Fig. 3.1I), whereas Ribeira-type dykes show positive values ($1.22 \leq (La/Nb)_{PM} \leq 1.43$, mean = 1.33 ± 0.06), approaching Paraná-Etendeka signatures (Marques et al., 1999) and Island Arc basalts (Kelemen et al., 2014; Figs. 2B, 2D).

3.4.3. SR, ND AND PB ISOTOPE COMPOSITIONS

Initial Sr, Nd and Pb isotope ratios for the MORB-type dykes were calculated using the amphibole $^{40}Ar/^{39}Ar$ age of 132.2 ± 0.48 Ma (Carvas et al., 2021). Given the close compositional relationships between the Ribeira-type dykes and Paraná-Etendeka magmas, and previous reliable intrusion ages for the Serra do Mar Dyke Swarm, which usually approach ~130 Ma (Turner et al., 1994; Deckart et al., 1998; Guedes et al., 2005), we also applied the $^{40}Ar/^{39}Ar$ age of 132.2 ± 0.48 Ma to recalculate their isotopic results.

Sr and Nd ratios are plotted in Fig. 3.3A along with South Atlantic MORB and E-MORB compositions (Gale et al., 2013; and references therein), low-Ti Paraná-Etendeka Ribeira and Esmeralda basalts (Peate, 1997; Marques et al., 1999; Rocha-Júnior et al., 2013, 2020; and references therein), and petrogenetic mixing curves that will be further described and discussed in section 3.5.2.3.

The MORB-type dykes have initial isotope compositions ranging between 0.70374-0.70425 for $^{87}Sr/^{86}Sr$, 0.51256-0.51264 for $^{143}Nd/^{144}Nd$, 17.14-18.16 for $^{206}Pb/^{204}Pb$, 15.51-15.56 for $^{207}Pb/^{204}Pb$, and 38.12-39.17 for $^{208}Pb/^{204}Pb$. Sr and Nd ratios coincide with the South Atlantic E-MORB field, which is more radiogenic in Nd and less radiogenic in Sr than low-Ti Paraná-Etendeka basalts (Fig. 3.3A). The Ribeira-type dykes, on the other hand, range between 0.70563-0.70620 for $^{87}Sr/^{86}Sr$, 0.51226-0.51240 for $^{143}Nd/^{144}Nd$, 17.19-17.76 for $^{206}Pb/^{204}Pb$, 15.48-15.57 for $^{207}Pb/^{204}Pb$, and 38.13-38.77 for $^{208}Pb/^{204}Pb$, and plot almost completely within the Ribeira basalt field (Figs. 3A).

As previously observed, hydrothermal alteration significantly affected Pb isotope signatures in some of the Cabo Frio Tectonic Domain dykes (Fig. 3.3B; Carvas et al., 2021).

The Pb data scatter, however, is less significant for the Ribeira-type dykes, and the ^{206}Pb/^{204}Pb, ^{207}Pb/^{204}Pb and ^{208}Pb/^{204}Pb vs. 1/Pb diagrams confirm their strong resemblances with Paraná-Etendeka low-Ti basalts (Fig. 3.3B).

Figure 3.3. (a) Initial ^{87}Sr/^{86}Sr vs. ^{143}Nd/^{144}Nd compositions of mafic CFTD dykes, along with LTi Esmeralda and Ribeira basalt flows from Paraná-Etendeka Magmatic Province (Peate, 1997; Marques et al., 1999; Rocha-Júnior et al., 2013, 2020; Machado et al., 2015; and references therein), South Atlantic MORB and E-MORB compositions (Gale et al., 2013), and mixing curves involving DMM, pyroxenite and Archean subcontinental lithospheric mantle sources. CC – Regional continental crust (Peixoto et al., 2017). Symbols as in Fig. 3.1. (b) Initial ^{208}Pb/^{204}Pb, ^{207}Pb/^{204}Pb and ^{206}Pb/^{204}Pb ratios vs. 1/Pb. The wide range of Pb concentrations derives from hydrothermal contributions (Carvas et al., 2021). (c) Dy/Yb vs. La/Yb ratios of the most primitive MORB-like and Ribeira dykes along with mantle melting curves for distinct mantle compositions. Sp – Spinel; Grt – Garnet.

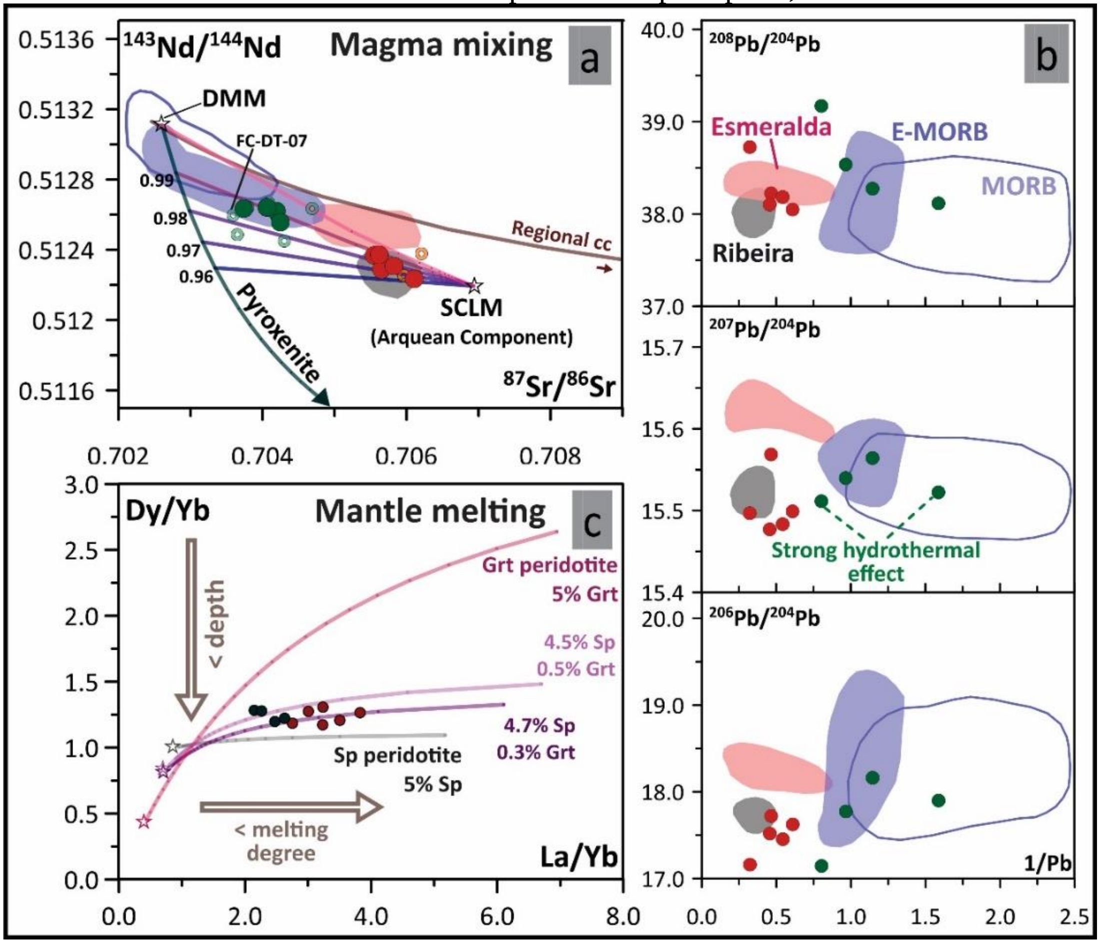

(Carvas et al., submitted)

3.4.4. CLINOPYROXENE MAJOR AND TRACE ELEMENT COMPOSITIONS

Clinopyroxene phenocrysts and groundmass crystals are pristine and their primary magmatic features were not affected by hydrothermal alteration, as indicated by reliable major element results (stoichiometric EPMA analyses with good totals of 100.5 ± 0.7) and the absence of Na anomalies in LA-ICP-MS crystal maps (Figs. S6-S13 of supporting information). Polyhedral phenocrysts from the MORB-type dykes generally show strong sector zoning, suggesting crystallization under a thermal gradient, at low degrees of undercooling (e.g., Mollo & Hammer, 2017; Ubide et al., 2019a, 2019b, 2021; and references therein); simple core-rim zoning was not identified in any of the crystals investigated. Relative to prism sectors, hourglass sectors are Mg- and Si-enriched (average of 11% and 4% in MORB-type dykes, and 4% and 9% in Ribeira-type dykes, respectively) and Ti-, Fe- and Al-depleted (64%, 70% and 8% in MORB-type dykes, and 60%, 67% and 5% in Ribeira-type dykes, respectively).

Sector zoning is not always present in clinopyroxene crystals from Ribeira-type dykes, which primarily display simple core-rim zoning (especially in the central region of the PPE dyke, a ~15m wide intrusion). In such cases, the average core compositions are Al-, Mg-, Cr-, Ni- and Ca-rich in comparison with the mantle (35%, 27%, 94%, 22% and 7%, respectively). In both dyke suites, phenocryst rims are Ti-, Mn-, Na- and Fe-rich when compared to hourglass, prism, core and mantle zones and groundmass crystals.

LA-ICP-MS mapping unveils additional complexities in clinopyroxene crystals. Figure 3.4 shows Ti, Na and Cr maps of representative crystals from the four selected dykes (MORB-type: PCO and POB; Ribeira-type: PPE and PCR; Fig. 3.1B; maps for all the additional crystals and elements are available in Figs. S6-S13 of supporting information). The elemental maps highlight sector zoning (HFSE such as Ti, REE such as Nd, and Cr) and compositional oscillation in concentric bands (Ti and Cr). Concentric chemical gradients are usually negligible or not measurable in major elements; however, trace elements tend to reflect gradual evolution of the magmas, with slight decrease of compatible elements (such as Cr), and slight increase of incompatible elements (e.g., REE, Ti, Al, Zr) from core to rim.

Figure 3.4. (a) LA-ICP-MS elemental maps and cross-polarized photomicrographs of clinopyroxene crystals from MORB-like dykes (PCO – Praia das Conchas dyke; POB – Praia Olho-de-Boi dyke). Colour scales reflect concentration values in parts per million. (b) Clinopyroxene-melt thermobarometry diagrams of the corresponding dykes based on jadeite and enstatite contents (Putirka, 2008; Neave & Putirka, 2017). Depth estimates were calculated based on a 0.30 kbar/km crustal pressure gradient. (c) LA-ICP-MS elemental maps and cross-polarized photomicrographs of clinopyroxene crystals from Ribeira dykes (PPE – Praia do Peró dyke; PCR – Ponta do Criminoso dyke). (d) Clinopyroxene-melt thermobarometry diagrams of the corresponding dykes. (e, f) Cr and Nd concentration gradients of the two MORB-dyke crystals along the transects indicated in Cr maps (a). Nd behavior is representative of all the analyzed incompatible elements, including REEs and HFSEs. Highlighted intervals (violet) correspond to the main oscillatory sections of the transects. Gradients were calculated by applying the numpy.gradient Python routine to the concentration data extracted with Iolite.

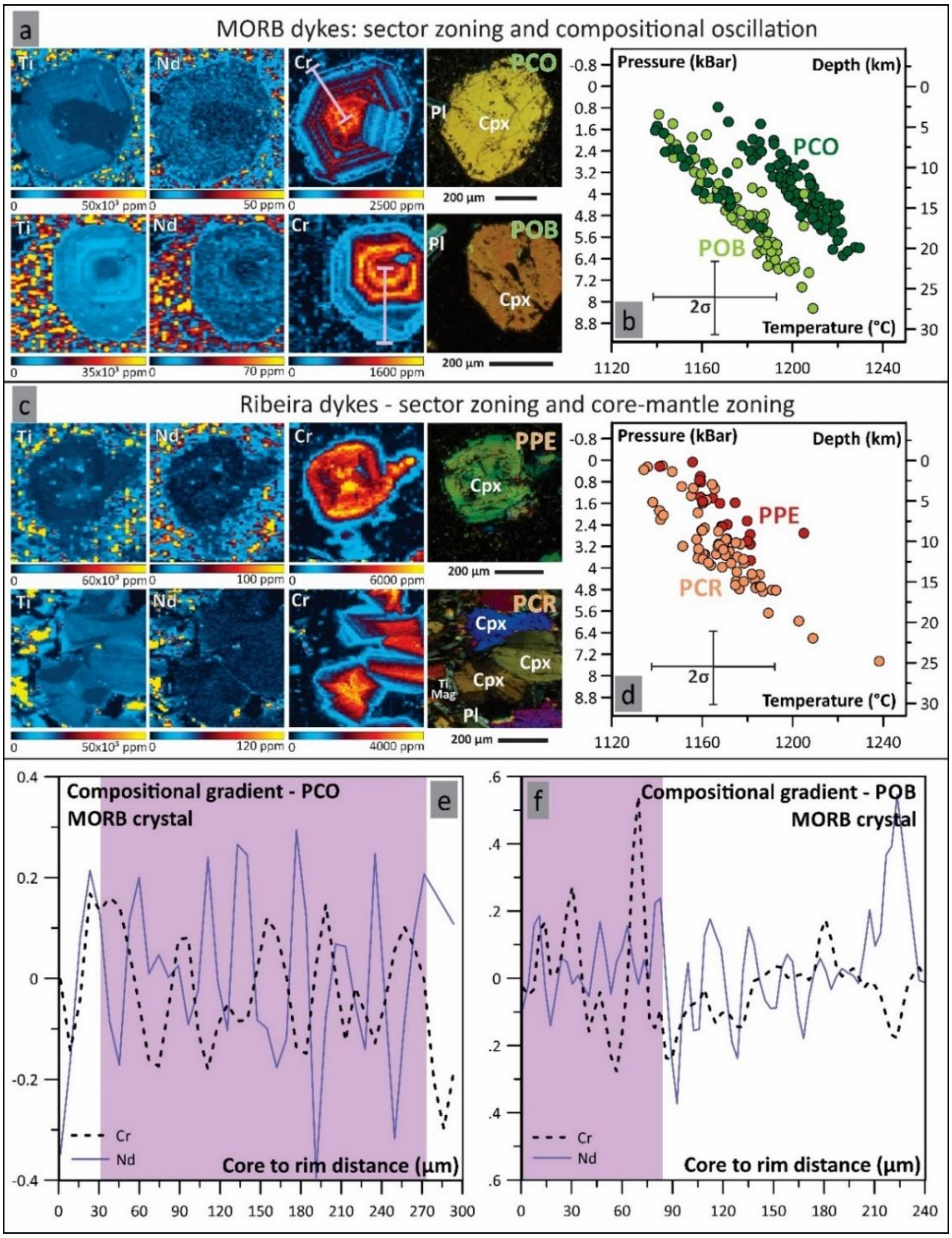

(Carvas et al., submitted)

Elemental maps for the MORB-type dykes confirm the presence of strong sector zoning affecting not only major elements, but also REEs (average of 32% increase in prism sectors), HFSEs (Zr shows 71% increase) and Cr (33% increase). This pattern results from preferential partitioning of Al into prism sectors and the resulting incorporation of highly charged cations to balance Si-Al substitutions (Ubide et al., 2019a). The Cr maps also exhibit enriched cores overgrown by sharp µm-scale concentric, oscillatory layers following euhedral crystal boundaries (up to four cycles); the same concentric patterns are observed in Al, Ti, Zr and REE concentrations, which decrease as Cr increases (see variation diagrams in Figs. 4E, 4F). Such oscillations, below EPMA detection limits, suggest cycling in compositionally distinct magmas via recharge and/or ascent and convection. Low charge elements such as Sr and Ni, on the other hand, do not exhibit oscillations or strong sector zoning.

The clinopyroxene crystals in Ribeira-type dykes, on the other hand, do not show oscillatory zoning, exhibiting instead strong increase in selected elements in prism sectors (Cr, 35%; REE, average of 69%; and HFSEs, e.g., 131% increase in Zr; PCR and PEE crystals in Fig. 3.4C, and Figs. S10-S13 of supporting information). In addition, simple core-rim zoning in HFSEs (e.g., Ti and Zr) and REEs, accompanied by increase in Al, Cr and decrease in Ni from core to rim also occurs. Both behaviors may occur together, such as in the PPE crystal shown in Fig. 3.4C, where the sector-zoned inner cores were outgrown by more homogeneous Ti, Na and Cr distributions in mantle or rim; these crystals have partially resorbed boundaries. Cr and Ni concentrations decrease abruptly (84 and 31%, respectively) towards the outer rims, where slight resorption occurs.

3.4.5. CLINOPYROXENE-MELT THERMOBAROMETRY

The pristine clinopyroxene crystals were suitable to jadeite and enstatite thermobarometry (Putirka, 2008; Neave & Putirka, 2017; and references therein). EPMA data were selected by applying Mg (Dungan et al., 1978), diopside, hedenbergite (Putirka et al., 1996, 1999) and Na partition coefficient equilibrium tests (Blundy et al., 1995; results are available in Fig. S5 of supporting information). Whole-rock geochemistry results were used as magmatic liquid compositions, and we favored component and partition coefficient equilibrium tests over Mg coherence because of the strong sector zoning in the crystals (kinetic effects may disturb and preclude Mg tests; Putirka, 2008; Mollo & Hammer, 2017). The selected clinopyroxene data fit all the equilibrium ranges.

Temperature and pressure estimates were calculated by the iterative models outlined in Putirka et al. (2008; temperature, Eq. 33) and Neave & Putirka (2017; pressure). The thermobarometry data for MORB- and Ribeira-type dykes define linear arrays, within uncertainties (~27 °C and 1.4 kbar), with average and standard deviation values of 1168±13 ºC and 2.8±1.3 kbar for Ribeira-type dykes and 1188±18 ºC and 4.1±1.1 kbar for MORB-type dykes (Figs. 4B, 4D). MORB-type dykes return two temperature clusters (1203±11 and 1174±15 ºC) that correlate positively with dyke thickness, suggesting clinopyroxene crystallization within the intrusion.

3.5. DISCUSSION

3.5.1. GEOCHEMISTRY OF THE CABO FRIO TECTONIC DOMAIN THOLEIITIC DYKES

3.5.1.1. IDENTIFYING THE EFFECTS OF HYDROTHERMAL ALTERATION

Secondary phases associated with plagioclase crystals in the MORB-like dykes show that major, minor and some of the trace elements such as K, Na, Fe, Si, Rb, Ba, Sr, Li, Pb and light REE were unevenly remobilized during hydrothermalism at ~106-105 Ma and 60-30 Ma (Carvas et al., 2021). Rock-fluid interaction variably affected whole-rock compositions and some elements (e.g., K, Na, Rb, Ba, Li and Pb) were significantly affected, precluding their use as petrogenetic indicators (Carvas et al., 2021). Some of the major and minor elements, and all the HFS and RE elements, however, remained relatively unaffected.

Whole-rock data for Ribeira-type dykes, in contrast, show less pronounced hydrothermal effects (Fig. S14 of supporting information). The distinct degrees of alteration between MORB- and Ribeira-type dykes is substantiated by petrographic observations, where MORB-like dykes show higher intensity of plagioclase sericitization and albitization, especially in the vicinities of chloritized olivine crystals (backscatter electron images are provided in Figs. S15 and S16 of supporting information). We interpret that differences in alteration intensity between MORB- and Ribeira-type dykes reflect the presence of olivine in the former and its absence in the latter group. Olivine readily alters to clays by late-stage magmatic fluids, increasing the porosity and permeability of MORB-type dykes and facilitating the migration of hydrothermal fluids.

3.5.1.2. SELECTING SUITABLE PETROGENETIC INDICATORS

To avoid pitfalls associated with alteration effects, we interpreted major element geochemistry excluding K_2O and Na_2O, which are prone to remobilization; trace element geochemistry interpretation relies only on relatively immobile REEs and Y and HFSEs, including Zr, Hf, and Nb. We also quantified the effect of hydrothermal Rb and Sr input onto $^{87}Sr/^{86}Sr$ signatures by calculating mixing curves between the least radiogenic Cabo Frio Tectonic Domain sample (FC-DT-07, $^{87}Sr/^{86}Sr = 0.70359$; from Almeida et al., 2021) and estimated fluid compositions, analogously to the approach of Carvas et al. (2021). Isotopic compositions of possible alteration fluids were estimated from the average signatures of Campos Basin evaporites (immediate offshore basin; Farias et al., 2019; Lima et al., 2020) and Cabo Frio alkaline intrusions (contemporary with hydrothermal circulation; Thompson et al., 1998). Sr concentrations in the fluids were estimated based on the sericitized and albitized areas of plagioclase crystals in MORB-type dykes (LA-ICP-MS data available in Carvas et al., 2021). The mixing curves are available in figure S17 of supporting information.

In our approach, sample FC-DT-07 represents the Sr isotope compositions of unaltered MORB-type dykes in the Cabo Frio Tectonic Domain; they are compatible with E-MORB signatures measured for the South Atlantic (Gale et al., 2013). Samples with lower Sr concentrations than FC-DT-07 are interpreted to have been affected by fluids involving seawater contributions.

3.5.1.3. CHARACTERIZING THE COMPOSITIONS OF DISTINCT MAGMA SUITES

Most Ribeira-type dykes are basaltic andesites, with Zr/Ti values increasing towards the andesitic field and deviating from MORB compositions (Fig. 3.1G). To further assess whole-rock major element distinctions, plagioclase and clinopyroxene fractionation and possible evolutionary paths linking the two magma types, we performed numerous mass balance tests following the methods of Stormer & Nicholls (1978) and combining (i) geochemically similar samples, and (ii) samples from the two dyke groups.

Primitive MORB-type dykes (PCO-18-03 – MgO = 8.44 wt%; and PCO-18-05-I – MgO = 7.57 wt%) were used as parental magmas. Fractionation of clinopyroxene and plagioclase successfully modelled most of these dykes ($8.44 \leq$ MgO ≤ 6.67 wt%) with average residuals of 0.08 – 0.93, and average mass fractionation of 12.9% ± 9.3%. The only exceptions consist of samples from Bennio et al. (2003), probably because of their systematic differences in SiO_2, MgO, Al_2O_3 and Na_2O data.

Mass balance tests yielded similar results for the Ribeira-type dykes. Whole-rock data of selected samples were used as parental liquids (LM-DA-152 – MgO = 6.92 wt%; PPE-18-03 – MgO = 6.28 wt%), and clinopyroxene and plagioclase fractionation generated most of the compositional variations in the samples ($6.92 \leq$ MgO ≤ 4.87 wt%) with average residuals between 0.08 – 0.58 and 17.2 ± 5.6% mean mass fractionation. For both MORB- and Ribeira-type dykes, K_2O and Na_2O oxide residuals were low (MORB: $0.01 \leq K_2O_{res} \leq 0.14$ and $0.02 \leq Na_2O_{res} \leq 0.57$; Ribeira: $0.01 \leq K_2O_{res} \leq 0.23$ and $0.01 \leq Na_2O_{res} \leq 0.40$), validating the modeled evolutionary paths and suggesting that hydrothermal mobility of K and Na (Carvas et al., 2021) does not preclude using these elements in mass balance tests.

The mass balance results for MORB- and Ribeira-type dykes were assessed by comparing calculated and measured contents of immobile trace elements (La, Ce, Nd, Sm, Eu, Gd, Dy, Er, Yb, Lu, Hf and Zr; calculation details are described in text S1 of supporting information). We used published mineral partition coefficients for tholeiitic basalts, calculated bulk partition coefficients using mass balance results, and estimated theoretical trace element concentrations through Rayleigh fractionation formulations (e.g., Albarède, 1995). Average accuracy of modelled trace element concentrations for MORB- and Ribeira-type dykes was between 4-18 and 3-11%, respectively, confirming the reliability of the approach.

To verify possible evolutionary paths linking MORB- and Ribeira-type dykes, we applied mass balance tests to multiple combinations of samples from both groups. The results invariably generated high residuals (≥ 1.0) and large mass fractionation (≥ 60%, an unreasonable subtraction percentage considering the mafic compositions and trace element concentrations of Ribeira samples). The results indicate substantial differences in mantle sources for the two dyke types and suggest a rapid change in mantle-crust interactions during early stages of South Atlantic rifting, on maximum timescales of ~2 Ma (the age gap between peak Paraná-Etendeka volcanism and MORB-type dykes; Gomes & Vasconcelos, 2021; Carvas et al., 2021).

Trace element compositions of MORB- and Ribeira-type dykes are clearly distinct, defining steeper La/Ti, La/Yb and La/Hf trends (Figs. 1H-1K) for the former; the ratio trends match those of low-Ti Esmeralda basalts and South Atlantic MORB and E-MORB compositions. The low La/Nb values of MORB-type dykes and South Atlantic E-MORB compositions (Fig. 3.1I) reflect positive Nb anomalies (that are negative in Ribeira-type dykes and low-Ti Paraná-Etendeka basalts; Fig. 3.2B). The different trends preclude the possibility that the Ribeira-type dykes were products of closed system magmatic differentiation from MORB-like original composition.

The flattened HREE behavior, fractionation of LREE (La-Nd) and positive Nb and Ta anomalies (Figs. 2A-D) reveal further similarities between the MORB-type dykes and South Atlantic MORBs. On the other hand, the negative Nb and Ta anomalies (Fig. 3.2D) of Ribeira-type dykes and low-Ti Paraná-Etendeka basalts imply petrogenetic similarities with island arc basalts and suggest metasomatized SCLM contributions to the magmas with significant influence of oceanic crust recycling in their mantle sources (e.g., Hofmann et al., 1986; Foley et al., 2000). Such influence is also detectable in the Th/Nb and TiO_2/Yb signatures of Ribeira-type dykes (Fig. 3.2E), which plot in the transition between MORB and island/continental arc basalts, whereas the MORB-type dykes largely coincide with the MORB and oceanic plateau basalts domain.

In order to assess the involvement of crustal assimilation in both dyke suites, multiple AFC models comprising regional crustal compositions (Peixoto et al., 2017), ^{143}Nd-rich, ^{87}Sr-poor asthenospheric components and/or average South Atlantic MORB compositions were compared with whole-rock immobile incompatible trace element data (Th, U, Ta, REE), and Sr and Nd isotope ratios. Overall, the AFC results failed to fit the dataset concomitantly, invariably requiring high crustal assimilation (~0.15-0.2) and fractional crystallization rate values to model isotopic compositions that conflicted with major and trace element concentrations. The

AFC modelling also failed to generate Ribeira-type dykes from the MORB-like suite, confirming that the two dyke types were indeed generated from distinct initial magmas.

3.5.2. TRANSITION FROM LIP TO MORB GEODYNAMICS

3.5.2.1. MAGMA DYNAMICS IN THE CRUST

Clinopyroxene crystals are generated in basaltic magmas across a wide range of temperature and pressure conditions (Putirka, 2017), potentially registering magmatic processes along ascending pathways (e.g., Ubide & Kamber, 2018; and references therein). High resolution LA-ICP-MS maps reveal small-scale textural features in crystals from MORB- and Ribeira-type dykes that suggest significant differences between the two plumbing systems.

Sector zoning in clinopyroxenes from both dyke types suggest crystal growth under undercooled conditions (e.g., Ti and Cr maps in Figs. 4A, 4C, and Figs. S6-S13 of supporting information; Mollo & Hammer, 2017; Ubide et al., 2019a). Since most of the clinopyroxene sector compositions are in equilibrium with whole-rock data (Fig. S5 of supporting information), crystallization probably took place under low to intermediate undercooling, favoring growth- instead of nucleation-dominated crystallization (Kirkpatrick, 1977; Ubide et al., 2019b). Such conditions are compatible with the observed equigranular and porphyritic textures (section 3.4.1).

Clinopyroxene crystals from MORB- and Ribeira-type dykes share further chemical parallels. The scale of element partitioning in clinopyroxene sectors of the two dyke groups is similar, suggesting analogous cooling regimes during crystallization (Ubide et al., 2019a). The absence of inner and outer resorption features in most of the crystals (Cr maps in Figs. 4A, 4C, and Figs. S6-S13 of supporting information) indicates similar melt compositions through the ascent pathway in the crust. In addition, the linear positive correlations between pressure and temperature estimates in both magma suites (Figs. 4B, 4D) agrees with clinopyroxene crystallization during magma ascent and emplacement along fault systems. Since Sr and Nd isotope data do not suggest significant contributions from the continental crust (Fig. 3.3A, section 3.5.2.3), such emplacement probably occurred rapidly, within a relatively cool crust, and without major storage, precluding major magma-wall rock interaction.

The occurrence of sector-zoned cores outgrown by chemically homogeneous rims in samples from dyke PPE (Cr map in Fig. 3.4C, and Fig. S13 of supporting information) suggests that Ribeira-type magmas underwent distinct thermal regimes during crystallization: rapid cooling during magma ascent, and subsequent slow cooling within wide intrusive bodies. Importantly, clinopyroxene crystals do not show any compositional oscillatory layers, suggesting that a single magma pulse fed the entire intrusive system. The Cr- and Ni-poor clinopyroxene rims suggest magma fractionation likely related to cooling of the intrusion without further replenishment.

Clinopyroxene crystals from MORB-types dykes, in contrast, are invariably sector-zoned, sometimes exhibiting more primitive (Cr-rich) cores (Cr maps in Fig. 3.4A, and Figs. S6 and S8 of supporting information); such compositional variations suggest fractionation during ascent. Primitive cores often exhibit subtle prism-hourglass contrasts. Given that crystallization occurred during magma ascent, the cores were probably formed under higher pressures and temperatures and lower undercooling regimes.

The most remarkable small-scale texture in crystals from the MORB-type dykes, however, is the widespread chemical oscillatory behavior affecting major, minor and trace element concentrations. The recurrent Cr-rich, and Al-, Ti-, REE-, Zr-depleted zones (Figs. 4E, 4F) suggest magma ascent and/or convection inside conduits that were episodically recharged by slightly more primitive magmas. Thermobarometry results support crystallization under a polybaric and polythermal regimes, and the absence of significant resorption features in the crystals rules out strong compositional contrasts between interacting melts.

The oscillatory zoning may have resulted from rapid replenishment of magma chambers and fault conduits by numerous magma pulses and reflect a change of interaction between the Cabo Frio Tectonic Domain lithospheric block and the upwelled asthenosphere at ~132 Ma. Multiple magma pulses intruded at crustal levels are compatible with a passive margin system where progressive mantle melting through repeated decompression events may have produced rhythmic magma replenishment and ascent through the extending crust.

3.5.2.2. DEPTH OF MAGMA GENERATION

To evaluate source depths for both magma types, we calculated non-modal partial melting Dy/Yb vs. La/Yb curves for variable mantle compositions (Fig. 3.3C; calculation details are described in text S2 of supporting information). Initial trace element concentrations were based on primitive mantle values (McDonough & Sun, 1995), and typical mantle melting coefficients were based on Kinzler (1997), Walter (1998) and Xu et al. (2005).

The selection of possible mantle compositions (comprising variable proportions of olivine, clinopyroxene, orthopyroxene, spinel, and garnet) was based on compositions of primitive samples from each magma suite (MORB-like dykes: MgO ≥ 8.0 wt%; Ribeira dykes: MgO ≥ 6.0 wt%). Most of the primitive MORB- and all the Ribeira-type are compatible with a peridotitic source containing ~4.7 vol.% spinel and ~0.3 vol.% garnet. Some of the primitive MORB-type dyke compositions suggest a slightly higher garnet proportion of ~0.5 vol.% (Fig. 3.3C) and a larger melting column in the mantle. Such difference may result from an increase of lithospheric thinning at ~132 Ma, which potentially widened the mantle decompression interval and the pressure range of the depleted mantle source (e.g., Niu et al., 2021).

3.5.2.3. VARIABLE MANTLE SOURCES AND THE ROLE OF SUBDUCTED SLABS ON MAGMA CHEMISTRY

Modelling Sr, Nd and Pb isotope signatures can further constrain the role of asthenospheric and lithospheric magma sources during continental breakup in the Cabo Frio Tectonic Domain. As stated in section 3.5.1.3, multiple assimilation-fractional crystallization (AFC) models involving regional crust (Peixoto et al., 2017) and asthenospheric components failed to fit isotopic and incompatible trace element data concomitantly. Similarly, the high $^{87}Sr/^{86}Sr$ signatures of simple mixing curves between depleted asthenospheric sources (DMM) and the regional crust (Peixoto et al., 2017; fig. 3.3A) suggest little involvement of crustal assimilation during magma emplacement, indicating instead that elemental enrichment in Ribeira- and MORB-type dykes most likely record lithospheric heterogeneities underneath the Cabo Frio block.

To simulate the influence of subduction events in the Cabo Frio Tectonic Domain lithospheric mantle, we followed the petrogenetic approach of Rocha-Júnior et al. (2020) and calculated mixing curves between DMM-pyroxenite compositions (representative of ancient mantle edges within the SCLM) and a ^{87}Sr-rich Archean SCLM. Mafic alkaline rocks from the northeastern Paraná-Etendeka province mostly derived from mantle sources affected by metasomatism of recycled Paleoproterozoic/Archean slabs (Araújo et al., 2001; Rocha-Júnior et al., 2020; and references therein), and their compositions were used to estimate the ^{87}Sr-rich component. A 1-3% Archean SCLM contribution applied to a 100-96% DMM – 0-4% pyroxenite mantle component (metasomatized lithospheric mantle) successfully models the signatures of Ribeira-type dykes (Fig. 3.3A).

The prevalent involvement of metasomatized lithospheric magmas in the Ribeira-type magmatism at the Cabo Frio Tectonic Domain is consistent with the negative Nb and Ta anomalies and most of the REE behavior (Figs. 3.2C, D; section 3.5.1.3), which cannot be produced by typical asthenospheric melts. Furthermore, clinopyroxene crystallization temperatures of Ribeira-type dykes are lower in comparison with the MORB-type dykes, probably deriving from lower lithospheric solidus temperatures (Figs. 4B, 4D; comparative kernel density curves are available in Figs. S18 and S19 of supporting information).

Sr and Nd isotope data also confirm the similarities between MORB-type dykes and South Atlantic E-MORB magmas (especially sample FC-DT-07, the best estimate of Sr isotopic signatures), despite some Rb and Sr mobility and resulting moderate ^{87}Sr/^{86}Sr scatter (Fig. 3.3A). Hydrothermalism also disturbed Pb isotope signatures (Fig. 3.3B); however, they still largely overlap with E-MORB/N-MORB compositions.

MORB-like magmas are usually associated with eclogitic melt contributions into an asthenospheric, peridotitic mantle reservoir, which partially converts peridotites into olivine-free pyroxenites (e.g., Sobolev et al., 2007); the reaction between eclogitic melts and peridotites potentially provides incompatible element-enriched material to the upper mantle (Sobolev et al., 2005, 2007; Fig. 3.3A). To further evaluate the mantle sources of the MORB-type dykes, we calculated the ^{143}Nd/^{144}Nd vs. ^{87}Sr/^{86}Sr mixing curve between a depleted MORB Mantle (DMM; average D-MORB estimates of Salters & Stracke, 2004) and a pyroxenitic reservoir (websterite xenolith compositions in Carlson & Irving, 1994).

The asthenospheric DMM-pyroxenite combination (Fig. 3.3A) generates the most primitive signatures of the South Atlantic MORB and E-MORB magmas but fails to explain the more evolved oceanic basalts and the MORB-like signatures of the Cabo Frio Tectonic Domain dykes. As previously stated, the dykes do not follow crustal assimilation trends (Fig.

3.3A; Peixoto et al., 2017; comments about AFC models in section 3.5.1.3) and seem to involve a distinct ^{87}Sr-rich and ^{143}Nd-depleted reservoir.

The Archean SCLM reservoir possibly contributing to the Ribeira-type dykes is a reasonable component to model the slight enrichment in ^{87}Sr in the MORB-type dykes. A very small SCLM contribution of 0.2-0.4% (estimated by the FC-DT-07 sample) applied to the 100-98% DMM – 0-2% pyroxenite range (enriched asthenospheric component) is sufficient to produce most of the remaining MORB compositions and suggests interaction between asthenospheric melts and the local lithospheric mantle during MORB-type magma ascent.

The mixing models suggest that intrusive magmas initially derived from typical low-Ti Paraná-Etendeka SCLM sources (Ribeira-type dykes), but they quickly started to rise almost exclusively from a slightly enriched asthenosphere (MORB-type dykes). A schematic representation of the lithospheric and asthenospheric sources and magma conduits through the lithosphere for both suites is illustrated in figure 3.5.

The involvement of metasomatized SCLM (hybridized by pyroxenites during subduction processes) and enriched asthenospheric (eclogite recycling) sources in the Cretaceous tholeiitic magmatism is consistent with the occurrence of recurrent subduction and rifting events during the Cabo Frio Tectonic Domain evolution. Paleoproterozoic rocks of the Região dos Lagos Complex (Fig. 3.1B) probably integrated a reworked continental magmatic arc within the Angola Block in the Congo Craton (~2.0-1.95 Ga; Fig. 3.1A inset; e.g., Schmitt et al., 2008, 2016; and references therein). TDM Nd model ages vary between 2.7-2.4 Ga and imply Archean crust recycling (Schmitt et al., 2008). Some authors suggest the existence of a Paleoproterozoic oceanic crust between the Congo and São Francisco Cratons that underwent eastward subduction beneath the Cabo Frio Tectonic Domain (e.g., Heilbron et al., 2010; Schmitt et al., 2016), which could explain the Archean contribution to the local asthenosphere.

At ~590-560 Ma, a series of N-MORB tholeiitic dykes intruded the basement rocks and were later metamorphosed into ortho-amphibolites (Fernandes et al., 2015; Schmitt et al., 2008, 2016), resulting in the Forte de São Mateus Unit. Circa 580 Ma, Búzios and Palmital successions were deposited between the São Francisco and Congo Cratons (Fig. 3.1B inset; Fernandes et al., 2015; Schmitt et al., 2016). Gondwana amalgamation caused westward subduction of the sedimentary layers underneath the Ribeira Belt at ~ 570 Ma, possibly causing further enrichment and heterogeneity in the lithospheric mantle (Schmitt et al., 2004, 2016; and references therein).

The complex geological history of Cabo Frio Tectonic Domain likely generated shallow Moho discontinuities and a favorable path to ascending asthenospheric magmas during continental breakup (~38 km; Assumpção et al., 2002; Stanton et al., 2010; Schmitt et al., 2016). Such tectonic scenario explains the unique combination of Ribeira- and MORB-type dyke compositions in the Cabo Frio Tectonic Domain.

Figure 3.5. Schematic representation of mantle sources and magma ascent pathways for Ribeira (a) and MORB-like (b) dykes.

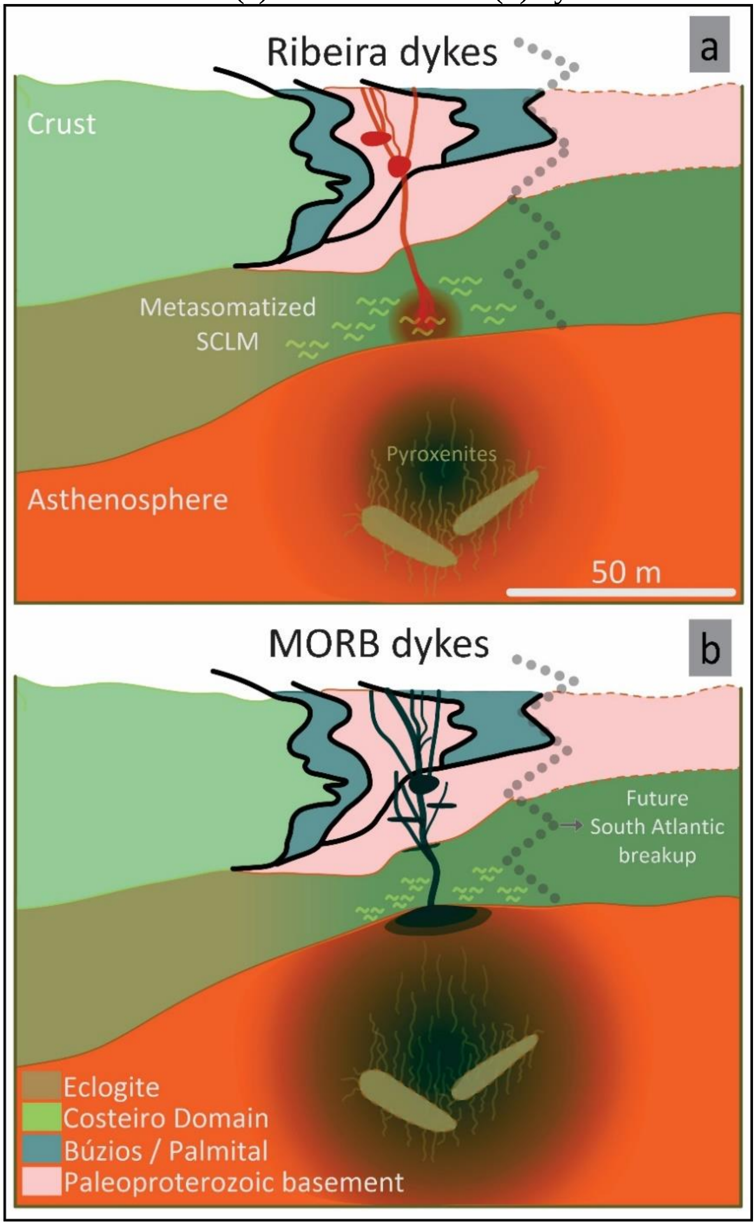

(Carvas et al., submitted)

The geochemical results suggest that early oceanization started in selected areas of the South Atlantic margin during Gondwana breakup (Corti et al., 2003; Ligi et al., 2018; Niu, 2021; Gallacher et al., 2019). Abundant early MORB intrusions and discontinuous and fragmentary oceanic crustal blocks are probably located offshore, in the still poorly mapped transition between hyperextended continental and oceanic crusts along the Brazilian margin (shift from tectonic- to magmatic-driven divergence, e.g., Gillard et al., 2016, 2017). The final transition into normal ocean-floor spreading in the central South Atlantic (~112 Ma; Torsvik et al., 2009) was almost coincident with major changes in plate motion (Granot et al., 2015), and it was followed by margin reactivation (Cogné et al., 2012), abundant on- and offshore alkaline magmatism (Thompson et al., 1998; Ferroni et al., 2018; and references therein), and significant percolation of hydrothermal fluids (Carvas et al., 2021). The early intermittent MORB-like magmatic blocks were probably rotated, deformed, and altered multiple times during these events, failing to produce resolvable magnetic anomalies today. They should, however, be identifiable via suitable geochronology and geochemistry if samples are recovered.

Another possibility to explain the paucity of early ocean floor is that MORB-like magmatism affected large areas along the Brazilian southeast Atlantic margin without ascending to the surface, potentially increasing temperatures and lowering viscosities of the lower crust and modifying its rheological behavior shortly after the main LIP magmatism. In fact, in a recent thermomechanical numerical model of the evolution of divergent margins, Silva & Sacek (2022) propose that a low-viscosity lower crust under a more viscous upper crust results in decoupling and hyperextension of the lithosphere. Emplacement of early and voluminous asthenospheric magmas at depth could have produced such configuration in southeastern Brazil and in other ancient Pangea rifts.

3.5.3. The role of ancient subduction zones in oceanization after rifting

The combination of MORB-like and subduction-influenced magma suites is common within recent and ancient rifting systems. In the northern Red Sea, for example, the western Arabian volcanism exhibits strong similarities with Ocean Island basalts. Occurrences of MORB magmatism, however, gradually increase towards the Red Sea axis, where lithospheric thinning is more significant (Sanfilippo et al., 2019). Analogously, the Paleoproterozoic volcanism in Sarmatia, Eastern Europe, in the Orel-Tim rift, also combined coeval Ocean

Island- and MORB-like basalts resultant from variable interactions between continental crust, SCLM, eclogitized oceanic crust, and the asthenosphere (Tsybulyaev et al., 2021).

Intrusive cases also occur. In the Dronning Maud land, in the Jurassic Africa-Antarctica rift, the Vestfjella dyke swarm combines MORB- and Ocean Island-like intrusions with a predominant depleted mantle source (Luttinen et al., 2015). The rifted continental margin of the Yangtze Block, South Qinling Belt, South China, was intruded by Neoproterozoic mafic dykes from both asthenospheric (N-MORB and E-MORB signatures) and subduction-modified lithospheric mantle sources (Zhao & Azimow, 2018).

All these occurrences suggest that ancient, subducted slabs may play a major role during continental breakup by promoting mantle delamination focused on specific lithospheric blocks, where favorable conditions – such as strong density contrasts, low-viscosity lower crust and low convergence velocity – are present (e.g., Göğüş et al., 2011; Magni et al., 2013; Li et al., 2016; Negredo et al., 2020). The resultant lithospheric thinning permits localized and pronounced asthenosphere upwelling during early stages of rifting and promotes early ascent of largely asthenospheric magmas that may otherwise be trapped in the lithosphere-asthenosphere boundary or within magma chambers in the lower crust.

Such scenario suggests that subducted slabs previously involved in oceanic closure may play a dominant role in weakening localized continental areas, promoting gradual destabilization of the crust, and enabling onset of rifting. Further studies combining whole-rock and high-definition mineral chemistry and geochronology of MORB-like magmatism in similar terrains should provide insights into the rift-to-drift transition during continental breakup.

3.6. CONCLUSIONS

Geochemistry of immobile elements and Sr, Nd and Pb isotope signatures, combined with high-resolution clinopyroxene chemistry and textural analysis indicate that two distinct suites of tholeiitic magmas intruded the Cabo Frio Tectonic Domain during continental breakup that preceded opening of the South Atlantic Ocean. One suite, rich in incompatible elements, shares strong similarities with low-Ti Paraná-Etendeka Ribeira basalts. It is likely derived from heterogeneous SCLM peridotitic sources (~4.7 vol.% Spinel; ~0.3 vol.% Garnet) affected by ancient subduction and comprising a 1-3% Archean SCLM contribution applied to a 100-96% DMM – 0-4% pyroxenite mix. Individual magma pulses feeding subvertical dykes evolved through polybaric fractional crystallization of plagioclase and clinopyroxene during rapid ascent and cooling within the crust.

In contrast, the more primitive magma suite, dated at ~132 Ma, exhibits strong similarities with South Atlantic N-MORB and E-MORB rocks. Chemical and isotopic analyses suggest an asthenospheric peridotitic source (~4.5-4.7 vol.% Spinel; ~0.3-0.5 vol.% Garnet) that consists of 100-98% DMM mixed with 0-2% Pyroxenite slightly enriched by a 0.2-0.4% contribution of an Archean SCLM reservoir during magma ascent. Numerous and rapid magma pulses ascended through the fault system and evolved through plagioclase and clinopyroxene fractional crystallization. Mineral textures and compositions suggest multiple decompression episodes and crustal injection of several pulses of magmas derived from the asthenosphere, consistent with a passive margin setting.

Our results suggest a passive regime plumbing system was intermittently active as early as ~2 Ma after the main peak of LIP volcanism, and that asthenospheric MORB magmas may have affected the continental lithosphere ~20 Ma before the central South Atlantic Ocean floor was established. Our chemical results also coincide with other restricted occurrences of subduction influenced (IAB/OIB) and MORB-like magmatic suites in ancient and recent rifts and suggest that thinned, complex lithospheric blocks affected by ancient subduction and mantle delamination potentially allow localized upwelling of the asthenosphere and preliminary oceanization of crustal margins.

ACKNOWLEDGEMENTS

This research project was supported by Fundação de Amparo à Pesquisa do Estado de São Paulo (FAPESP; Procs. 2012/06082-6, 2014/22948-9, 2017/18232-6, 2018/23650-4), Petrobras, Coordenação de Aperfeiçoamento de Pessoal de Nível Superior (CAPES; Proc. 1425945), and Conselho Nacional de Desenvolvimento Científico e Tecnológico (CNPq; Proc. 141058/2018-8). The microscopy, EPMA, and LA-ICP-MS analyses were funded by UQ-AGES. We thank Dr. Isabela Carmo and Prof. Marcia Ernesto for all the assistance during sampling. We are also very thankful to Dr. Allan Gomes, Dr. Al-Tamini Tapu, Ms. Alice Mcdonald, Dr. Ai Nguyen, Dr. Gang Xia, Dr. Faye Liu, and Ms. Yin Yu for the support during analyses. The authors acknowledge the facilities and the scientific and technical assistance of the Microscopy Australia Facility at the Centre for Microscopy and Microanalysis (CMM), The University of Queensland. LS Marques is a CNPq Research Fellow.

CHAPTER 4 – MAGMATIC EVOLUTION OF THE MAFIC DYKE SUITES OF THE CABO FRIO TECTONIC DOMAIN

The tholeiitic mafic dykes of the Cabo Frio Tectonic Domain record evidence of a localized transition between LIP and passive regime magmatism – evident from a change from lithospheric and asthenospheric mantle sources – during Gondwana breakup, as discussed in Chapter 3. Despite petrogenetic and geodynamic differences, however, clinopyroxene thermobarometric data of Ribeira- and MORB-type dykes display similar behavior and suggest crystallization in the upper crust under polybaric conditions, and during rapid magma ascent (Chapter 3, fig. 3.4). In other words, even though early asthenospheric magma inputs in the southeastern Brazilian margin resulted from several recharge events, they reached the crust at high temperatures, rising through the faults with little or no crystal remnants from intermediate or deep magma chambers, similarly to LIP magmas.

In this chapter, we evaluate the thermobarometry of Ribeira- and MORB-type dykes more closely by applying pressure and temperature estimates obtained from Rhyolite-MELTS 1.2.0 thermodynamic models (Gualda et al., 2012; Ghiorso e Gualda, 2015), and comparing the results with petrographic observations, mass balance results, and whole-rock compositions. Subsequently, we provide a combined assessment of the model results and clinopyroxene chemistry to derive further insights on dyke emplacement and crystallization during continental breakup.

4.1. METHODS

The analytical procedures applied during EPMA, XRF and ICP-OES analyses and mass balance calculations are described in Chapter 3. The EPMA analyses were carried out on representative samples from both magma suites: Ponta do Criminoso dyke (PCR, Ribeira-type suite, Armação dos Búzios, ~15 m wide), Praia do Peró dyke (PPE, Ribeira-type suite, Cabo Frio, ~20 m), Praia Olho-de-Boi dyke (POB, MORB-type suite, Armação dos Búzios, ~1 m), and Praia das Conchas dyke (PCO, MORB-type suite, Cabo Frio, ~25 m).

Clinopyroxene data are stoichiometric and have total oxides between 98-102% (average 100.53% ± 0.7%). In addition to the clinopyroxene results, here we present 29 chemical analyses of biotite and amphibole aggregates with totals >90% (average of 93.3 ± 3.0%; 11 from Ribeira-type dykes and 18 from MORB-type, available in the data repository of Chapter 3). Such aggregates resulted from deuteric reactions between late magmatic fluids and clinopyroxene crystals, as discussed in Chapter 2. All analyses are stoichiometric for either biotite or amphibole compositions.

We thermodynamically modelled the fractional crystallization of Ribeira- and MORB-type magmas under decreasing pressure and temperature conditions with the Rhyolite-MELTS 1.2.0 software (Gualda et al., 2012; Ghiorso e Gualda, 2015). Whole-rock compositions of the most primitive samples of each dyke suite were employed as initial liquid estimates. Dykes PCO (MgO = 8.34 wt%) and LM-DA-208 (MgO = 7.99 wt%; Praia dos Amores, Armação dos Búzios) were selected to simulate initial compositions of MORB-type magmas under 1240-1130°C and 6-1 kBar. Dykes PPE (MgO = 6.47 wt%), LM-DA-152 (MgO = 6.82 wt%; Praia do Pontal, Arraial do Cabo) and F67 (MgO = 6.11 wt%, from Bennio et al., 2003) were selected to model Ribeira-type magmas fractionation under 1240-1120°C and 5-0 kBar.

The modelled evolution curves of liquid phases were compared to the whole-rock geochemical data of Ribeira- and MORB-type dykes. For both suites, the best fits were obtained by:

(i) Applying the -1FMQ buffer (fayalite-magnetite-quartz) for oxidation adjustments, a reasonable oxygen buffer for mafic rocks (i.e., Frost, 1991);

(ii) Ignoring the presence of volatiles in initial magmas. Such condition was necessary to fit Al_2O_3 and CaO decrease in both magma suites that resulted from plagioclase fractionation, and it is coherent with the tholeiitic compositions of the samples and their general low LOI values (average of 0.91 ± 0.09 wt% for MORB-type dykes; 0.43 ± 0.3 wt% for Ribeira-type dykes);

(iii) Applying pressure and temperature intervals that were compatible with clinopyroxene thermobarometry estimates and uncertainties. We started the algorithm at estimated liquidus temperatures and varied initial pressures within the 6-3 kBar for MORB-type dykes, and 5-0.5 kBar for the Ribeira-type dykes. The variation in initial pressures simulated the ascent of hot magmas in chambers and conduits at multiple upper crustal levels and allowed the modelled liquid compositions to fit most of the whole-rock data (except for those extracted from Bennio et al., 2003, which exhibit systematic differences of major element contents when compared with data from other studies).

All Rhyolite-MELTS 1.2.0 outputs for Ribeira- and MORB-type suites are available at the data repository indicated in supplementary material. The analytical procedures applied during EPMA, XRF and ICP-OES analyses and mass balance calculations are described in Chapter 3. The EPMA analyses were carried out on representative samples from both magma suites: Ponta do Criminoso dyke (PCR, Ribeira-type suite, Armação dos Búzios, ~15 m wide), Praia do Peró dyke (PPE, Ribeira-type suite, Cabo Frio, ~20 m), Praia Olho-de-Boi dyke (POB, MORB-type suite, Armação dos Búzios, ~1 m), and Praia das Conchas dyke (PCO, MORB-type suite, Cabo Frio, ~25 m).

Clinopyroxene compositions are stoichiometric and have total oxides between 98-102% (average 100.53% ± 0.7%). In addition to the clinopyroxene results, here we present 29 chemical analyses of biotite and amphibole aggregates with totals >90% (average of 93.3 ± 3.0%; 11 from Ribeira-type dykes and 18 from MORB-type, available in supplementary material X). Such aggregates resulted from deuteric reactions between late magmatic fluids and clinopyroxene crystals, as discussed in Chapter 2. All analyses are stoichiometric for either biotite or amphibole compositions.

We thermodynamically modelled the fractional crystallization of Ribeira- and MORB-type magmas under decreasing pressure and temperature conditions with the Rhyolite-MELTS 1.2.0 software (Gualda et al., 2012; Ghiorso e Gualda, 2015). Whole-rock compositions of the most primitive samples of each dyke suite were employed as initial liquid estimates. Dykes PCO (MgO = 8.34 wt%) and LM-DA-208 (MgO = 7.99 wt%; Praia dos Amores, Armação dos Búzios) were selected to simulate initial compositions of MORB-type magmas under 1240-1130°C and 6-1 kBar. Dykes PPE (MgO = 6.47 wt%), LM-DA-152 (MgO = 6.82 wt%; Praia do Pontal, Arraial do Cabo) and F67 (MgO = 6.11 wt%, from Bennio et al., 2003) were selected to model Ribeira-type magma fractionation under 1240-1120°C and 5-0 kBar.

The modelled evolution curves of liquid phases were compared to the whole-rock geochemical data of Ribeira- and MORB-type dykes. For both suites, the best fits were obtained by:

(iv) Applying the -1FMQ buffer (fayalite-magnetite-quartz) for oxidation adjustments, a reasonable oxygen buffer for mafic rocks (i.e., Frost, 1991);

(v) Ignoring the presence of volatiles in initial magmas, a condition necessary to represent observed Al_2O_3 and CaO decrease in both magma suites that result from plagioclase fractionation. Initially low magmatic volatile contents are consistent with the tholeiitic compositions and the generalized low LOI values of the samples (average of 0.91 ± 0.09 wt% for MORB-type dykes; 0.43 ± 0.3 wt% for Ribeira-type dykes);

(vi) Modelling at pressure and temperature intervals compatible with those derived from clinopyroxene thermobarometry, we started the algorithm at estimated liquidus temperatures and varied initial pressures within the 6-3 kBar for MORB-type dykes, and 5-0.5 kBar for the Ribeira-type dykes. The variation in initial pressures simulated the ascent of hot magmas in chambers and conduits at multiple upper crustal levels and allowed the modelled liquid compositions to fit most of the whole-rock data (except for those extracted from Bennio et al., 2003, which exhibit systematic differences of major element contents when compared with data from other studies).

All Rhyolite-MELTS 1.2.0 outputs for Ribeira- and MORB-type suites are available at supplementary material X.

4.2. RESULTS

4.2.1. EPMA DATA

The majority of the clinopyroxene analyses have augitic compositions according to Morimoto et al.’s (1988) criteria (Fig. 4.1), except for three Fe- and Mg-enriched MORB-type analyses (~50-100 µm; two analyses in the pigeonite field, and one in the clinoenstatite). Most of the matrix EPMA analyses did not meet stoichiometric criteria, probably due to small crystal sizes and influence of adjacent phases in the interaction volume of the electron beam.

Figure 4.1: Ribeira-type (orange circles) and MORB-type (green circles) clinopyroxene composition classification according to Morimoto et al. (1988).

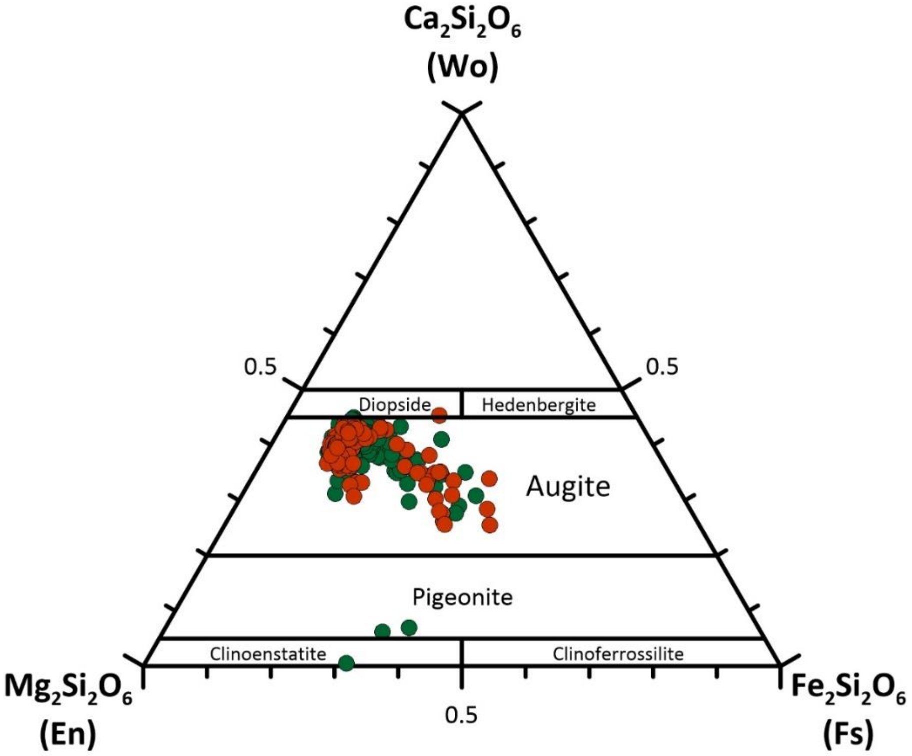

Both Ribeira- and MORB-type clinopyroxene crystals show sector-zoning (prisms sectors, ({1,0,0}; {1,1,0}; {0,1,0}); and hourglasses, ({-1,1,1})); Ribeira-type dykes also have simple core-rim zoning, as discussed in Chapter 3. Major element data in figures 4.2 (Ribeira-type) and 4.3 (MORB-type) are discriminated in compositional zones: prism, hourglass, core, rim and matrix crystals. Rims and matrix analyses often exhibit very similar chemical behavior and are combined in the plots.

Biotite/amphibole aggregate analyses cluster in two main groups: high-MgO (>16 wt%; average 20.9 ± 1.2 wt% for MORB-type dykes; 18.7 ± 1.2 wt% for Ribeira-type) and low-MgO (<16%; average 10.8 ± 1.7 wt% for MORB-type dykes; 12.1 ± 1.3 wt% for Ribeira-type). The high-MgO group is plotted along clinopyroxene results in figures 4.2 and 4.3. CaO concentrations of the aggregates are notably lower than those of clinopyroxene crystals for both Ribeira- and MORB-type suites, whereas MgO contents are similar to core regions in Ribeira-type dykes, and to high-MgO matrix and rims of MORB-type dykes.

Figure 4.2: Ribeira-type clinopyroxene and biotite/amphibole aggregates major element compositions vs. MgO contents. Rhyolite-MELTS 1.2.0 results for CaO, Al_2O_3, FeO_t and Na_2O clinopyroxene concentrations are plotted for comparison. Biotite/amphibole Al_2O_3 concentrations are highly scattered and largely exceed the scale limits, so they were not included in the plot.

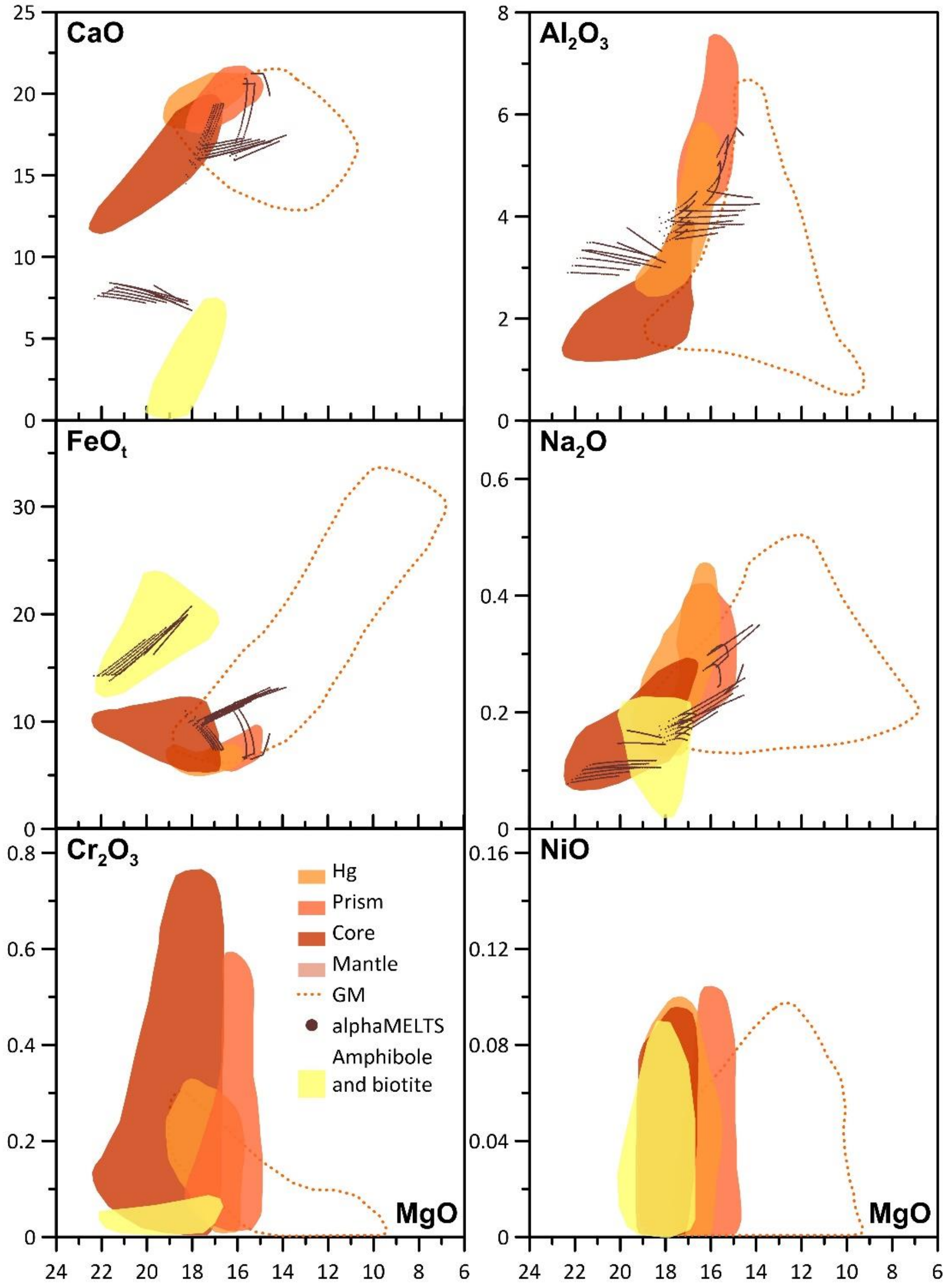

Figure 4.3: MORB-type clinopyroxene and biotite/amphibole aggregates major element compositions vs. MgO contents. Rhyolite-MELTS 1.2.0 results for CaO, Al_2O_3, FeO_t and Na_2O clinopyroxene concentrations are plotted for comparison.

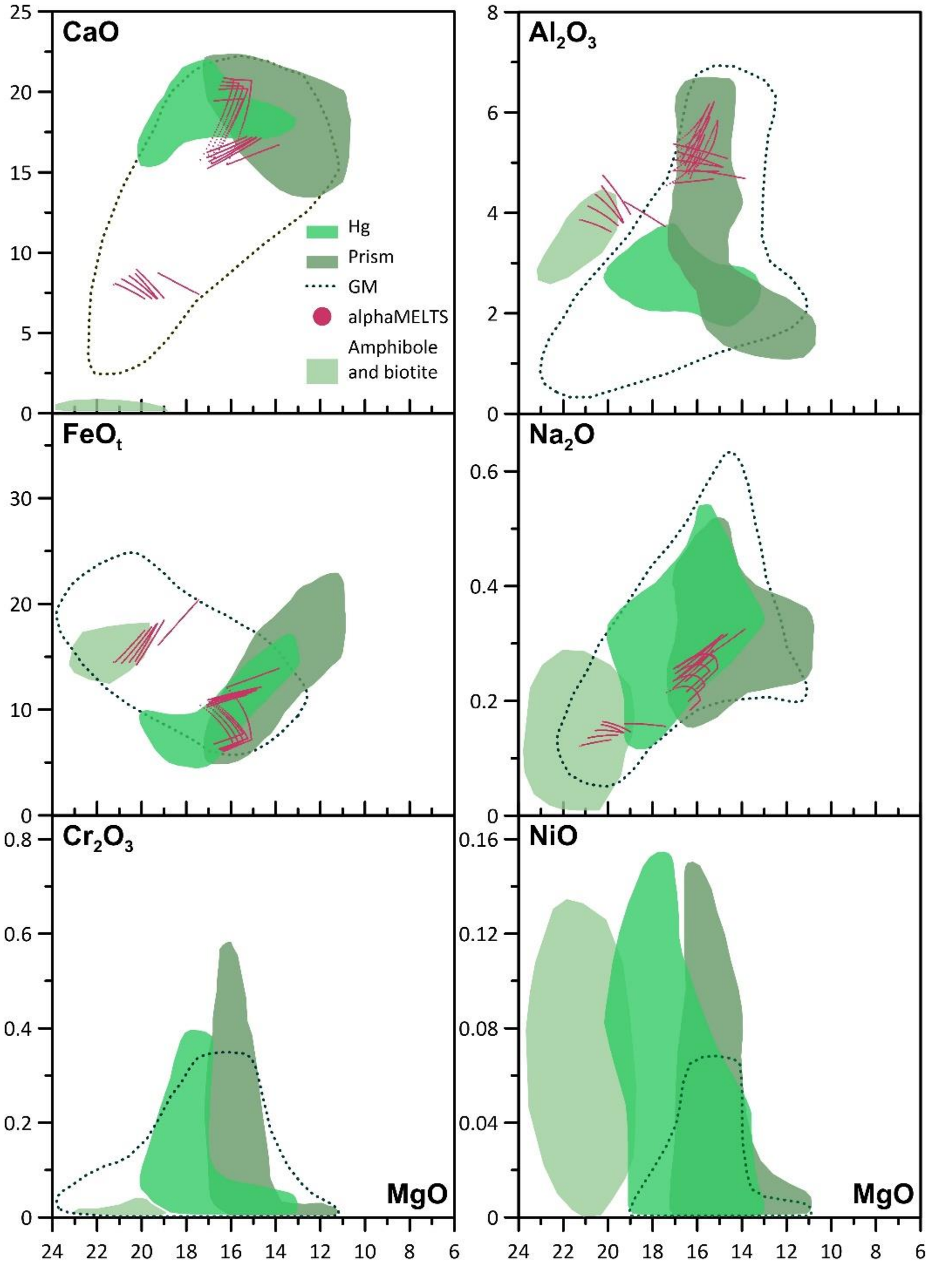

4.2.2. RHYOLITE-MELTS 1.2.0 THERMODYNAMIC MODELS

The models for the chemical evolution of Ribeira-type dykes comprised augitic and pigeonitic clinopyroxene fractionation starting between ~1215-1180°C, plagioclase between ~1220-1195°C, and minor magnetite (included in the "spinel" group) between ~1115-1100°C (variable pressure ranges according to the initial liquid and pressure inputs). The evolution models of the MORB-type suite, on the other hand, comprised augitic and pigeonitic clinopyroxene fractionation at the entire temperature and pressure ranges of thermobarometry estimates. Plagioclase fractionation started between ~1240-1200°C, and minor magnetite crystallization started at ~1120-1100°C.

Liquid lines of descent were plotted together with whole-rock major and minor compositions of both magma suites in figure 4.4. Modelled CaO, Al_2O_3, FeO_t, Na_2O and MgO compositions of Ribeira-type clinopyroxenes were potted together with EPMA data in figure 4.2, while MORB-type clinopyroxenes are shown in figure 4.3. All Rhyolite-MELTS plots were restricted to the clinopyroxene thermobarometric ranges estimated in Chapter 3.

Figure 4.4: MORB- and Ribeira-type whole-rock major and minor element concentrations vs. MgO (symbols as in Fig. 3.2) together with Rhyolite-MELTS 1.2.0 liquid lines of descent (green for MORB-type initial compositions, and orange for Ribeira-type). The lines correspond to distinct pressure intervals (varying initial pressures, as discussed above). The arrows point towards decreasing initial pressures (i.e., hot magmas ascending to shallower crustal depths).

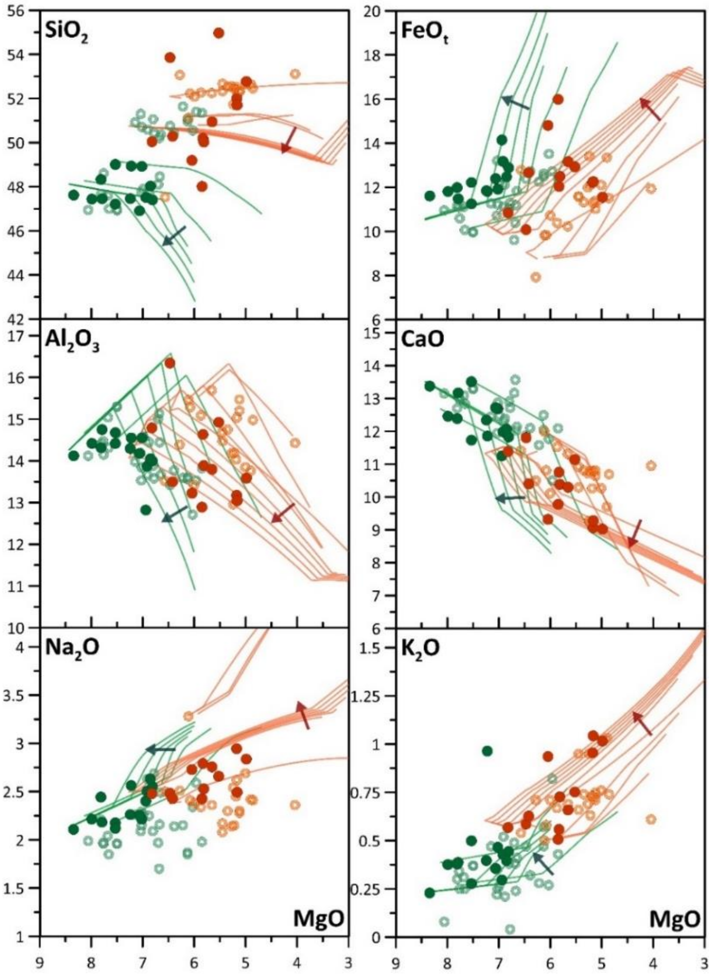

4.3. DISCUSSION

4.3.1. LIQUID LINE OF DESCENT

Rhyolite-MELTS results agree with the mineral assemblage observed by optical microscopy and SEM (Chapter 2), and with the mass balance tests reported in Chapter 3, indicating that the chemical variation of each dyke suite resulted mainly from clinopyroxene and plagioclase crystallization, and that Ribeira- and MORB-type compositions do not correspond to cogenetic evolutionary paths.

As stated above, the liquid lines of descent calculated by the thermodynamic models comprehensibly fit the entire range of whole-rock compositions of both magma suites when variable initial pressures are applied. The decrease of Al_2O_3 and CaO whole-rock concentrations resulting from plagioclase fractionation were also reasonably reproduced by the Rhyolite-MELTS curves. The necessary variation of initial pressures implies that Ribeira- and MORB-type magmas intruded the upper crust at a wide range of depths during supercontinent breakup, and that local crustal heterogeneities probably controlled the extent of magma ascent regardless of mantle sources and dynamics.

4.3.2. CLINOPYROXENE COMPOSITIONS IN RIBEIRA-TYPE DYKES

The PPE dyke is more primitive and its clinopyroxene crystals were generated under lower pressure and higher temperature conditions than those from PCR dykes (Chapter 3). Some of the PPE clinopyroxene crystals exhibit sector-zoned cores which indicate crystallization under low undercooling conditions (temperatures below *solidus*; e.g., Mollo and Hammer, 2017), similarly to clinopyroxene crystals from the PCR dyke (Chapter 3). However, most of the sector-zoned cores from PPE dyke clinopyroxenes are outgrown by homogeneous rims.

The MgO contents of both PPE and PCR clinopyroxene crystals range between 9.1 to 22.1 wt%. High MgO and low Na_2O, CaO and Al_2O_3 concentrations occur in core regions of

PPE phenocrysts. Phenocryst rims display lower MgO contents and pigeonitic compositions, with higher FeO_t, lower Al_2O_3, and negligible Cr_2O_3 and NiO concentrations. Sector-zoned crystals have intermediate MgO, CaO, Na_2O and Cr_2O_3 contents, and are compatible with element partition processes described by Ubide et al. (2019; and references therein), where hourglass sectors are enriched in Mg and depleted in Al in comparison with prism sectors.

Phenocryst rims and matrix crystal signatures of Ribeira-type dykes span from 9.1 to 18.5 wt% MgO. The high MgO concentrations analyzed in groundmass crystals approach core compositions and suggest that some of the crystals formed during initial stages of magma differentiation remained small throughout the fractional crystallization process.

The rims of clinopyroxenes from the PPE dyke do not meet MgO, diopside, hedenbergite and Na partition coefficient equilibrium criteria (described in Chapter 3) when PPE or PCR whole-rock signatures are applied as initial liquid compositions, precluding thermobarometric modelling of a considerable fraction of Ribeira-type EPMA data. Such inconsistency is possibly related to chemical heterogeneities and/or small-scale convection during crystallization of this wide intrusive body (Chapter 3).

The clinopyroxene compositions resultant from the polybaric Rhyolite-MELTS models cluster in two main groups (Fig. 4.2). The first group started to fractionate under high temperatures and pressures and mainly comprises augitic compositions that coincide with the electron microprobe results obtained for core, hourglass and prism crystal segments. Rim and groundmass data shows increased FeO contents and depletion in CaO, Al_2O_3- and MgO that may record *in situ* differentiation during crystallization of the PPE dyke.

The second group of modelled clinopyroxene compositions, which is FeO_t-, Al_2O_3-rich, started its fractionation under intermediate temperatures (~1195-1170°C) and does not correspond to any clinopyroxene EPMA results; however, its MgO, FeO_t and Na_2O compositions largely agree with those of high MgO (>16 wt%) biotite/amphibole aggregates (Fig. 4.4). Such correlation suggests that deuteric alteration by late-stage magmatic fluids probably affected FeO_t-rich clinopyroxene crystals.

4.3.3. CLINOPYROXENE COMPOSITIONS IN MORB-TYPE DYKES

The PCO dyke is more primitive than the POB dyke, and its clinopyroxene crystals formed under higher temperature conditions; however, pressure ranges were very similar for both intrusions. All of the clinopyroxene crystals from MORB-type dykes investigated in this study were sector-zoned, with Al_2O_3-rich prisms and MgO-rich hourglasses (Fig. 4.4). In the central regions of the PCO dyke, clinopyroxene crystals show that Al_2O_3 and MgO contents decrease concomitantly while FeO_t contents increase in the prism sectors of crystals. These trends suggest *in-situ* differentiation resulting from lower cooling rates within wide intrusions.

MgO contents of clinopyroxene crystals from MORB-type dykes range between 21.8 and 11.3 wt%. The lowest concentrations occur in matrix crystals and in prism sectors of the *in-situ* differentiated regions of PCO. Surprisingly, the highest MgO contents occur in matrix clinopyroxene crystals from both the PCO and the POB dykes. These MgO-rich clinopyroxene matrix crystals could represent small cores from early crystallization stages, or they could represent antecrysts; however, their Cr_2O_3-poor signatures do not support these hypotheses. Instead, such matrix crystals were likely generated during multiple episodes of replenishment of PCO and POB plumbing systems by MgO-rich magmas (as exposed by LA-ICP-MS analyses and discussed in Chapter 3).

Rhyolite-MELTS models for MORB-type clinopyroxene fractionation clustered in two distinct compositional groups. The first group crystallized under higher temperature conditions and largely coincides with prism and hourglass signatures. The second group, FeO_t-rich, started its crystallization between ~1200-1180°C. The modelled MgO, CaO, FeO_t and Na_2O contents of clinopyroxene rims and coexisting groundmass match the values measured by EPMA analyses.

Similarly to Ribeira-type dykes, FeO_t-rich clinopyroxene crystals from MORB-type dykes seem to have been more affected by deuteric alterations during late stages of magmatic differentiation. The high-MgO (>16 wt%) biotite/amphibole compositions share similarities with FeO_t-rich Rhyolite-MELTS results in terms of MgO, Al_2O_3, FeOt and Na_2O concentrations (Fig. 4.3). Correspondingly, pigeonitic, FeO_t- and MgO-rich clinopyroxene compositions detected during EPMA analyses (Fig. 4.1) were localized in the vicinities of biotite/amphibole aggregates in MORB-type dykes.

4.4. CONCLUSIONS

The polybaric crystallization of Ribeira- and MORB-type magmas, starting at variable upper crustal depths, successfully accounted for the complete range of whole-rock and most of the clinopyroxene mineral compositions. The variation of initial clinopyroxene crystallization pressures suggests that Ribeira- and MORB-type hot magma ascent (i.e., both lithospheric and asthenospheric magma inputs) was likely controlled by local crustal heterogeneities rather than the character of mantle sources and/or magma dynamics and frequency of recharges. In addition, the Rhyolite-MELTS crystallization models suggest that Fe-rich clinopyroxene phases were chemically affected by late-stage magmatic fluids, resulting in deuteric biotite/amphibole aggregates.

CHAPTER 5 - CONCLUSION

This PhD thesis investigated the initial stages of oceanization during South America-Africa break-up and South Atlantic opening by assessing the geochronology, petrogenesis and magma dynamics of mafic tholeiitic dykes from the Cabo Frio Tectonic Domain, southeastern Brazil. We focused our efforts on defining better age estimates for the MORB-type dykes from this area, assessing the effects of magma-water interaction on the geochemistry and the radiogenic isotope systematics – including the K-Ar system – of the dykes, and on modelling petrogenesis, magmatic evolution, ascent, and emplacement for MORB- and Paraná-Etendeka-type dykes.

The geochemistry and $^{40}Ar/^{39}Ar$ geochronology of MORB-type dykes, which comprise Chapter 2 of the thesis, were reported in a *Geochimica and Cosmochimica Acta* publication entitled "Geochronology of mafic magmatism and hydrothermal alteration during early stages of South Atlantic opening". The paper explored intrusion and alteration ages, the chemical and isotopic effects of rock-water interaction, and investigated potential fluid sources by analyzing (i) $^{40}Ar/^{39}Ar$ systematics of whole-rock fragments, fresh and altered plagioclase crystals, and amphibole and biotite aggregates; (ii) whole-rock major and minor element contents (XRF), and trace element concentrations (ICP-MS); (iii) whole-rock Sr (TIMS) and Nd (ICP-MS) isotopic signatures; (iv) mineral chemistry (EPMA); and (v) high-resolution elemental maps of altered plagioclase crystals (LA-ICP-MS). The main implications of the study are:

- MORB-type dykes intruded the Cabo Frio Tectonic Domain at 132.83 ± 0.30 Ma, the measured crystallization age of deuteric amphibole and biotite aggregates formed in the final stages of magma crystallization during late stages of the Paraná-Etendeka volcanism;
- Hydrothermal fluids enriched in K, Na, Rb, Ba, Sr, Si, Li, Fe, Pb and light-REE affected the plagioclase K-Ar system. Two main events of alteration – sericitization between ~106-105 Ma and albitization between 60-30 Ma – were identified;
- Hydrothermal solutions modified whole-rock K, Sr, Rb, Ba, and Pb contents and Pb-isotope compositions;
- Estimates of fluid composition, alteration ages and whole-rock Sr isotopes suggest that interactions between alkaline magmatism and basinal fluids from offshore basins scavenged K and Na from evaporitic layers, triggering K- and Na-rich metasomatism along the Southeast Brazilian margin. Fluid percolation potentially reached other mafic intrusions associated with

Gondwana breakup and South Atlantic opening, and further investigation is needed to constrain the effect of hydrothermal alteration on the ^{40}Ar/^{39}Ar systematics of other intrusive bodies.

The petrogenesis and magma dynamics of LIP- and MORB-type dykes were investigated and reported in a manuscript entitled “Tracking the transition from a Gondwana LIP to the South Atlantic Ocean with geochronological and geochemical indicators” and submitted to the *Journal of Geophysical Research*; this manuscript comprises Chapter 3. This investigation included: (i) whole-rock major and minor compositions (XRF and ICP-OES), and trace element concentrations (ICP-MS); (ii) whole-rock Sr (TIMS), Nd (ICP-MS), and Pb (TIMS) isotopic signatures; (iii) mineral chemistry (EPMA) of all phases, which were applied in mass-balance tests and thermobarometric models; and (iv) elemental mapping of clinopyroxene crystals (LA-ICP-MS). The results led to the following conclusions:

- During Gondwana breakup, the Cabo Frio Tectonic Domain was intruded by two distinct and non-cogenetic tholeiitic magma suites;
- The first suite shares major similarities with low-Ti Ribeira magmas from the Paraná-Etendeka Magmatic Province. The dykes were derived from a largely metasomatized lithospheric peridotitic source (~4.7% spinel; ~0.3% garnet) that comprised a 1-3% ancient SCLM contribution applied to a 100-96% DMM – 0-4% pyroxenite mixture. The Ribeira-type magmas ascended to the crust as a single, strong pulse, and evolved through plagioclase and clinopyroxene fractionation under polybaric conditions;
- The second magma suite, emplaced at ~132 Ma, shares multiple chemical similarities with South Atlantic MORB and E-MORB rocks. These dykes were derived from a primarily asthenospheric, peridotitic source (~4.5-4.7% spinel; ~0.3-0.5 garnet) consisting of a 100-98% DMM – 0-2% pyroxenite mixture with circa 0.2-0.4% ancient SCLM contribution. Magma ascent and emplacement were fed by a series of recharge events, and magmas evolved through plagioclase and clinopyroxene fractional crystallization under polybaric conditions;
- High-resolution geochemical textures and thermobarometry estimates of MORB-type dykes suggest that the multiple recharge events resulted from episodic decompression of the asthenospheric source, and imply an intermittent and confined passive system in the Brazilian southeast margin as early as ~2 Ma after peak LIP volcanism;
- A combination of subduction-influenced lithospheric and asthenospheric magma suites commonly occurs in ancient and recent rifts globally. Such occurrences suggest that restricted blocks with complex tectonic structures, affected by crustal thinning and mantle delamination,

potentially promote and/or enhance asthenospheric magmatism and early oceanization of the continental crust;

- Regardless of the initial triggers of lithospheric distension and LIP volcanism (mantle plume, thermal anomaly, mantle delamination etc.), the results imply that localized oceanization possibly takes place during early stages of rifting within fragile segments of the margin. Occurrences of onshore MORB magmatism consist of rare records of this transitional process that results in gradual weakening of the continental crust.

The additional assessment of whole-rock and clinopyroxene crystals and biotite/amphibole aggregate compositions based on thermobarometry and thermodynamic Rhyolite-MELTS models revealed that:

- Polybaric crystallization of Ribeira- and MORB-type magmas, starting at variable upper crustal depths, accounts for the complete range of whole-rock and most of the clinopyroxene mineral compositions;
- Such pressure variation implies that local crustal heterogeneities probably controlled Ribeira- and MORB-type hot magma ascent regardless of mantle sources and dynamics;
- Thermodynamic crystallization models suggest that Fe-rich clinopyroxene phases were largely altered by late-stage magmatic fluids, resulting in deuteric biotite/amphibole aggregates.

This research project reveals that intrusive igneous rocks associated with ancient and recent rifts keep precise but poorly explored records of the evolution of lithosphere-asthenosphere interactions during continental breakup – a topic of fundamental relevance in the study of divergent tectonics. Further sampling of onshore MORB-like rocks in distinct rifts and careful assessment of reliable geochemical and geochronological data is needed to better constrain the progressive evolution of magma sources, dynamics and timescales during supercontinent breakup. Investigation of secondary phases is crucial, as they might affect primary signatures, and may provide additional information about late tectonic events related to ocean crust formation.

REFERENCES

ALBARÈDE, F. **Introduction to Geochemical Modeling**. Cambridge University Press, 1995. https://doi.org/10.1017/CBO9780511622960

ALMEIDA, F.F.M. Distribuição regional e relações tectônicas do magmatismo pós–paleozóico no Brasil. **Revista Brasileira de Geociências**, n. 16(4), p. 325-349, 1986. https://doi.org/10.25249/0375-7536.1986325349

ALMEIDA, J.; DIOS, F.; MOHRIAK, W. U.; VALERIANO, C. D. M.; HEILBRON, M.; EIRADO, L. G.; TOMAZZOLI, E. Pre-rift tectonic scenario of the Eo-Cretaceous Gondwana break-up along SE Brazil–SW Africa: insights from tholeiitic mafic dyke swarms. **Geological Society, London, Special Publications**, n. 369, p. 11–40, 2013. https://doi.org/10.1144/SP369.24

ALMEIDA, J.; HEILBRON, M.; GUEDES, E.; NEUBAUER, F.; MANFRED, B.; KLAUSEN, M. B.; VALERIANO, C. M.; BRUNO, H.; GIRO, J. P.; MCMASTER, M.; TETZNER W. Pre-to-syn tholeiitic magmatism in a transtensive hyperextended continental margin: Onshore and offshore magmatism of the Campos Basin, SE Brazil. **Journal of South American Earth Sciences**, n. 108, 103218, 2021. https://doi.org/10.1016/j.jsames.2021.103218

ARAÚJO, A.L.N.; CARLSON, R.W.; GASPAR, J.C.; BIZZI, L.A. Petrology of kamafugites and kimberlites from the Alto Paranaiba alkaline Province, Minas Gerais, Brazil. **Contributions to Mineralogy and Petrology**, n. 142, p. 163–177, 2001. https://doi.org/10.1007/s004100100280

ARTH, J.G.. Behavior of trace elements during magmatic processes - A summary of theoretical models and their applications. **Journal of Research of the US Geological Survey**, n. 4, p. 41-47, 1976.

ASSUMPÇÃO, M.; MARZA, V.; BARROS, L.; CHIMPLIGANOND, C.; SOARES, J. E.; CARVALHO, J.; CAIXETA, D.; AMORIN, A.; CABRAL, E. Reservoir induced seismicity in Brazil. **Pure Applied Geophysics**, n. 159, p. 597–617, 2002. https://doi.org/10.1785/0120170364

BAKSI, A. K.; ARCHIBALD, D. A. Mesozoic igneous activity in the Maranhão province, northern Brazil: 40Ar/ 39Ar evidence for separate episodes of basaltic magmatism. **Earth and Planetary Science Letters**, n. 151(3/4), p. 139–153, 1997. https://doi.org/10.1016/S0012-821X(97)81844-4

BELLIENI, G.; MONTES-LAUAR, C. R.; DE MIN, A.; PICCIRILLO, E. M.; CAVAZINI, G.; MELFI, A. J.; PACCA, I. G. Early and Late Cretaceous magmatism from São Sebastião island (SE-Brazil): geochemistry and petrology. **Geochimica Brasiliensis**, n. 4(1), p. 59–83, 1990. http://dx.doi.org/10.21715/gb.v1i4.31

BENNIO, L.; BROTZU, P.; D'ANTONIO, M.; FERAUD, G.; GOMES, C. B.; MARZOLI, A.; MELLUSO, L.; MORBIDELLI, L.; MORRA, V.; RAPAILLE, C.; RUBERTI, E. The tholeiitic dyke swarm of the Arraial do Cabo peninsula (SE Brazil): 39Ar/40Ar ages, petrogenesis, and regional significance. **Journal of South American Earth Sciences**, n. 16, p. 163–176, 2003. https://doi.org/10.1016/S0895-9811(03)00030-0

BLUNDY, J. D.; FALLOON, T. J.; WOOD, B. J.; DALTON, J. A. Sodium partitioning between clinopyroxene and silicate melts. **Journal of Geophysical Research: Solid Earth**, n. 100, p. 15501–15515, 1995. https://doi.org/10.1029/95JB00954

CARLSON, R.W.; IRVING, A.J. Depletion and enrichment history of subcontinental and lithospheric mantle: an Os, Sr, Nd and Pb isotopic study from the northwestern Wyoming Craton. **Earth and Planetary Science Letters**, n. 126, p. 457–472, 1994. https://doi.org/10.1016/0012-821X(94)90124-4

CARVAS, K.Z.; VASCONCELOS, P.M.P.; MARQUES, L.S.; UBIDE, T.; CARMO, I.O.; BABINSKI, M. Geochronology of mafic magmatism and hydrothermal alteration during early stages of South Atlantic opening. **Geochimica et Cosmochimica Acta**, n. 314, p. 358-380, 2021. https://doi.org/10.1016/j.gca.2021.08.017

COGNÉ, N.; GALLAGHER, K.; COBBOLD, P. R.; RICCOMINI, C.; GAUTHERON, C. Post-breakup tectonics in southeast Brazil from thermochronological data and combined inverse-forward thermal history modeling. **Journal of Geophysical Research: Solid Earth**, n. 117, p. B11413, 2012. https://doi.org/10.1029/2012JB009340

CORVAL, A.; VALENTE, S. C.; DUARTE, B. P.; FAMELLI, N.; ZANON, M. Dados petrológicos dos diabásios dos setores centronorte e nordeste do Enxame de Diques da Serra do Mar. **Geochimica Brasiliensis**, n. 22(3), p. 159–177, 2008. http://dx.doi.org/10.21715/gb.v22i3.286

COTTA, A.; ENZWEILER, J. Certificate of Analysis of the Reference Material BRP-1 (Basalt Ribeirão Preto). **Geostandards and Geoanalytical Research**, n. 32, p. 231–235, 2008. https://doi.org/10.1111/j.1751-908X.2008.00894.x

CORTI, G.; WIJK, J.; BONINI, M.; SOKOUTIS, D.; CLOETINGH, S.; INNOCENTI, F.; PIERO, M.; BONINI, M. Transition from continental break-up to punctiform seafloor spreading: How fast, symmetric and magmatic. **Geophysical Research Letters**, n. 30, p. 1-4, 2003. https://doi.org/10.1029/2003GL017374

CROSSINGHAM, T.; UBIDE, T.; VASCONCELOS, P.; MALLMANN, G. Parallel Plumbing Systems Feeding a Pair of Coeval Volcanoes in Eastern Australia. **Journal of Petrology**, n. 59, p. 1035-1066, 2018. https://doi.org/10.1093/petrology/egy054

DE PIERI, R.; GREGNANIN, A.; STELLA, R.; VALENTINI, M.T.G. Coefficienti di distribuzione cristallo-liquido dei minerali nelle trachiti e rioliti dei Colli Euganei. **Memorie degli Istituti di Geologia e Mineralogia dell' Universita di Padova**, n. 36, p. 461-498, 1984.

DECKART, K.; FÉRAUD, G.; MARQUES, L. S.; BERTRAND, H. New time constraints on dyke swarms related to the Paraná- Etendeka magmatic province, and subsequent South Atlantic opening, southeastern Brazil. **Journal of Volcanology and Geothermal Research**, n. 80, p. 67–83, 1998. https://doi.org/10.1016/S0377-0273(97)00038-3

DEINO, A.L. **Mass Spec – version 7.884 – Program documentation**. Berkeley Geochronology Center, 2012.

DENG, Y.; REN, J.; GUO, Q.; CAO, J.; WANG, H.; LIU, C. Rare earth element geochemistry characteristics of seawater and porewater from deep sea in western Pacific. **Scientific Reports**, n. 7, p. 16539, 2017. https://doi.org/10.1038/s41598-017-16379-1

DUNCAN, A. M.; PRESTON, R. M. F. Chemical variation of clinopyroxene phenocrysts from the trachybasaltic lavas of Mount Etna, Sicily. **Mineralogical Magazine**, n. 43, p. 765–770, 1980. https://doi.org/10.1180/minmag.1980.043.330.10

ELDERFIELD, H. The oceanic chemistry of the rare-earth elements. **Philosophical Transactions of the Royal Society of London. Series A, Mathematical and Physical Sciences**, n. 325, p. 105–126, 1988. https://doi.org/10.1098/rsta.1988.0046

EWART, A.; TAYLOR, S.R. Trace element geochemistry of the rhyolitic volcanic rocks, Central North Island, New Zealand. **Contributions to Mineralogy and Petrology**, n. 22, p. 127-146, 1969. https://doi.org/10.1007/BF00372400

EWART, A.; BRYAN, W.B.; GILL, J.B. Mineralogy and geochemistry of the younger volcanic islands of Tonga. S. W. Pacific. **Journal of Petrology**, n. 14, p. 429-465, 1973. https://doi.org/10.1093/petrology/14.3.429

EWART, A.; MILNER, S. C.; ARMSTRONG, R. A.; DUNCAN, A. R. Etendeka volcanism of the Goboboseb Mountains and Messum Igneous Complex, Namibia. **Journal of Petrology**, n. 39(2), p. 191–225, 1998. https://doi.org/10.1093/petroj/39.2.191

FARIAS, F.; SZATMARI, P.; BAHNIUK, A.; FRANCA, A. B. Evaporitic carbonates in the pre-salt of Santos Basin – Genesis and tectonic implications. **Marine and Petroleum Geology**, n. 105, p. 251–272, 2019. https://doi.org/10.1016/j.marpetgeo.2019.04.020

FERNANDES, G.L.; SCHMITT, R.S.; BONGIOLO, E.; MENDES, J.C.; BASEI, M.A.S. Unraveling the tectonic evolution of a Neoproterozoic-Cambrian active margin in the Ribeira Orogen (SE Brazil): U-Pb and Lu-Hf provenance data. **Precambrian Research**, n. 266, p. 337-360, 2015. https://doi.org/10.1016/j.precamres.2015.05.017

FERRONI, F.; MELLO, C.; DESTRO, N. Tectonic control on the Cabo Frio anorogenic magmatic lineament, Southeastern Brazil. **Journal of South American Earth Sciences**, n. 83, p. 37-54, 2018. https://doi.org/10.1016/j.jsames.2017.11.001

FLECK, R. J.; SUTTER, J. F.; ELLIOT, D. H. Interpretation of discordant 40Ar/39Ar age-spectra of Mesozoic tholeiites from Antarctica. **Geochimica et Cosmochimica Acta**, n. 41, p. 15–32, 1977. https://doi.org/10.1016/0016-7037(77)90184-3

FLORISBAL, L. M.; HEAMAN, L. M.; JANASI, V. A.; BITENCOURT, M. F. Tectonic significance of the Florianopolis Dyke Swarm, Parana-Etendeka Magmatic Province: a reappraisal based on precise U-Pb dating. **Journal of Volcanology and Geothermal Research**, n. 289, p. 140–150, 2014. https://doi.org/10.1016/j.jvolgeores.2014.11.007

FOLEY, S.; BARTH, M.; JENNER, G. Rutile/melt Partition Coefficients for Trace Elements and an Assessment of the Influence of Rutile on the Trace Element Characteristics of Subduction Zone Magmas. **Geochimica et Cosmochimica Acta**, n. 64, p. 933-938, 2000. https://doi.org/10.1016/S0016-7037(99)00355-5

FRANKE, D. Rifting, lithosphere breakup and volcanism: Comparison of magma-poor and volcanic rifted margins. **Marine and Petroleum Geology**, n. 43, p. 63-87, 2013. https://doi.org/10.1016/j.marpetgeo.2012.11.003

FROST, B. R. Introduction to oxygen fugacity and its petrologic importance. In: LINDSLEY, D.H. (Ed.), **Oxide Minerals: Petrologic and Magnetic Significance**, Berlin, Boston: De Gruyter, 1991. https://doi.org/10.1515/9781501508684-004

FUJIMAKI, H.; TATSUMOTO, M.; AOKI, K. Partition coefficients of Hf, Zr, and REE between phenocrysts and groundmasses. **Journal of Geophysical Research – Solid Earth**, n. 89, p. 662-672, 1984. https://doi.org/10.1029/JB089iS02p0B662

GAETANI, G. The influence of melt structure on trace element partitioning near the peridotite solidus. **Contributions to Mineralogy and Petrology**, n. 147, p. 511-527, 2004. https://doi.org/10.1007/s00410-004-0575-1

GALE, A.; DALTON, C.; LANGMUIR, C.; SU, Y.; SCHILLING, J. The mean composition of ocean ridge basalts. **Geochemistry, Geophysics, Geosystems**, n. 14, p. 489-518, 2013. https://doi.org/10.1029/2012GC004334

GALLACHER, R.; KEIR, D.; HARMON, N. The nature of upper mantle upwelling during initiation of seafloor spreading in the southern Red Sea. In: RASUL, N.; STEWART, I. (Eds.), **Geological Setting, Palaeoenvironment and Archaeology of the Red Sea**, Springer, p. 113-129, 2019. http://doi.org/10.1007/978-3-319-99408-6_6

GILL, R. **Igneous rocks and processes – A practical guide**. UK: Wiley-Blackwell, 1944. http://doir.orb/10.2307/40929624

GILLARD, M.; MANATSCHAL, G.; AUTIN, J. How can asymmetric detachment faults generate symmetric Ocean Continent Transitions? **Terra Nova**, n. 28, p. 27–34, 2016. https://doi.org/10.1111/ter.12183

GILLARD, M.; SAUTER, D.; TUGEND, J.; TOMASI, S.; EPIN, M.; MANATSCHAL, G. Birth of an oceanic spreading center at a magma-poor rift system. **Scientific Reports**, n. 7, p. 15072, 2017. https://doi.org/10.1038/s41598-017-15522-2

GÖĞÜŞ, O. H.; PYSKLYWEC, R. N.; CORBI, F.; FACCENNA, C. The surface tectonics of mantle lithosphere delamination following ocean lithosphere subduction: Insights from physical-scaled analogue experiments. **Geochemistry, Geophysics, Geosystems**, n. 12, p. Q05004, 2011. http://doi.org.10.1029/2010GC003430

GOMES, C. B.; AZZONE, R. G.; RUBERTI, E.; VASCONCELOS, P. M.; SATO, K.; ROJAS, G. E. E. New age determinations for the Banhadão and Itapirapuã complexes in the Ribeira Valley, southern Brazil. **Brazilian Journal of Geology**, n. 48(2), p. 403–414, 2018. https://doi.org/10.1590/2317-4889201820170094

GOMES, A.; VASCONCELOS, P. Geochronology of the Paraná-Etendeka large igneous province. **Earth-Science Reviews**, n. 220, p. 103716, 2021. https://doi.org/10.1016/j.earscirev.2021.103716

GRANOT, R.; DYMENT, J. The Cretaceous opening of the South Atlantic Ocean. **Earth and Planetary Science Letters**, n. 414, p. 156-163, 2015. https://doi.org/10.1016/j.epsl.2015.01.015

GREEN, T.; BLUNDY, J.; ADAM, J.; YAXLEY, G. SIMS determination of trace element partition coefficients between garnet, clinopyroxene and hydrous basaltic liquids at 2-7.5 Gpa and 1080-1200C. **Lithos**, n. 53, p. 165-187, 2000. https://doi.org/10.1016/S0024-4937(00)00023-2

GUALDA, G.A.R.; GHIORSO, M.S.; LEMONS, R. V.; CARLEY, T.L. Rhyolite-MELTS: a Modified Calibration of MELTS Optimized for Silica-rich, Fluid-bearing Magmatic Systems. **Journal of Petrology**, n. 53(5), p. 875–890, 2012. https://doi.org/10.1093/petrology/egr080

GUALDA, G. A. R.; GHIORSO, M.S. MELTS_Excel: A Microsoft Excel-based MELTS interface for research and teaching of magma properties and evolution. **Geochemistry, Geophysics, Geosystems**, n. 16, p. 315–324, 2015. http://doi.org/10.1002/2014GC005545

GUEDES, E.; HEILBRON, M.; VASCONCELOS, P. M.; DE MORISSON VALERIANO, C.; HORTA DE ALMEIDA, J. C.; TEIXEIRA, W.; FILHO, A. T. K-Ar and 40Ar/39Ar ages of dikes emplaced in the onshore basement of the Santos Basin, Resende area, SE Brazil: Implications for the south Atlantic opening and Tertiary reactivation. **Journal of South American Earth Sciences**, n. 18, p. 371–382, 2005. https://doi.org/10.1016/j.jsames.2004.11.008

GUEDES, E.; HEILBRON, M.; MORISSON VALERIANO, C.; ALMEIDA, J. C. H.; SZATMARI, P. Evidence of Gondwana early rifting process recorded by Resende-Ilha Grande Dike Swarm, southern Rio de Janeiro, Brazil. **Journal of South American Earth Sciences**, n. 67, p. 11–24, 2016. https://doi.org/10.1016/j.jsames.2016.01.004

HEILBRON, M.; DUARTE, B.P.; VALERIANO, C.M.; SIMONETTI, A.; MACHADO, N.; NOGUEIRA, J.R. Evolution of reworked Paleoproterozoic basement rocks within the Ribeira belt (Neoproterozoic), SE-Brazil, based on U–Pb geochronology: Implications for paleogeographic reconstructions of the São Francisco-Congo paleocontinent. **Precambrian Research**, n. 178, p. 136-148, 2010. https://doi.org/10.1016/j.precamres.2010.02.002

HENDERSON, P. General geochemical properties and abundances of the rare earth elements. In: HENDERSON, P. (Ed.), **Rare earth element geochemistry**, Amsterdam: Elsevier, p. 1-32, 1984. https://doi.org/10.1016/B978-0-444-42148-7.50006-X

HOFMANN, A.; JOCHUM, K.; SEUFERT, M.; WHITE, W. Nb and Pb in oceanic basalts: new constraints on mantle evolution. **Earth and Planetary Science Letters**, n. 79, p. 33-45, 1986. https://doi.org/10.1016/0012-821X(86)90038-5

HONJO, N.; LEEMAN, W.P. Origin of hybrid ferrolatite lavas from Magic Reservoir Eruptive, Snake River Plain, Idaho. **Contributions to Mineralogy and Petrology**, n. 96, p. 163-177, 1987. https://doi.org/10.1007/BF00375230

IRVINE, T.N.; BARAGAR, W.R.A. A Guide to the Chemical Classification of the Common Volcanic Rocks. **Canadian Journal of Earth Sciences**, n. 8(5), p. 523-548, 1971. https://doi.org/10.1139/e71-055

JAGOUTZ, O.; MÜNTENER, O.; MANATSCHAL, G.; RUBATTO, D.; PÉRON-PINVIDIC, G.; TURRIN, B.D.; VILLA, I.M. The rift-to-drift transition in the North Atlantic: A stuttering start of the MORB machine? **Geology**, n. 35(12), p. 1087–1090, 2007. https://doi.org/10.1130/G23613A.1

JOHNSON, A.; SCHWAB, B. Constraints on clinopyroxene/melt partitioning REE, Rb, Sr, Ti, Cr, Zr, and Nb during mantle melting: First insights from direct peridotite melting experiments at 1.0 GPa. **Geochimica et Cosmochimica Acta**, n. 68(23), p. 4949-4962, 2004. https://doi.org/10.1016/j.gca.2004.06.009

JOURDAN, F.; FÉRAUD, G.; BERTRAND, H.; WATKEYS, M. From flood basalts to the inception of oceanization: Example from the 40Ar/39Ar high-resolution picture of the Karoo large igneous province. **Geochemistry, Geophysics, Geosystems**, n. 80, p. Q02002, 2007. https://doi.org/10.1029/2006GC001392

KATO, T.; RINGWOOD, A.E.; IRIFUNE, T. Experimental-Determination of Element Partitioning between Silicate Pervoskites, Garnets and Liquids - Constraints on Early Differentiation of the Mantle. **Earth and Planetary Science Letters**, n. 89(1), p. 123-145, 1988. https://doi.org/10.1016/0012-821X(88)90038-6

KELEMEN, P.; HANGHØJ, K.; GREENE, A. One View of the Geochemistry of Subduction-Related Magmatic Arcs, with an Emphasis on Primitive Andesite and Lower Crust. In: TUREKIAN, K.; HOLLAND, H. (Eds.), **Treatise on Geochemistry**, n. 3, p. 593-659, Elsevier, 2003. http://doi.org/10.1016/B0-08-043751-6/03035-8

KEMPE, U.; SELTMANN, R.; GRAUPNER, T.; RODIONOV, N.; SERGEEV, S. A.; MATUKOV, D. I.; KREMENETSKY, A. A. Concordant UPb SHRIMP ages of U-rich zircon in granitoids from the Muruntau gold district (Uzbekistan): Timing of intrusion, alteration ages, or meaningless numbers. **Ore Geology Reviews**, n. 65(1), p. 308–326, 2015. http://doi.org/10.1016/j.oregeorev.2014.10.007

KINZLER, R.J. Melting of mantle peridotite at pressure approaching the spinel to garnet transition: application to mid-ocean ridge petrogenesis. **Journal of Geophysical. Research – Solid Earth**, n. 102, p. 853– 874, 1997. https://doi.org/10.1029/96JB00988

KIRKPATRICK, R. J. Nucleation and growth of plagioclase, Makaopuhi and Alae lava lakes, Kilauea Volcano, Hawaii. **The Geological Society of America Bulletin**, n. 88, p. 78–84, 1977. https://doi.org/10.1130/0016-7606(1977)88<78:NAGOPM>2.0.CO;2

KUIPER, K. F.; DEINO, A.; HILGEN, F. J.; KRIJGSMAN, W.; RENNE, P. R.; WIJBRANS, J. B. Synchronizing rock clocks of Earth history. **Science**, n. 320, p. 500–504, 2008. http://doi.org/10.1126/science.1154339

LAVECCHIA, A.; CLARK, S. R.; BEEKMAN, F.; CLOETINGH, S. A. P. L.; BUROV, E. Thermal perturbation, mineral assemblages, and rheology variations induced by dyke emplacement in the crust. **Tectonics**, n. 35, p. 1137–1152, 2016. https://doi.org/10.1002/2016TC004125

LAWRENCE, D.H. They Say the sea is loveless. In: PINTO, V.S.; ROBERTS, W. (Eds.), **The complete poems**, Penguin Books, 1977.

LE BAS, M.J.; LE MAITRE, R.W.; STRECKEISEN, A.; ZANETTIN, B. A chemical classification of volcanic rocks based on the totalalkali–silica diagram. **Journal of Petrology**, n. 27, p. 745–750, 1986. https://doi.org/10.1093/petrology/27.3.745

LEE, J.-Y.; MARTI, K.; SEVERINGHAUS, J. P.; KAWAMURA, K.; YOO, H.-S.; LEE, J. B.; KIM J. S. A redetermination of the isotopic abundances of atmospheric Ar. **Geochimica**

et Cosmochimica Acta, n. 70, p. 4507–4512, 2006. https://doi.org/10.1016/j.gca.2006.06.1563

LE MAITRE, R.; STRECKEISEN, A.; ZANETTIN, B.; LE BAS, M.; BONIN, B.; BATEMAN, P. **Igneous Rocks: A Classification and Glossary of Terms: Recommendations of the International Union of Geological Sciences Subcommission on the Systematics of Igneous Rocks.** Cambridge: Cambridge University Press, 2002. https://doi.org/10.1017/CBO9780511535581

LI, Z.-H.; LIU, M.; GERYA, T. Lithosphere delamination in continental collisional orogens: A systematic numerical study. **Journal of Geophysical Research – Solid Earth**, n. 121, p. 5186–5211, 2016. http://doi.org/10.1002/2016JB013106

LIGI, M.; BONATTI, E.; BORTOLUZZI, G.; CIPRIANI, A.; COCCHI, L.; CARATORI TONTINI, F.; CARMINATI, E.; OTTOLINI, L.; SCHETTINO, A. Birth of an ocean in the Red Sea: Initial pangs. **Geochemistry, Geophysics, Geosystems**, n. 13, p. Q08009, 2012. https://doi.org/10.1029/2012GC004155

LIGI, M.; BONATTI, E.; BOSWORTH, W.; CAI, Y.; CIPRIANI, A.; PALMIOTTO, C.; RONCA, S.; SEYLER, M. Birth of an ocean in the Red Sea: Oceanic-type basaltic melt intrusions precede continental rupture. **Gondwana Research**, n. 54, p. 150-160, 2018. https://doi.org/10.1016/j.gr.2017.11.002

LIGI, M.; BONATTI, E.; BOSWORTH, W.R.; RONCA, S. Oceanization Starts at Depth During Continental Rupturing in the Northern Red Sea. In. RASUL, N.; STEWART, I. (Eds.), **Geological Setting, Palaeoenvironment and Archaeology of the Red Sea**, p. 131-158, Springer, 2019. http://doi.org/10.1007/978-3-319-99408-6_7

LIMA, B. E. M.; TEDESCHI, L. R.; PESTILHO, A. L. S.; SANTOS, R. V.; VAZQUEZ, J. C.; GUZZO, J. V. P.; DE ROS, L. F. Deep burial hydrothermal alteration of the Pre-Salt carbonate reservoirs from northern Campos Basin, offshore Brazil: Evidence from petrography, fluid inclusions, Sr, C and O isotopes. **Marine and Petroleum Geology**, n. 113, p. 104143, 2020. https://doi.org/10.1016/j.marpetgeo.2019.104143

LUHR, J.F.; CARMICHAEL, S.E. The Colima Volcanic Complex, Mexico. **Contributions to Mineralogy and Petrology**, n. 71, p. 343-372, 1980. https://doi.org/10.1007/BF00374707

LUTTINEN, A.V.; HEINONEN, J.S.; KURHILA, M.; JOURDAN, F.; MÄNTTÄRI, I.; VUORI, S.K.; HUHMA, H. Depleted Mantle-sourced CFB Magmatism in the Jurassic Africa–Antarctica Rift: Petrology and ^{40}Ar/^{39}Ar and U/Pb Chronology of the Vestfjella Dyke Swarm, Dronning Maud Land, Antarctica. **Journal of Petrology**, n. 56(5), p. 919–952, 2015. https://doi.org/10.1093/petrology/egv022

MACHADO, F. B.; ROCHA-JÚNIOR, E. R. V.; MARQUES, L. S.; NARDY, A. J. R. Volcanological aspects of the northwest region of Paraná continental flood basalts (Brazil). **Solid Earth**, n. 6, p. 227–241, 2015. http://doi.org/10.5194/se-6-227-2015

MAGEE, C.; PICHEL, L. M.; MADDEN-NADEAU, A. L.; JACKSON, C.-A.-L.; MOHRIAK, W. Salt–magma interactions influence intrusion distribution and salt tectonics in the Santos Basin, offshore Brazil. **Basin Research**, n. 33, p. 1820– 1843, 2021. https://doi.org/10.1111/bre.12537

MAGNI, V.; FACCENNA, C.; VAN HUNEN, J.; FUNICIELLO, F. Delamination vs. break-off: the fate of continental collision. **Geophysical Research Letters**, n. 40, p. 285– 289, 2013. http://doi.org/10.1002/grl.50090

MARQUES, L. S.; DUPRE, B.; PICCIRILLO, E. M. Mantle source compositions of the Paraná Magmatic Province: evidence from trace element and Sr-Nd-Pb isotope geochemistry. **Journal of Geodynamics**, n. 28, p. 439–459, 1999. https://doi.org/10.1016/S0264-3707(99)00020-4

MARQUES, L. S.; ROCHA-JÚNIOR, E. R. V.; BABINSKI, M.; CARVAS, K. Z.C.; PETRONILHO, L. A.; DE MIN, A. Lead isotope constraints on the mantle sources involved in the genesis of Mesozoic high-Ti tholeiite dykes (Urubici type) from the São Francisco Craton (Southern Espinhaço, Brazil). **Brazilian Journal of Geology**, n. 46(1), p. 105–122, 2016. https://doi.org/10.1590/2317-4889201620150010

MARQUES, L. S.; DEMIN, A.; ROCHA-JÚNIOR, E. R. V.; BABINSKI, M.; BELLIENI, G.; FIGUEIREDO, A. M. G. Elemental and Sr-Nd-Pb isotope geochemistry of the Florianópolis Dyke Swarm (Paraná Magmatic Province): crustal contamination and mantle source constraints. **Journal of Volcanology Research**, n. 355, p. 149–164, 2018. https://doi.org/10.1016/j.jvolgeores.2017.07.005

MARZOLI, A.; MELLUSO, L.; MORRA, V.; RENNE, P.; SGROSSO, I.; D'ANTONIO, M.; DUARTE MORAIS, L.; MORAIS, E.A.A.; RICCI, G. Geochronology and petrology of cretaceous basaltic magmatism in the Kwanza basin (Western Angola), and relationships with the Parana-Etendeka continental flood basalt province. **Journal of Geodynamics**, n. 28, p. 341–356, 1999. https://doi.org/10.1016/S0264-3707(99)00014-9

MCDONOUGH, W. F.; SUN, S. The composition of the Earth. **Chemical Geology**, n. 120, p. 223–253, 1995. https://doi.org/10.1016/0009-2541(94)00140-4

MCDOUGALL, I.; HARRISON, T. M. **Geochronology and Thermochronology by the 40Ar/39Ar method.** England: Oxford University Press, 1999. https://doi.org/10.1093/petrology/41.12.1823

MCKENZIE, D. Some remarks on the development of sedimentary basins. **Earth and Planetary Science Letters**, n. 40(1), p. 25-32, 1978. https://doi.org/10.1016/0012-821X(78)90071-7

MCKENZIE, D.; O'NIONS, R.K. Partial melt distributions from inversion of rare Earth element concentrations. **Journal of Petrology**, n. 32, p. 1021-1091, 1991. https://doi.org/10.1093/petrology/32.5.1021

MOLLO, S.; HAMMER, J. Dynamic crystallization in magmas. **EMU Notes in Mineralogy**, n. 16, p. 373–418, 2017. http://doi.org/10.1180/EMU-notes.16.12

MONTES-LAUAR, C. R.; PACCA, I. G.; MELFI, A. J.; KAWASHITA, K. Late Cretaceous alkaline complexes, southeastern Brazil: Paleomagnetism and geochronology. **Earth and Planetary Science Letters**, n. 134(3–4), p. 425–440, 1995. https://doi.org/10.1016/0012-821X(95)00135-Y

MORIMOTO, N. Nomenclature of Pyroxenes. **Mineralogy and Petrology**, n. 39, p. 55–76, 1988. https://doi.org/10.1007/BF01226262 https://doi.org/10.1007/BF01226262

MILANI, E.; FILHO, A. Sedimentary basins of South America. In: CORDANI, U.G.; MILANI, E.J.; THOMAZ FILHO, A.; CAMPOS, D. A. (Eds.), **Tectonic evolution of South America**, International Geological Congress, n. 31, p. 389–449, 2000. http://dx.doi.org/10.4067/S0716-02082000000200006

MIZUSAKI, A. M. P.; PETRINI, R.; BELLIENI, G.; COMIN-CHIARAMONTI, P.; DIAS, J.; DE MIN, A.; PICCIRILLO, E. M. Basalt magmatism along the passive continental margin of SE Brazil (Campos Basin). **Contributions to Mineralogy and Petrology**, n. 111, p. 143–160, 1992. https://doi.org/10.1007/BF00348948

NARDY, A. J. R.; OLIVEIRA, M. A. F.; FIGUEIREDO, A. M. Geoquímica das Rochas Vulcânicas Ácidas Mesozóicas da Região Central da Bacia do Paraná. **V Simpósio de Geologia do S.E.**, p. 65–67, 1997.

NEAVE, D. A.; PUTIRKA, K. D. A new clinopyroxene-liquid barometer, and implications for magma storage pressures under Icelandic rift zones. **American Mineralogist**, n. 102, p. 777–794, 2017. https://doi.org/10.2138/am-2017-5968

NEGREDO, A.M.; MANCILLA, F.D.L.; CLEMENTE, C.; MORALES, J.; FULLEA, J. Geodynamic Modeling of Edge-Delamination Driven by Subduction-Transform Edge Propagator Faults: The Westernmost Mediterranean Margin (Central Betic Orogen) Case Study. **Frontiers in Earth Science**, n. 8, p. 533392, 2020. http://doi.org/10.3389/feart.2020.533392

NIU, Y. Lithosphere thickness controls the extent of mantle melting, depth of melt extraction and basalt compositions in all tectonic settings on Earth – A review and new perspectives. **Earth-Science Reviews**, n. 217, p. 103614, 2021. https://doi.org/10.1016/j.earscirev.2021.103614

OREIRO, S. G.; CUPERTINO, J. A.; SZATMARI, P.; FILHO, A. T. Influence of pre-salt alignments in post-Aptian magmatism in the Cabo Frio High and its surroundings, Santos and Campos basins, SE Brazil: An example of non-plume-related magmatism. **Journal of South American Earth Sciences**, n. 25(1), p. 116–131, 2008. https://doi.org/10.1016/j.jsames.2007.08.006

PATON, C.; HELLSTROM, J.; PAUL, B.; WOODHEAD, J.; HERGT, J. Iolite: freeware for the visualisation and processing of mass spectrometric data. **Journal of Analytical Atomic Spectrometry**, n. 26(12), p. 2508–2518, 2011. https://doi.org/10.1039/C1JA10172B

PEARCE, J.A. A user’s guide to basalt discrimination diagrams. In: WYMAN, D.A. (Ed), **Trace element geochemistry of volcanic rocks: applications for massive sulfide exploration: Geological Association of Canada, Short Course Notes**, n. 12, p. 79–113, 1996.

PEARCE, J.; ERNST, R.; PEATE, D.; ROGERS, C. LIP printing: Use of immobile element proxies to characterize Large Igneous Provinces in the geologic record. **Lithos**, n. 392-393, p. 106068, 2021. https://doi.org/10.1016/j.lithos.2021.106068

PEATE, D. W.; HAWKESWORTH, C. J.; MANTOVANI, M. S. M. Chemical stratigraphy of the Paraná lavas, South America: classification of magma types and their spatial distribution. **Bulletin of Volcanology**, n. 55, p. 119–139, 1992. https://doi.org/10.1007/BF00301125

PEATE, D.W. The Paraná-Etendeka Province. In: MAHONEY, J.J.; COFFIN, M. (Eds.), **Large Igneous Provinces**, Geophysical Monography Series, American Geophysical Union, n. 100, p. 217–245, 1997. https://doi.org/10.1029/GM100p0217

PEIXOTO, C.; HEILBRON, M.; RAGATKY, D.; ARMSTRONG, R.; DANTAS, E.; VALERIANO, C.; SIMONETTI, A. Tectonic evolution of the Juvenile Tonian Serra da Prata magmatic arc in the Ribeira belt, SE Brazil: Implications for early west Gondwana amalgamation. **Precambrian Research**, n. 302, p. 221-254, 2017. https://doi.org/10.1016/j.precamres.2017.09.017

PERON-PINVIDIC, G.; MANATSCHAL, G.; THE "IMAGINING RIFTING" WORKSHOP PARTICIPANT. Rifted Margins: State of the Art and Future Challenges. **Frontiers in Earth Sciences**, n. 7, p. 218, 2019. http://doi.org/10.3389/feart.2019.00218

PESSOA, F. Qualquer caminho leva a toda parte. In: LOPES, T.R. (Ed.), **Pessoa por conhecer – Textos para um novo mapa**, Lisboa, Estampa, 1990.

PETRUS, J. A.; CHEW, D. M.; LEYBOURNE, M. I.; KAMBER, B. S. A new approach to laser-ablation inductively-coupledplasma mass spectrometry (LA-ICP-MS) using the flexible map interrogation tool 'Monocle'. **Chemical Geology**, n. 463, p. 76–93, 2017. https://doi.org/10.1016/j.chemgeo.2017.04.027

PICCIRILLO, E. M.; MELFI, A. J. **The Mesozoic flood volcanism of the Paraná Basin: petrogenetic and geophysical aspects**, São Paulo: Universidade de São Paulo, Instituto Astronômico e Geofísico, 1988.

PUTIRKA, K. D.; JOHNSON, M.; KINZLER, R. J.; LONGHI, J.; WALKER, D. Thermobarometry of mafic igneous rocks based on clinopyroxene-liquid equilibria, 0–30 kbar. **Contributions to Mineralogy and Petrology**, n. 123, p. 92–108, 1996. https://doi.org/10.1007/s004100050145

PUTIRKA, K. Clinopyroxene + liquid equilibria to 100 kbar and 2450 K. **Contributions to Mineralogy and Petrology**, n. 135, p. 151–163, 1999. https://doi.org/10.1007/s004100050503

PUTIRKA, K. D. Thermometers and barometers for volcanic systems. **Reviews in Mineralogy and Geochemistry**, n. 69, p. 61–120, 2008. https://doi.org/10.2138/rmg.2008.69.3

RAPOSO, M. I. B.; ERNESTO, M.; RENNE, P. R. Paleomagnetism and 40Ar/39Ar dating of the Early Cretaceous Florianópolis dike swarm (Santa Catarina Island), Southern Brazil. **Physics of the Earth and Planetary Interiors**, n. 108, p. 275–290, 1998. https://doi.org/10.1016/S0031-9201(98)00102-2

REN Z.; VASCONCELOS, P. M. Argon diffusion in hypogene and supergene alunites: implications to geochronology and thermochronometry on Earth and Mars. **Geochimica et Cosmochimica Acta**, n. 262, p. 166–187, 2019. https://doi.org/10.1016/j.gca.2019.07.014

RENNE, P. R.; MERTZ, D. F.; ERNESTO, M.; MARQUES, L. S.; TEIXEIRA, W.; ENS, H. H.; RICHARDS, M. A. Geochronologic constraints on magmatic and tectonic evolution of the Paraná Province. **EOS AGU**, n. 26, p. 553, 1993.

https://repositorio.usp.br/directbitstream/8588701b-d0c9-44ab-a1b1-b13a97f5e835/0858409.pdf

RENNE, P. R.; GLEN, J. M.; MILNER, S. C.; DUNCAN, A. R. Age of Etendeka flood volcanism and associated intrusions in southwestern Africa. **Geology**, n. 24, p. 659–662, 1996. https://doi.org/10.1130/0091-7613(1996)024<0659:AOEFVA>2.3.CO;2

RENNE, P. R.; SWISHER, C. C.; DEINO, A. L.; KARNER, D. B.; OWENS, T. L.; DE PAOLO, D. J. Intercalibration of standards, absolute ages and uncertainties in 40Ar/39Ar dating. Chem. **Geology**, n. 145, p. 117–152, 1998. https://doi.org/10.1016/S0009-2541(97)00159-9

RIVALTA, E.; TAISNE, B.; BUNGER, A. P.; KATZ, R. F. A review of mechanical models of dike propagation: Schools of thought, results and future directions. **Tectonophysics**, n. 638, p. 1-42, 2015. https://doi.org/10.1016/j.tecto.2014.10.003

ROCHA-JÚNIOR, E. R. V.; MARQUES, L. S.; BABINSKI, M.; NARDY, A. J. R.; FIGUEIREDO, A. M. G.; MACHADO, F. B. Sr-Nd-Pb isotopic constraints on the nature of the mantle sources involved in the genesis of the high-Ti tholeiites from Northern Paraná Continental Flood Basalts (Brazil). **Journal of South American Earth Sciences**, n. 46, p. 9–25, 2013. https://doi.org/10.1016/j.jsames.2013.04.004

ROCHA-JÚNIOR, E. R. V.; MARQUES, L. S.; BABINSKI, M.; MACHADO, F.B.; PETRONILHO, L. A.; NARDY, A. J. R. A telltale signature of Archean lithospheric mantle in the Paraná continental flood basalts genesis. **Lithos**, n. 364–365, p. 105519, 2020. https://doi.org/10.1016/j.lithos.2020.105519

SALTERS, V.; LONGHI, J. Trace element partitioning during the initial stages of melting beneath mid-ocean ridges. **Earth and Planetary Science Letters**, n. 166, p. 15-30, 1999. https://doi.org/10.1016/S0012-821X(98)00271-4

SALTERS, V.J.M.; STRACKE, A. Composition of the depleted mantle. **Geochemistry, Geophysics, Geosystems**, n. 5, p. Q05B07, 2004. https://doi.org/10.1029/2003GC000597

SANFILIPPO, A.; CAI, Y.; JÁCOME, A.P.G.; LIGI, M. Geochemistry of the Lunayyir and Khaybar Volcanic Fields (Saudi Arabia): Insights into the Origin of Cenozoic Arabian Volcanism. In: RASUL, N.; STEWART, I. (Eds.), **Geological Setting, Palaeoenvironment and Archaeology of the Red Sea**, p. 113-129, Springer, 2019. https://doi.org/10.1007/978-3-319-99408-6_18

SAPIN, F.; RINGENBACH, J.C.; CLERC, C. Rifted margins classification and forcing parameters. **Scientific Reports**, n. 11, p. 8199, 2021. https://doi.org/10.1038/s41598-021-87648-3

SAVASTANO, V.L.M.; SCHMITT, R.S.; ARAÚJO, M.N.C.; INOCÊNCIO, L.C. Rift brittle deformation of SE-Brazilian continental margin: Kinematic analysis of onshore structures relative to the transfer and accommodation zones of southern Campos Basin. **Journal of Structural Geology**, n. 94, p. 136-153, 2017. https://doi.org/10.1016/j.jsg.2016.11.012

SCHAEN, A.J.; JICHA, B.R.; HODGES, K.V.; VERMEESCH, P.; STELTEN, M.E.; MERCER, C.M.; PHILLIPS, D.; RIVERA, T.A.; JOURDAN, F.; MATCHAN, E.L.; HEMMING, S.R.; MORGAN, L.E.; KELLEY, S.P.; CASSATA, W.S.; HEIZLER, M.T.; VASCONCELOS, P.M.; BENOWITZ, J.A.; KOPPERS, A.A.P.; MARK, D.F.; NIESPOLO,

E.M.; SPRAIN, C.J.; HAMES, W.E.; KUIPER, K.F.; TURRIN, B.D.; RENNE, P.R.; ROSS, J.; NOMADE, S.; GUILLOU, H.; WEBB, L.E.; COHEN, B.A.; CALVERT, A.T.; JOYCE, N.; GANERØD, M.; WIJBRANS, J.; ISHIZUKA, O.; HE, H.; RAMIREZ, A.; PFÄNDER, J.A.; LOPEZ-MARTÍNEZ, M.; QIU, H.; SINGER, B.S. Interpreting and reporting 40Ar/39Ar geochronologic data. **GSA Bulletin**, n. 133(3–4), p. 461–487, 2020. https://doi.org/10.1130/B35560.1

SCHMITT, R. S.; TROUW, R. A. J.; VAN SCHUMUS, W. R.; PIMENTEL, M. M. Late amalgamation in the central part of West Gondwana: new geochronological data and the characterization of a Cambrian collisional orogeny in the Ribeira Belt (SE Brazil). **Precambrian Research**, n. 113, p. 29–61, 2004. http://doi.org/10.1016/j.precamres.2004.03.010

SCHMITT, R.S.; TROUW, R.A.J.; MEDEIROS, S.R.; DANTAS, E.L. Age and geotectonic setting of Late-Neoproterozoic juvenile mafic gneisses and associated paragneisses from the Ribeira Belt (SE Brazil): geochemistry and Sm-Nd data - implications on Gondwana assembly. **Gondwana Research**, n. 13, p. 502-515, 2008. https://doi.org/10.1016/j.gr.2007.05.015

SCHMITT, R. S.; TROUW, R.; VAN SCHMUS, W. R.; ARMSTRONG, R.; STANTON, N. S. G. The tectonic significance of the Cabo Frio Tectonic Domain in the SE Brazilian margin: a Paleoproterozoic through Cretaceous saga of a reworked continental margin. **Brazilian Journal of Geology**, n. 46(1), p. 37–66, 2016. http://doi.org/10.1590/2317-4889201620150025

SCHOCK, H.H. Trace-element partitioning between phenocrysts of plagioclase, pyroxenes and magnetite and host pyroclastic matrix. **Journal of Radioanalytical Chemistry**, n. 38(1-2), p. 327-340, 1977. https://doi.org/10.1007/BF02520210

SHARP, D. W.; RENNE P. R. The 40Ar/39Ar dating of core recovered by the Hawaii Scientific Drilling Project (phase 2), Hilo, Hawaii. **Geochemistry, Geophysics, Geosystems**, n. 6(4), p. Q04G17, 2005. https://doi.org/10.1029/2004GC000846

SILVA, R. M.; SACEK, V. Shallow necking depth and differential denudation linked to post-rift continental reactivation: The origin of the Cenozoic basins in southeastern Brazil. **Terra Nova**, n. 31(6), p. 527–533, 2019. http://doi.org/10.1111/ter.12423

SILVA, R.M.; SACEK, V. Influence of Surface Processes on Postrift Faulting During Divergent Margins Evolution. **Tectonics**, n. 41, p. e2021TC006808, 2022. https://doi.org/10.1029/2021TC006808

SMITH, P. M.; ASIMOW, P.D. Adiabat_1ph: A new public front-end to the MELTS, pMELTS, and pHMELTS models. **Geochemistry, Geophysics, Geosystems**, n. 6, p. Q02004, 2005. http://doi.org/10.1029/2004GC000816

SOBOLEV, A.V.; HOFMANN, A.W.; SOBOLEV, S.V.; NIKOGOSIAN, I.K. An olivine-free mantle source of Hawaiian shield basalts. **Nature**, n. 434(7033), p. 590-7, 2005. https://doi.org/10.1038/nature03411

SOBOLEV, AL.; HOFMANN, A.; KUZMIN, D.; YAXLEY, G.; ARNDT, N.; CHUNG, S.; DANYUSHEVSKY, L.; ELLIOTT, T.; FREY, F.; GARCIA, M.; GURENKO, A.; KAMENETSKY, V.; KERR, A.; KRIVOLUTSKAYA, N.; MATVIENKOV, V.; NIKOGOSIAN, I.; ROCHOLL, A.; SIGURDSSON, I.; SUSHCHEVSKAYA, N.; TEKLAY,

M. The Amount of Recycled Crust in Sources of Mantle-Derived Melts. **Science**, n. 316, p. 412-417, 2007. http://doir.org/10.1126/science.1138113

SPELL, T. L.; MCDOUGALL, I. Characterization and calibration of 40Ar/39Ar dating standards. **Chemical Geology**, n. 198, p. 189–211, 2003. https://doi.org/10.1016/S0009-2541(03)00005-6

STANTON, N.; SCHMITT, R. S.; GALDEANO, A.; MAIA, M.; MANE M. Crustal Structure of the Southeastern Brazilian Margin, Campos Basin, from Aeromagnetic Data: New kinematic constraints. **Tectonophysics**, n. 490, p. 15–27, 2010. https://doi.org/10.1016/j.tecto.2010.04.008

STORMER, J.C., & NICHOLLS, J. (1978). XLFRAC: a program for the interactive testing of magmatic differentiation models. *Computers &. Geosciences*, 4(2), 143-159. https://doi.org/10.1016/0098-3004(78)90083-3

THIEDE, D. S.; VASCONCELOS P. M. Parana flood basalts: Rapid extrusion hypothesis confirmed by new 40Ar/39Ar results. **Geology**, n. 38(8), p. 747–750, 2010. https://doi.org/10.1130/G30919.1

THOMPSON, R. N.; GIBSON, S. A.; MITCHELL, J. G.; DICKIN, A. P.; LEONARDOS, O. H.; BROD, J. A.; GRENNWOOD, J. C. Migrating Cretaceous-Eocene magmatism in the Serra do Mar Alkaline Province, SE Brazil: melts from the deflected Trindade mantle plume? **Journal of Petrology**, n. 39, p. 1493–1526, 1998. https://doi.org/10.1093/petroj/39.8.1493

THOMPSON, R. N.; GIBSON, S. A.; DICKIN, A. P.; SMITH P. M. Early Cretaceous basalt and picrite dykes of the southern Etendeka region, NW Namibia: windows to the role of the Tristan mantle plume in Paraná-Etendeka magmatism. **Journal of Petrology**, n. 11, p. 2049–2081, 2001. https://doi.org/10.1093/petrology/42.11.2049

THYBO, H.; NIELSEN, C. Magma-compensated crustal thinning in continental rift zones. **Nature**, n. 457, p. 873–876, 2009. https://doi.org/10.1038/nature07688

TORSVIK, T.H.; ROUSSE, S.; LABAILS, C.; SMETHURST, M.A. A new scheme for the opening of the South Atlantic Ocean and the dissection of an Aptian salt basin. **Geophysical Journal International**, n. 177, p. 1315-1333, 2009. https://doi.org/10.1111/j.1365-246X.2009.04137.x

TSYBULYAEV, S.V.; SAVKO, K.A.; SAMSONOV, A.V.; KORISH, E.H. Paleoproterozoic OIB- and MORB-Type Rift Volcanics of the Kursk Block, Eastern Sarmatia: Petrology and Geodynamics. **Petrology**, n. 29, p. 114–147, 2021. https://doi.org/10.1134/S0869591121020065

TURNER, S.; REGELOUS, M.; KELLEY, S.; HAWKESWORTH, C.; MANTOVANI, M. Magmatism and continental break-up in the South Atlantic: high precision 40Ar39Ar geochronology. **Earth and Planetary Science Letters**, n. 121, p. 333–348, 1994. https://doi.org/10.1016/0012-821X(94)90076-0

UBIDE, T.; MCKENNA, C. A.; CHEW, D. M.; KAMBER B. S. High-resolution LA-ICP-MS trace element mapping of igneous minerals: In search of magma histories. **Chemical Geology**, n. 409, p. 157–168, 2015. https://doi.org/10.1016/j.chemgeo.2015.05.020

UBIDE, T.; KAMBER, B.S. Volcanic crystals as time capsules of eruption history. **Nature Communications**, n. 9, p. 326, 2018. https://doi.org/10.1038/s41467-017-02274-w

UBIDE, T.; MOLLO, S.; ZHAO, J.; NAZZARI, M.; SCARLATO, P. Sector-zoned clinopyroxene as a recorder of magma history, eruption triggers, and ascent rates. **Geochimica et Cosmochimica Acta**, n. 251, p. 265–283, 2019a. https://doi.org/10.1016/j.gca.2019.02.021

UBIDE, T.; CAULFIELD, J.; BRANDT, C.; BUSSWEILER, Y.; MOLLO, S.; STEFANO, F.; NAZZARI, M.; SCARLATO, P. Deep Magma Storage Revealed by Multi-Method Elemental Mapping of Clinopyroxene Megacrysts at Stromboli Volcano. **Frontiers in Earth Science**, n. 7, p. 239, 2019b. https://doi.org/10.3389/feart.2019.00239

UBIDE, T.; NEAVE, D.A.; PETRELLI, M.; LONGPRÉ, M-A. Editorial: Crystal Archives of Magmatic Processes. **Frontiers in Earth Sciences**, n. 9, p. 749100, 2021. http://doi.org/10.3389/feart.2021.749100

URES, U.; BOSSI, J.; FÉRAUD, G.; BERTRAND, H. New Age and Geochemical Constraints on the Paraná Flood Volcanism: Additional Data on Uruguay Extrusive and Intrusive Formations. **AGU Fall meeting**, n. VI, p. E-11, 1997.

VASCONCELOS, P. M.; KNESEL, K. M.; COHEN, B. E.; HEIM, J. A. Geochronology of the Australian Cenozoic: a history of tectonic and igneous activity weathering, erosion, and sedimentation. **Australian Journal of Earth Sciences**, n. 55(6–7), p. 865–914, 2008. https://doi.org/10.1080/08120090802120120

VEIZER, J. Strontium isotopes in seawater through time. **Annual Review of Earth and Planetary Science**s, n. 17, p. 141–167, 1989. http://doi.org/10.1146/annurev.earth.17.1.141

VERATI, C.; JOURDAN, F. Modelling effect of sericitization of plagioclase on the 40 K/40Ar and 40 Ar/39 Ar chronometers: implication for dating basaltic rocks and mineral deposits. **Geological Society, London, Special Publications**, n. 378, p. 55–174, 2014. https://doi.org/10.1144/SP378.14

WALTER, M.J.. Melting of garnet peridotite and the origin of komatiite and depleted lithosphere. **Journal of Petrology**, n. 39, p. 29–60, 1998. https://doi.org/10.1093/petroj/39.1.29

WARREN, J. K. **Evaporites – A Geological Compendium.** Switzerland: Springer, 2016. https://doi.org/10.1007/978-3-319-13512-0

WERNICKE, B. Uniform-sense normal simple shear of the continental lithosphere. **Canadian Journal of Earth Sciences**, n. 22(1), p. 108-125, 1985. https://doi.org/10.1139/e85-009

WILSON, M. **Igneous Petrogenesis.** The Netherlands: Springer, 1989. https://doi.org/10.1007/978-94-010-9388-0

WINCHESTER, J.A.; FLOYD, P.A. Geochemical discrimination of different magma series and their differentiation products using immobile elements. **Chemical Geology**, n. 20, p. 325–343, 1977. https://doi.org/10.1016/0009-2541(77)90057-2

XU, Y.; MA, J.; FREY, F.; FEIGENSON, M.; LIU, J. Role of lithosphere-asthenosphere interaction in the genesis of Quaternary alkali and tholeiitic basalts from Datong, western

North China Craton. **Chemical Geology**, n. 224, p. 247-271, 2005. https://doi.org/10.1016/j.chemgeo.2005.08.004

ZACK, T.; FOLEY, S.F.; JENNER, G.A. A consistent partition coefficient set for clinopyroxene, amphibole and garnet from laser ablation microprobe analysis of garnet pyroxenites from Kakanui, New Zealand. **Neues Jahrbuch fur Mineralogie, Abhirchen**, n. 172 (1), p. 23-41, 1997. http://doi.org/10.1127/njma/172/1997/23

ZHAO, J.; ASIMOW, P.D. Formation and Evolution of a Magmatic System in a Rifting Continental Margin: Neoproterozoic Arc- and MORB-like Dike Swarms in South China. **Journal of Petrology**, n. 59(9), p. 1811–1844, 2018. https://doi.org/10.1093/petrology/egy080

ZHENG, X.; PLANCHEREL, Y.; SAITO, M. A.; SCOTT, P. M.; HENDERSON, G. M. Rare earth elements (REEs) in the tropical South Atlantic and quantitative deconvolution of their non-conservative behavior. **Geochimica et Cosmochimica Acta**, n. 177, p. 217–237, 2016. https://doi.org/10.1016/j.gca.2016.01.018

SUPPLEMENTARY MATERIAL

CHAPTER 2

All additional tables, figures and models:
https://doi.org/10.1016/j.gca.2021.08.017
(direct download link: https://figshare.com/s/534263f4284b5774d2bb)

CHAPTER 3

Full dataset: https://figshare.com/s/da57bb5acaeb59566c55
Additional figures and models: https://figshare.com/s/5848c2191b96a131527c

CHAPTER 4

Rhyolite-MELTS 1.2.0 model results: https://figshare.com/s/04e1a30fc712bbd2da6c